Université de Montréal

Relevé de planètes géantes autour d'étoiles proches par imagerie directe et optimisation d'une technique d'imagerie multibande

par
David Lafrenière

Département de physique
Faculté des arts et des sciences

Thèse présentée à la Faculté des études supérieures
en vue de l'obtention du grade de Philosophiæ Doctor (Ph.D.)
en physique

Avril, 2007

Université de Montréal
Faculté des études supérieures

Cette thèse intitulée:

Relevé de planètes géantes autour d'étoiles proches par imagerie directe et optimisation d'une technique d'imagerie multibande

présentée par:

David Lafrenière

a été évaluée par un jury composé des personnes suivantes:

Paul Charbonneau,	président-rapporteur
René Doyon,	directeur de recherche
Daniel Nadeau,	codirecteur
Serge Demers,	membre du jury
Jean-Luc Beuzit,	examinateur externe
Victor Ostromoukhov,	représentant du doyen de la FES

Thèse acceptée le: 14 août 2007

RÉSUMÉ

Le but principal de cette thèse est la recherche d'exoplanètes par imagerie directe. Étant donné la petite séparation angulaire et le très grand rapport de luminosité entre une planète et son étoile, cette tâche est très difficile. L'approche retenue pour le présent travail est l'imagerie différentielle, qui consiste à obtenir une image référence de la fonction d'étalement de point (FÉP) de l'étoile, et à soustraire cette image référence d'une image cible pour éliminer le signal de l'étoile.

Dans un premier temps, deux outils pour améliorer la qualité de cette soustraction sont développés. Le premier est un nouveau concept instrumental permettant d'améliorer la corrélation des images obtenues à différentes longueurs d'onde en imagerie différentielle spectrale simultanée. Ce concept consiste à placer un diffuseur holographique au plan focal d'entrée d'une caméra multi-canal de façon à briser la cohérence du front d'onde incident, ce qui limite grandement l'effet des aberrations optiques de la caméra sur la structure de la FÉP enregistrée dans chaque canal. Un prototype basé sur ce concept a permis de réaliser une atténuation de la FÉP par un facteur 12–15, soit une amélioration d'un facteur $\sim$5 par rapport à l'atténuation obtenue sans diffuseur. Le deuxième outil développé est un nouvel algorithme permettant de combiner plusieurs images référence de la FÉP de l'étoile en une image référence plus fidèle à l'image cible. L'application de cet algorithme à une séquence d'imagerie différentielle angulaire a permis d'améliorer la sensibilité des observations par un facteur allant jusqu'à 3.

Finalement, les résultats d'une recherche de planètes géantes autour de 85 jeunes étoiles du voisinage solaire sont présentés ; cette recherche a été menée au télescope Gemini Nord. La sensibilité des observations, exprimée en différence de magnitude à 1.6 μm entre une planète et son étoile, est typiquement de 9.5 à 0.5″, 12.9 à 1″, 15 à 2″, et 16.5 à 5″. Pour une étoile cible typique, une étoile de type K0 âgée de 100 millions d'années et située à 22 pc du Soleil, ces sensibilités permettent la détection de planètes plus massives que 2 $M_{\rm Jup}$ avec une séparation projetée entre 40 et 200 UA. En tout, plus

de 300 candidates exoplanètes ont été identifiées autour de 54 des étoiles observées ; un suivi de 48 de ces étoiles a cependant permis de vérifier que leurs candidates sont toutes des étoiles d'arrière-plan. Une analyse statistique des résultats indique que, en supposant une fonction de masse $\mathrm{d}n/\mathrm{d}m \propto m^{-1.1}$ et une distribution en demi-grand axe $\mathrm{d}n/\mathrm{d}a \propto a^{-1}$, la limite supérieure de la fraction d'étoiles avec au moins une planète de masse 0.5–13 M_{Jup} est de 28% pour l'intervalle 10–25 UA, 13% pour 25–50 UA, et 9.3% pour 50–200 UA, à un niveau de crédibilité de 95%.

Mots clés: exoplanètes, imagerie à haute gamme dynamique, traitement d'image, instrumentation astronomique

ABSTRACT

The primary goal of this thesis is the search for exoplanets using direct imaging. Given the small angular separation and the very large luminosity ratio between a planet and its star, this task is very difficult. The approach adopted for the present work is differential imaging, which consists in obtaining a reference image of the point-spread function (PSF) of the star, and subtracting this reference image from a target image to remove the stellar signal.

Initially, two tools aimed at improving the quality of this subtraction are developed. The first is a new instrumental concept that makes it possible to increase the correlation of images obtained at different wavelengths in simultaneous spectral differential imaging. This concept consists in placing a holographic diffuser at the entrance focal plane of a multi-channel camera in order to break the coherence of the wavefront entering the camera; this largely reduces the effect of optical aberrations in the camera on the structure of the PSF recorded in each channel. A prototype based on this concept provided an attenuation of the PSF by a factor 12–15, an improvement by a factor $\sim$5 compared to the attenuation obtained without a diffuser. The second tool developed is a new algorithm allowing to combine several reference images of the stellar PSF together to form a reference image more faithful to the target image. The application of this algorithm to an angular differential imaging sequence of observations yielded an improvement in sensitivity by a factor of up to 3.

Finally, the results of a search for giant planets around 85 nearby young stars are presented; this search was done with the Gemini North telescope. The sensitivity of the observations, expressed in difference of magnitudes at 1.6 μm between a planet and its star, is typically 9.5 at 0.5″, 12.9 at 1″, 15 at 2″, and 16.5 at 5″. For a typical target star, a 100 million year old K0 star located at 22 pc from the Sun, these sensitivities allow the detection of planets more massive than 2 $M_{\rm Jup}$ with a projected separation between 40 and 200 UA. Overall, more than 300 candidate exoplanets were identified around 54 of

the stars observed; a follow-up of 48 of these stars has confirmed that their candidates are all unrelated background stars. A statistical analysis of the results indicates that, by assuming a mass function $\mathrm{d}n/\mathrm{d}m \propto m^{-1.1}$ and a semi-major axis distribution $\mathrm{d}n/\mathrm{d}a \propto a^{-1}$, the upper limits on the fraction of stars with at least one planet of mass 0.5–13 M_{Jup} are 28% for the interval 10–25 AU, 13% for 25–50 AU, and 9.3% for 50–200 AU, with a 95% credibility.

Keywords: exoplanets, high-contrast imaging, image processing, astronomical instrumentation

TABLE DES MATIÈRES

LISTE DES TABLEAUX

LISTE DES FIGURES

LISTE DES ANNEXES

LISTE DES SIGLES ET ABRÉVIATIONS

ADI	Angular differential imaging
AO	Adaptive optics
AU	Astronomical unit
BD	Brown dwarf
CDS	Centre de données astronomiques de Strasbourg
CI	Confidence interval
CL	Confidence level
CoRoT	COnvection, ROtation, and planetary Transits
FÉP	Fonction d'étalement de point
FOV	Field of view
FWHM	Full-width-at-half-maximum
GDPS	Gemini Deep Planet Survey
GPI	Gemini Planet Imager
HARPS	High Accuracy Radial velocity Planet Searcher
HD	Holographic diffuser
HiCIAO	High-contrast Coronagraphic Imager with Adaptive Optics
HST	Hubble Space Telescope
IDA	Imagerie différentielle angulaire
IDSS	Imagerie différentielle spectrale simultanée
IRDIS	Infra-Red Dual-beam Imager and Spectrograph
JWST	James Webb Space Telescope
LOCI	Locally optimized combination of images
MCC	Multi-channel camera
MOA	Microlensing Observations in Astrophysics

NICI	Near-Infrared Coronagraphic Imager
NSDI	Non-simulataneous spectral differential imaging
OA	Optique adaptative
OGLE	Optical Gravitational Lensing Experiment
P.A.	Position angle
PFI	Planet Formation Imager
PLMH	Pleine largeur à mi-hauteur
PSC	Point source catalogue
PSF	Point-spread function
RV	Radial velocity
SDI	Spectral Differential Imager
S/N	Signal-to-noise ratio
SOFIA	Stratospheric Observatory For Infrared Astronomy
SPHERE	Spectro-Polarimetric High-contrast Exoplanet REsearch instrument
SSDI	Simultaneous spectral differential imaging
TPF	Terrestrial Planet Finder
TRIDENT	TRiple-Imageur DÉcouvreur de Naine T
UA	Unité astronomique
VLT	Very Large Telescope

À tous ceux qui ont contribué à mon émerveillement face à la nature et à l'univers,

et aux gens que j'aime, Louiselle, Benjamin, Annie, Louise, et Geneviève.

REMERCIEMENTS

Premièrement, je tiens à remercier mes directeurs de thèse, René et Daniel, pour m'avoir pris sous leur aile et accompagné pendant ce périple. Merci pour m'avoir si bien conseillé et supporté, j'ai beaucoup appris grâce à vous. Merci pour les opportunités de participation à des conférences, séjours d'observation, et grands projets d'instruments que vous m'avez offertes ; celles-ci m'ont permis d'étendre mes horizons, d'établir des contacts, et de gagner un peu de visibilité. Merci infiniment René pour toute la confiance que tu m'as témoignée, ça m'a profondément touché, et merci Daniel pour m'avoir enseigné la rigueur dans tous les aspects de mon nouveau travail.

Je veux ensuite remercier mes amis du département, en particulier Mathilde, Étienne, Laurent, Christian, Loïc, André-Nicolas, Olivier, Olivier, Marie-Maude, Patrick, et Jean-François, pour un peu plus de quatre belles années dont je me souviendrai longtemps. Un merci spécial à Mathilde et à Étienne, avec qui j'ai partagé un bureau et beaucoup de plaisir ; grâce à vous, j'avais doublement envie de rentrer à l'université chaque matin. Je tiens également à souligner vos nombreuses contributions à mon travail. Merci à Christian, mon prédécesseur, pour l'aide qu'il m'a apportée à mes débuts. Merci aux professeurs, en particulier à Nicole, Tony, Serge, et Pierre, et à la bientôt-professeure Suzanne ; j'ai bien aimé discuter avec vous à l'heure du lunch et au café. Enfin, merci à René R. pour ses encouragements et conseils judicieux tout au long de mon doctorat.

Un gros merci à Philippe Vallée pour toute l'aide qu'il m'a apportée en laboratoire, et merci aux gars de l'atelier, Guillaume et Jean-Sébastien, pour avoir fabriqué toutes les pièces dont j'avais besoin. Merci à Luc pour toute son aide en informatique.

Merci à mes parents, Louiselle et Benjamin, et à mes grandes soeurs, Annie et Louise, pour le support et les encouragements qu'ils m'ont offerts tout au long de mes études et depuis mon plus jeune âge.

Tous ceux qui sont passés par là le savent : on ne peut pas laisser sa thèse au bureau, elle nous suit constamment. Alors un énorme merci à ma belle Geneviève, que j'aime

tellement, pour sa compréhension, son soutien, son aide, et son amour. Merci aussi pour avoir assisté sans broncher aux mille et une premières versions de mes présentations, révisé mes premiers brouillons, résolu mes intégrales, et pour tous les autres petits gestes que tu as posés pour m'aider. Merci encore, je n'aurais pas pu faire ça sans toi.

Finalement, je voudrais remercier les organismes qui m'ont soutenu financièrement pendant mes études de doctorat : la Faculté des études supérieures de l'Université de Montréal, le Conseil de recherches en sciences naturelles et en génie du Canada, et le Fonds québécois de recherche sur la nature et les technologies.

S'il y en a que j'oublie, pardonnez-moi, je vous remercie tout de même.

–David

Il y a d'innombrables soleils

et d'innombrables terres,

toutes tournant autour de leur soleil

comme le font les sept planètes de notre système.

Nous n'en voyons que les soleils

parce qu'ils sont les plus grands et les plus lumineux,

mais leurs planètes nous restent invisibles

parce qu'elles sont petites et peu lumineuses.

Les innombrables mondes de l'univers ne sont pas pires

et moins habités que notre Terre.

De L'Infinito Universo e Mundi (1584)

Giordano Bruno, 1548–1600

CHAPITRE 1

INTRODUCTION

De façon générale, le terme *planète* désigne un corps céleste orbitant une étoile ou un rémanent d'étoile et ayant une masse qui est d'une part suffisante pour que sa propre gravité lui confère une forme plutôt sphérique, et d'autre part insuffisante pour lui permettre de soutenir la fusion du deutérium en son coeur.[1] Dans le cas d'une planète orbitant le Soleil, il est de plus requis que l'influence gravitationnelle de la planète soit suffisante pour dégager l'espace entourant son orbite de tous débris ou astéroïdes. Dans le cas d'une planète orbitant une autre étoile, le terme *exoplanète*, ou encore *planète extra-solaire*, est utilisé.

Les objets ayant une masse suffisante pour enclencher la fusion du deutérium mais insuffisante pour enclencher celle de l'hydrogène sont appelés *naines brunes*. Celles-ci peuvent être isolées dans l'espace, être en orbite autour d'une étoile, ou encore faire partie d'un système de deux ou plusieurs naines brunes liées gravitationnellement. Enfin, les *étoiles* sont des objets dont la masse, plus grande que celles des naines brunes, permet la fusion de l'hydrogène en leur coeur. Les limites, en masse, entre planète et naine brune et entre naine brune et étoile sont établies à 13 M_{Jup} et $\sim$75 M_{Jup}, respectivement, où M_{Jup} désigne la masse de Jupiter. De l'autre côté de l'échelle de masse, les objets ayant une masse inférieure à celles des planètes sont appelés *planètes naines*, ou encore *astéroides*. Finalement, un objet de masse planétaire qui est isolé dans l'espace, plutôt qu'en orbite autour d'une étoile, est appelé *planémo*, ou plus rarement, *sous-naine brune*.

Les planètes peuvent être divisées en deux classes générales : les planètes telluriques et les planètes géantes gazeuses. Les planètes telluriques sont similaires à la Terre, elles sont constituées principalement de roches et ont une croûte solide. Les planètes géantes

[1] International Astronomical Union, resolution 5A (http ://www.iau.org/iau0603.414.0.html); Working Group on Extrasolar Planets of the International Astronomical Union (http ://www.dtm.ciw.edu/boss/definition.html)

gazeuses sont similaires à Jupiter et, comme leur nom l'indique, elles sont composées principalement de gaz et sont beaucoup plus massives que les planètes telluriques ; elles n'ont pas de croûte ni même de surface bien définie. Dans cette thèse, il ne sera question que des planètes géantes gazeuses.

L'étude des exoplanètes géantes gazeuses est importante à plusieurs égards. D'abord, pour comprendre comment les planètes se forment et comment elles évoluent, mais aussi parce que les planètes géantes ont une incidence directe sur le sort des planètes de plus faible masse. Dans un système planétaire comportant des planètes géantes, ce sont ces dernières qui, par leur grande influence gravitationnelle, établissent les zones de stabilité dans lesquelles des planètes telluriques peuvent exister. Particulièrement, en régissant la stabilité de la zone dite *habitable*, à l'intérieur de laquelle une planète tellurique pourrait avoir de l'eau sous forme liquide à sa surface, les planètes géantes pourraient jouer un rôle clé dans le développement de la vie. Ultimement, les études portant sur les exoplanètes permettront de mieux comprendre l'origine de la Terre et du système solaire, de clarifier les perspectives de développement de la vie dans d'autres systèmes, et de mieux cerner notre position dans l'univers.

1.1 Les planètes géantes

Les deux prochaines sous-sections sont basées sur les revues de Burrows et al. (2001) et Hubbard et al. (2002), et sur les modèles de Burrows et al. (1997); Chabrier et al. (2000); Allard et al. (2001) ; et Baraffe et al. (2003).

1.1.1 Structure et évolution

Les planètes géantes gazeuses ont un coeur composé d'hydrogène et d'hélium métallique au-dessus duquel se trouve une atmosphère composée principalement de molécules ; elles peuvent aussi posséder un petit coeur solide ($\sim$10 $M_{\oplus}$) en leur centre. Le transport d'énergie à l'intérieur des planètes géantes se fait par convection et le taux de

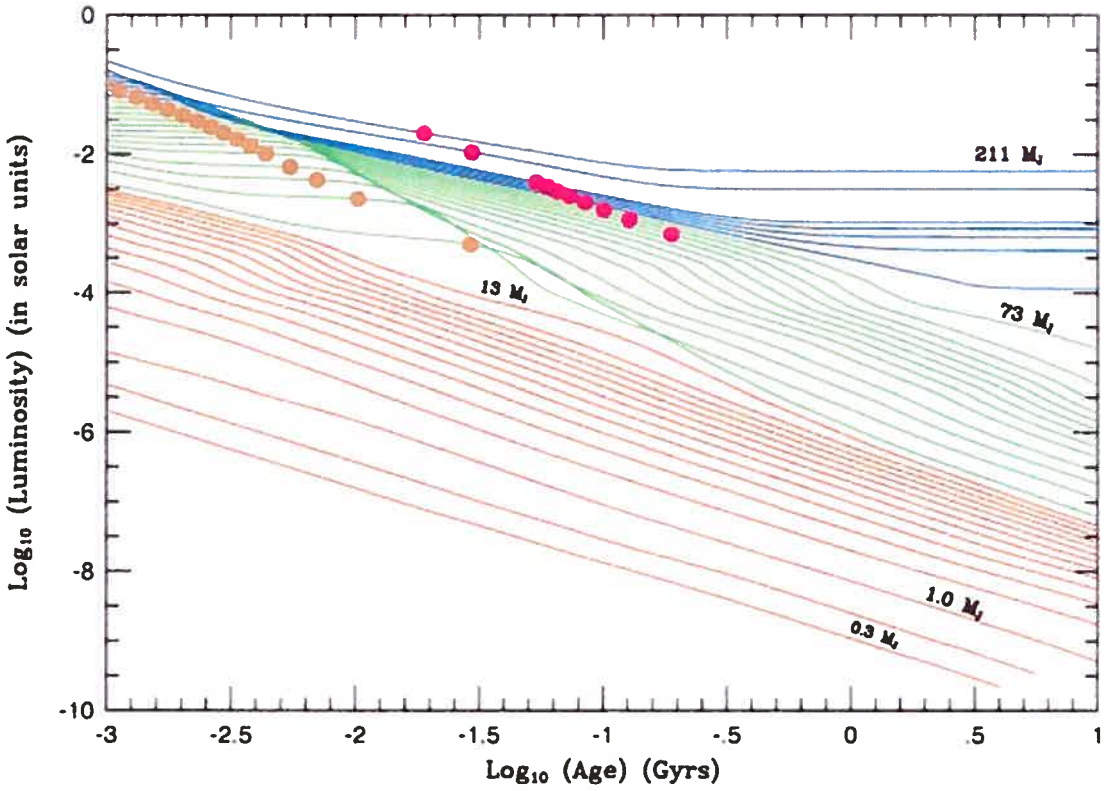

Figure 1.1 Courbes d'évolution de la luminosité des planètes géantes (*rouge*), des naines brunes (*vert*) et des étoiles de faible masse (*bleu*). Pour une masse donnée, le point beige indique le moment où 50% du deutérium a été fusionné et le point magenta indique le moment où 50% du lithium a été fusionné. De Burrows et al. (2001).

perte d'énergie à leur surface est contrôlé par les opacités radiatives de leur atmosphère. Les planètes géantes étant trop peu massives pour soutenir des réactions de fusion nucléaire en leur centre, elles ne disposent pas de source interne d'énergie suffisante pour compenser l'énergie perdue à leur surface. Elles sont donc condamnées à refroidir pendant toute leur vie.

Les Figures 1.1–1.3 montrent les courbes d'évolution (selon les modèles de Burrows et al. (2001)) de la luminosité, de la température efficace, et du rayon des planètes géantes, des naines brunes et des étoiles de faible masse. La luminosité des planètes géantes diminue typiquement d'un facteur $\sim$10 par décade d'âge. Les luminosités à 1 milliard d'années varient de $10^{-6}\ L_{\odot}$ à $10^{-9}\ L_{\odot}$ selon la masse. Au début de leur vie

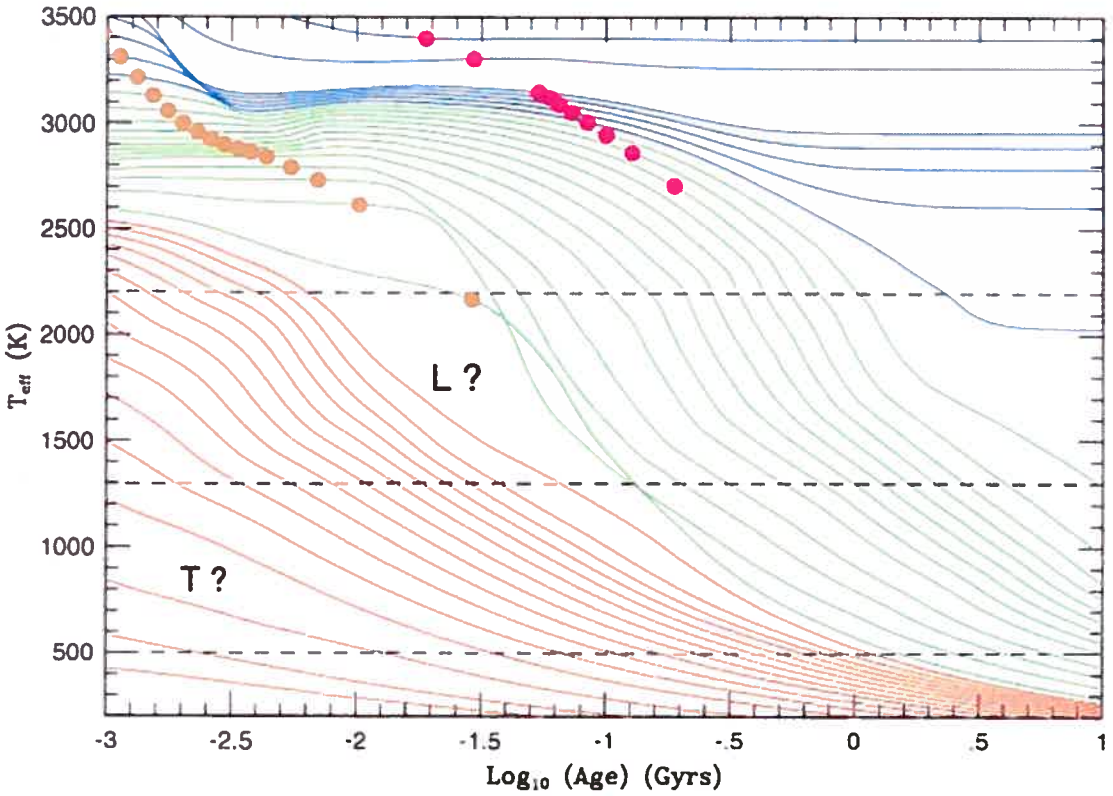

Figure 1.2 Courbes d'évolution de la température efficace des planètes géantes (*rouge*), des naines brunes (*vert*) et des étoiles de faible masse (*bleu*). Pour une masse donnée, le point beige indique le moment où 50% du deutérium a été fusionné et le point magenta indique le moment où 50% du lithium a été fusionné. De Burrows et al. (2001).

(<10 millions d'années), les planètes géantes ont une température allant de ~500 K à 2500 K selon leur masse, les plus massives étant les plus chaudes. Les planètes moins massives que 1, 5, et 13 $M_{\rm Jup}$ atteignent une température de 500 K après 10 millions, 100 millions, et 1 milliard d'années, respectivement. À des âges d'un milliard d'années et plus, les rayons des étoiles très tardives, des naines brunes, et des planètes géantes sont tous similaires à celui de Jupiter ; ils ne varient que de ~30% sur près de deux ordres de grandeur en masse. Ceci résulte d'une compétition entre des effets de Coulomb et des effets de dégénérescence des électrons. Le premier tente d'établir une densité fixe et mène à la dépendance $R \propto M^{1/3}$. Le deuxième mène à la dépendance connue d'un objet supporté par la pression d'électrons dégénérés $R \propto M^{-1/3}$. Ces deux effets conspirent

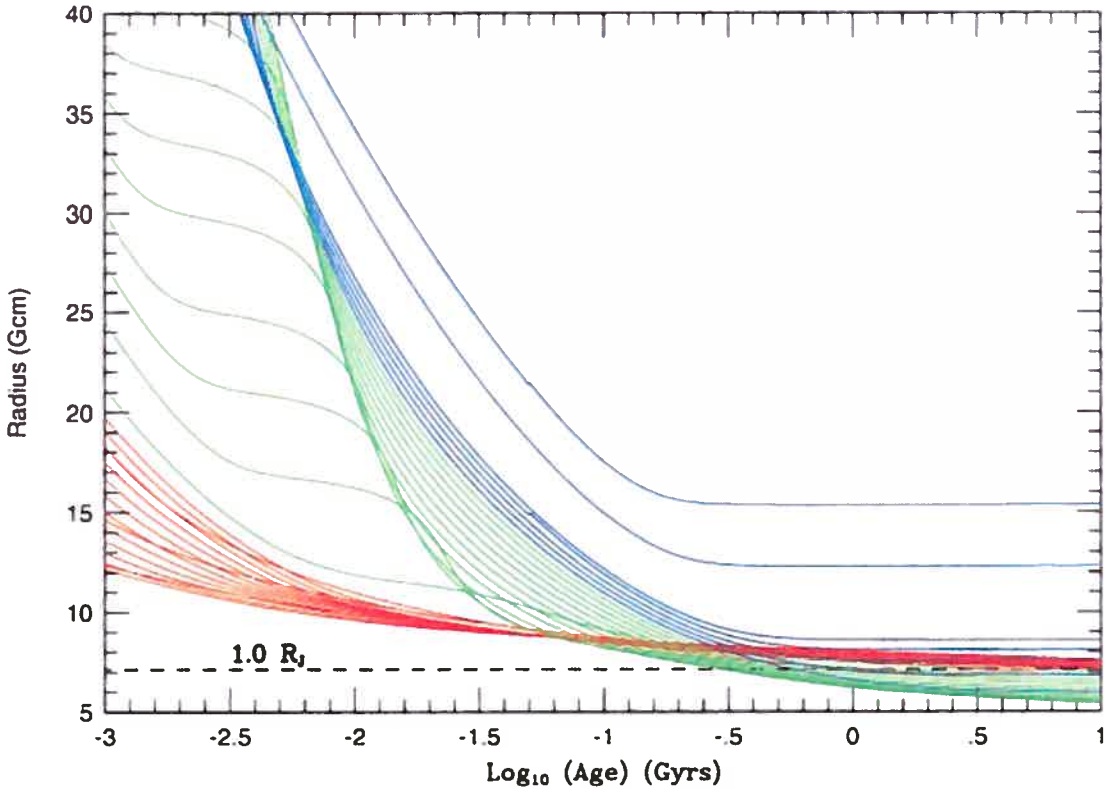

Figure 1.3 Courbes d'évolution du rayon des planètes géantes (*rouge*), des naines brunes (*vert*) et des étoiles de faible masse (*bleu*). De Burrows et al. (2001).

donc pour rendre le rayon approximativement constant.

1.1.2 Atmosphère et distribution spectrale d'énergie

Les éléments dominants dans l'atmosphère des planètes géantes sont l'hydrogène, l'hélium, le carbone, l'azote et l'oxygène. L'hydrogène se trouve principalement sous la forme de H_2. À des températures inférieures à $\sim$1500 K, le carbone se trouve principalement sous forme de CH_4, et sous forme de CO à des températures plus élevées. L'azote se retrouve sous forme de N_2 à des températures supérieures à 700 K et sous forme de NH_3 à plus basse température. Enfin, l'oxygène est principalement contenu dans le H_2O.

Les molécules et éléments condensés s'enfoncent dans l'atmosphère sous l'action de la gravité et s'accumulent à la plus haute température à laquelle ils peuvent sur-

vivre à l'état condensé. Les substances dont les énergies de liaison sont les plus faibles (H_2O, NH_3) forment des nuages aux plus basses températures, donc plus haut dans l'atmosphère pour une planète donnée. Les nuages de NH_3 et de H_2O se forment à des températures de moins de $\sim$200 K et $\sim$500 K, respectivement. Les substances liées plus fortement (silicates, fer) forment des nuages à des températures plus élevées, donc plus bas dans l'atmosphère. À des températures de moins de $\sim$2300 K, le fer est sous forme de gouttelettes qui forment un nuage à une profondeur où la température est environ 2000 K. Les silicates se condensent et précipitent à des températures de moins de 1600–1800 K. Comme la température efficace des planètes géantes est généralement inférieure à 1500 K, il y a très peu de fer ou de poussière dans leur atmosphère. La condensation/précipitation des métaux lourds et des silicates à des températures supérieures à $\sim$1600 K permet aux métaux alcalins (notamment Na et K) de survivre sous forme neutre dans l'atmosphère jusqu'à des températures de $\sim$1000 K. Ils seraient autrement presque totalement emprisonnés dans divers composés.

L'atmosphère des objets dont la température efficace est inférieure à 150 K est caractérisée par la présence de CH_4 gazeux et de nuages de NH_3. À des températures efficaces de 150–500 K, l'atmosphère contient du NH_3 et du CH_4 sous forme gazeuse et des nuages de H_2O à haute altitude. Les objets ayant une température efficace entre 500 K et 900 K possèdent une atmosphère libre de tout nuage ; celle-ci est dominée par du H_2O, CH_4, et H_2 sous forme gazeuse et des métaux alcalins neutres. L'atmosphère des objets de température efficace de 900–1500 K contient de bonnes quantités de K et Na neutre au-dessus d'une couche nuageuse de silicates. Les objets les plus chauds ($T_{\rm eff} \gtrsim 1500$ K) ont une couche de silicates très haut dans leur atmosphère, ce qui leur confère le plus grand albédo des planètes géantes.

Généralement les molécules les plus abondantes dans l'atmosphère dominent l'opacité. Le spectre des planètes ayant une température efficace supérieure à 1500 K est donc dominé par l'opacité du H_2O, du CO, et des grains de silicates. Pour les objets dont la température efficace est inférieure à 1500 K, les principales sources d'opacité sont le

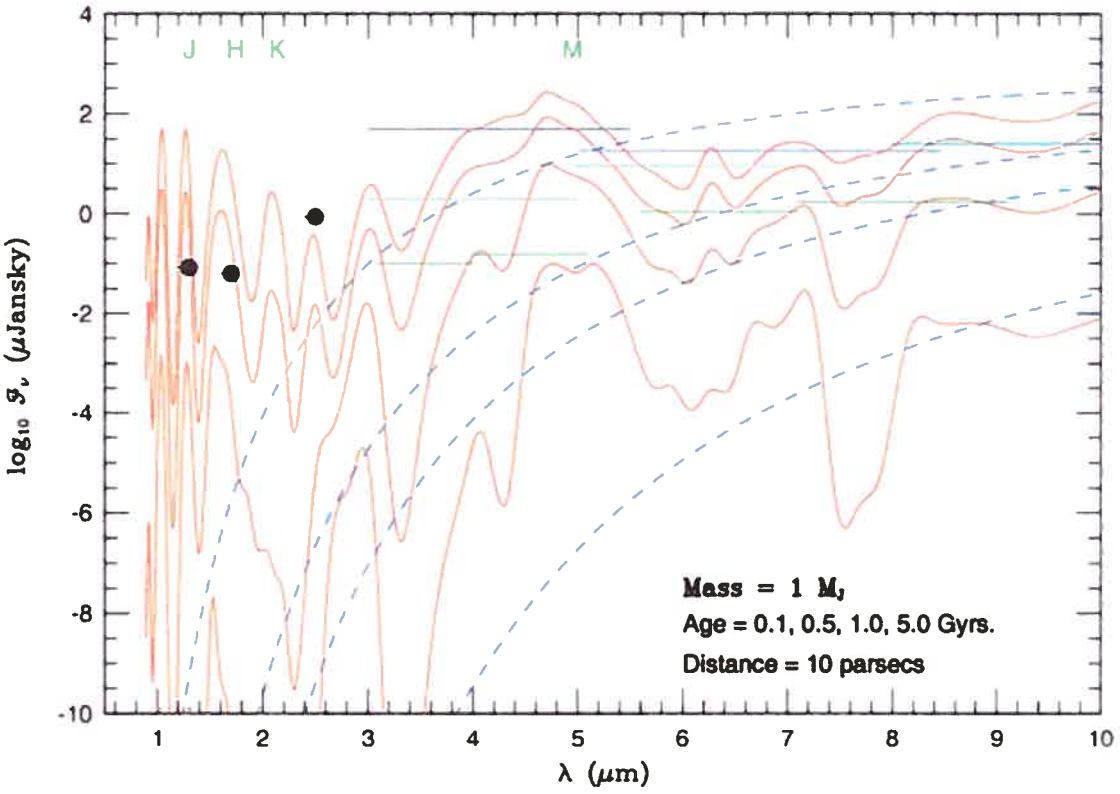

Figure 1.4 Spectres théoriques d'une planète de 1 M_{Jup} à différents âges. Ces spectres sont comparés aux courbes de corps noirs à la température efficace de la planète (tirets bleus). Les points noirs indiquent les sensibilités approximatives du télescope spatial Hubble). Les traits horizontaux indiquent les sensibilités approximatives du télescope spatial Spitzer (vert foncé), du télescope SOFIA (bleu), et du télescope Gemini (vert pâle). De Burrows et al. (2001).

H_2O, le CH_4, le NH_3, le H_2, et les métaux alcalins. L'absorption par le H_2O, le CH_4, et le H_2 supprime partiellement l'émission au-delà de 10 μm. Cette suppression du flux, combinée aux fenêtres d'absorption du H_2O (qui définissent les bandes de l'infrarouge proche) forcent le flux vers le bleu. Le flux des planètes dans les bandes spectrales Z (1.05 μm), J (1.25 μm), H (1.65 μm) et K (2.2 μm) est donc plus grand que le flux d'un corps noir à la température efficace de la planète. La forte absorption par le H_2 et le CH_4 en K rend l'émission dans cette bande plus faible que l'émission dans les bandes J et H. La Figure 1.4 montre les spectres théoriques d'une planète de 1 M_{Jup} à différents âges.

1.1.3 Formation

Il existe présentement deux principaux mécanismes de formation de planètes géantes. Le premier est la formation par agglomération et accrétion, selon laquelle des collisions de planétésimaux dans le disque proto-planétaire forment graduellement des noyaux de matière solide qui, lorsqu'ils atteignent une certaine masse critique, peuvent accréter le gaz présent dans le disque (Pollack et al., 1996). Ce scénario correspond à la vision traditionnelle de la formation des planètes géantes du système solaire. Les travaux de Pollack et al. (1996) indiquent qu'une planète similaire à Jupiter peut se former par ce mécanisme en $\sim$5 millions d'années. Des études plus récentes (Alibert et al., 2005) ont montré que le demi-grand axe de l'orbite d'une proto-planète peut changer au cours de sa formation suite à l'interaction de la proto-planète avec le disque dans lequel elle se trouve. Ceci permet à la proto-planète de balayer un plus grand volume de planétésimaux et d'atteindre plus rapidement la masse critique nécessaire pour déclencher une accrétion massive de gaz. Ces travaux indiquent qu'une planète comme Jupiter pourrait se former en $\sim$1 million d'années. Ces temps de formation sont comparables ou légèrement inférieurs au temps de vie des disques proto-planétaires, qui est estimé à $\sim$6 millions d'années (Haisch et al., 2001). Le temps de formation des planètes géantes par agglomération et accrétion est cependant fortement dépendant de la quantité de matériel solide présent dans le disque, et la formation de planètes de la masse de Jupiter est peu probable à des séparations supérieures à $\sim$20 UA (Chambers, 2006; Inaba et al., 2003; Pollack et al., 1996), où la quantité de planétésimaux est généralement trop faible.

Le deuxième mécanisme de formation est celui de l'instabilité gravitationnelle, selon laquelle des perturbations gravitationnelles dans un disque proto-planétaire conduisent rapidement à la formation de noeuds de surdensité qui s'effondrent ensuite sur eux-mêmes, produisant des planètes géantes (Boss, 1997, 2001). Ce procédé peut former des planètes géantes dans un temps très court ($\sim 10^3$ ans) à des séparations orbitales pouvant aller jusqu'à 20–30 UA.

Il existe quelques autres mécanismes capables de former des planètes géantes. Par exemple, la collision entre deux étoiles ayant chacune un disque circumstellaire produit un choc qui peut déclencher l'effondrement gravitationnel de certaines régions des disques (Shen & Wadsley, 2006). Les résultats de simulations numériques indiquent que des planètes géantes peuvent être formées à des séparations de plusieurs dizaines d'UA ou plus par ce procédé (Shen & Wadsley, 2006). Le modèle d'accrétion compétitive et éjection est un autre exemple de mécanisme (Reipurth & Clarke, 2001). Ce modèle, initialement développé pour expliquer la formation des naines brunes, propose que ces dernières sont des embryons stellaires éjectés dynamiquement hors de leur zone d'approvisionnement au tout début de leur formation ; ces embryons n'auraient donc pas eu le temps d'accréter suffisamment de masse pour devenir des étoiles. Les simulations numériques de Bate & Bonnell (2005) ont montré que ce processus pouvait tout aussi bien mener à la formation de planètes géantes en orbite à des dizaines d'UA autour de leur étoile.

Pendant et après leur formation, les planètes sont soumises à différentes forces qui peuvent modifier leur orbite. Cette migration orbitale peut être causée par l'interaction gravitationnelle de la planète avec un disque de gaz (Tanaka et al., 2002; Lin et al., 1996; Goldreich & Tremaine, 1980), avec un disque de planétésimaux (Levison et al., 2007; Murray et al., 1998), ou avec d'autres planètes du même système (Chatterjee et al., 2007; Veras & Armitage, 2004; Rasio & Ford, 1996; Weidenschilling & Marzari, 1996). Ces interactions peuvent amener une planète à s'approcher ou s'éloigner de son étoile sur une distance pouvant aller jusqu'à quelques dizaines d'UA. Les paramètres orbitaux des systèmes planétaires ne sont donc pas entièrement déterminés par les mécanismes de formation.

1.2 La recherche d'exoplanètes

La recherche d'exoplanètes est aujourd'hui l'un des domaines les plus actifs de l'astronomie. Cinq techniques de recherche sont généralement utilisées : la vélocimétrie, l'astrométrie, la photométrie, la micro-amplification gravitationnelle, et l'imagerie directe. Pour des raisons techniques, la plupart de ces méthodes de recherche sont présentement limitées à la détection de planètes géantes.

1.2.1 Vélocimétrie

Lorsqu'une planète orbite autour d'une étoile, l'étoile et la planète se déplacent toutes deux autour de leur centre de masse commun sur des orbites elliptiques de même période. Comme la masse de l'étoile est beaucoup plus grande que celle de la planète, l'amplitude de son déplacement est beaucoup plus petite. Ce faible déplacement de l'étoile peut être détecté par l'observation de sa vitesse radiale, selon la technique de vélocimétrie. La vitesse radiale de l'étoile est obtenue par spectroscopie haute résolution en mesurant le décalage de ses raies spectrales par effet Doppler. La première exoplanète en orbite autour d'une étoile normale a été découverte par cette technique il y a un peu plus de 10 ans (Mayor & Queloz, 1995).[2] Il s'agit d'une planète géante qui orbite son étoile, 51 Peg, en seulement quatre jours ; la courbe de vitesse radiale de cette étoile est montrée à la Figure 1.5.

L'observation de la courbe d'oscillation de la vitesse radiale d'une étoile fournit directement la période de l'orbite ainsi que l'amplitude de la variation de sa vitesse le long de la ligne de visée. L'excentricité de l'orbite peut de plus être déterminée à partir de la forme de la courbe. La période orbitale et la masse de l'étoile[3], combinées à la troisième

[2]Il est à noter qu'un compagnon avec $m \sin i$=11 $M_{\rm Jup}$ a été découvert autour de l'étoile HD 114762 par Latham et al. (1989), mais l'inclinaison de son orbite est vraisemblablement assez faible (Hale, 1995; Mazeh et al., 1996), de sorte que sa masse réelle est fort probablement bien au-delà de la masse limite des planètes. De plus, l'existence d'un compagnon avec $m \sin i$=11.6 $M_{\rm Jup}$ autour de l'étoile γ Cephei (Hatzes et al., 2003) avait initialement été postulée par Campbell et al. (1988) et Walker et al. (1992), sans toutefois être confirmée.

[3]La masse de l'étoile est rarement mesurée de façon directe, elle est généralement déterminée à partir

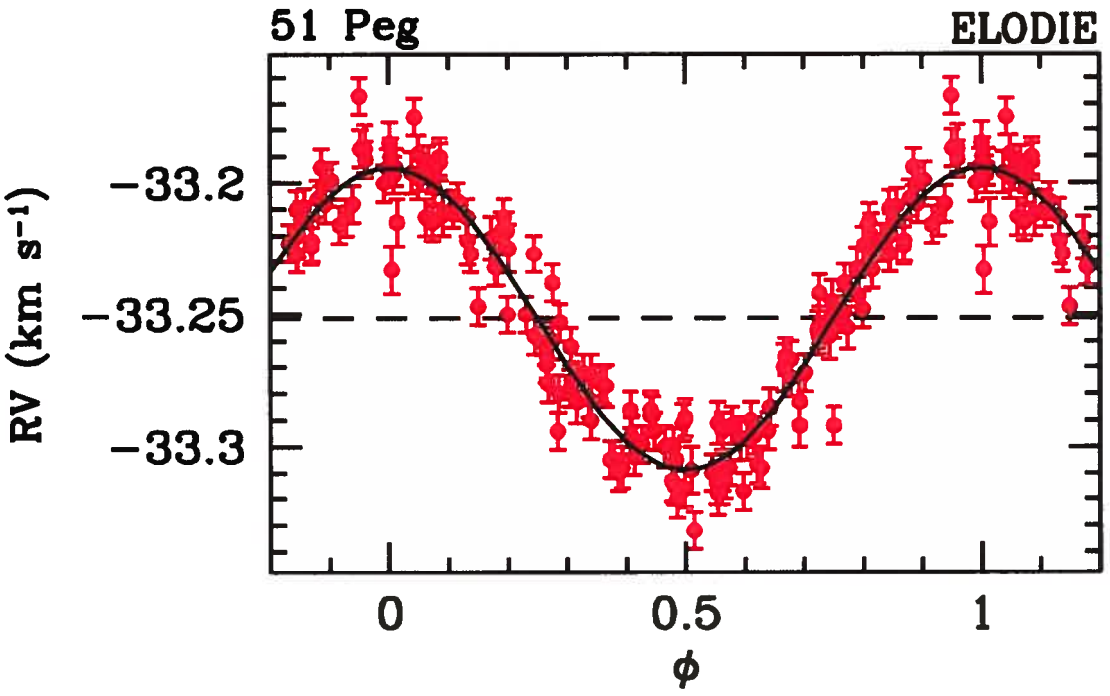

Figure 1.5 Courbe de la vitesse radiale de l'étoile 51 Peg. La variation de période 4.23 jours est due à la présence d'une planète de masse minimum 0.468 $M_{\rm Jup}$ ($m_{\rm pl} \sin i$) sur une orbite de 0.052 UA. De Mayor & Queloz (1995).

loi de Kepler, fournissent le demi-grand axe $a_{\rm pl}$ de l'orbite de la planète. Par la suite, la demi-amplitude de la variation de vitesse radiale permet de déterminer la valeur de $m_{\rm pl} \sin i$, où $m_{\rm pl}$ est la masse de la planète et i est l'inclinaison orbitale par rapport à la ligne de visée ($i = 0°$ indique une orbite dans le plan du ciel) ; ceci constitue une limite inférieure à la masse de la planète. La recherche par vélocimétrie a mené à la découverte de plus de 200 exoplanètes jusqu'à ce jour ; c'est de loin la technique ayant connu le plus de succès.

Les facteurs limitant la détection de planètes par vélocimétrie sont la précision des mesures de vitesse radiale, la résolution temporelle des observations et la période de temps écoulée depuis le début des observations. L'amplitude de la vitesse radiale d'une étoile est proportionnelle à la masse de la planète qui l'orbite et décroît comme la racine

d'observations spectroscopiques à haute résolution et de modèles d'atmosphère et d'évolution stellaires.

carrée du demi-grand axe de celle-ci. Les planètes plus éloignées de leur étoile sont donc plus difficiles à détecter, d'autant plus que leur période peut être très longue. Des variations de vitesse radiale aussi petites que 1 m/s peuvent maintenant être détectées par des instruments spécialisés (e.g. HARPS, Rupprecht et al., 2004). Pour référence, la demi-amplitude de la vitesse radiale d'une étoile ayant une planète de 1 M_{Jup} sur une orbite de demi-grand axe 1 AU orientée perpendiculairement au plan du ciel serait de $\sim$30 m/s.

1.2.2 Astrométrie

Comme pour la technique de détection par vélocimétrie, la recherche par astrométrie repose sur la détection du mouvement de l'étoile qui est induit par l'influence gravitationnelle de la planète. Cependant, la détection par astrométrie vise à déterminer le déplacement angulaire de l'étoile dans le plan du ciel plutôt que la variation de sa vitesse le long de la ligne de visée.

Le déplacement angulaire de l'étoile est proportionnel à $\frac{m_{\mathrm{pl}} a_{\mathrm{pl}}}{m_\star d_\star}$, où m_{pl} et a_{pl} sont respectivement la masse et le demi-grand axe de la planète, $m_\star$ est la masse de l'étoile, et $d_\star$ est la distance de l'étoile au Soleil. La recherche par astrométrie est donc plus efficace pour les étoiles les plus rapprochées du Soleil et pour les planètes les plus éloignées de leur étoile ; par contre, de telles planètes peuvent avoir de très longues périodes, prévenant leur détection. Pour référence, une planète comme Jupiter orbitant une étoile située à 10 pc du Soleil et ayant une orbite de demi-grand axe égal à 1 AU orientée dans le plan du ciel causerait un déplacement angulaire maximal de l'étoile d'environ $0.0001''$.

Étant donné les très petits déplacements angulaires en jeu, les recherches de planètes par astrométrie n'ont conduit à aucune découverte de planète jusqu'à ce jour. Cependant, le déplacement d'une étoile causé par une planète connue au préalable a été mesuré avec succès, permettant une détermination précise de la masse de la planète (Benedict et al., 2002). Dans 5 à 10 ans, les mission spatiales Gaia (Mignard, 2005) et SIM-PlanetQuest (Marr, 2006) permettront des mesures astrométriques suffisamment précises pour décou-

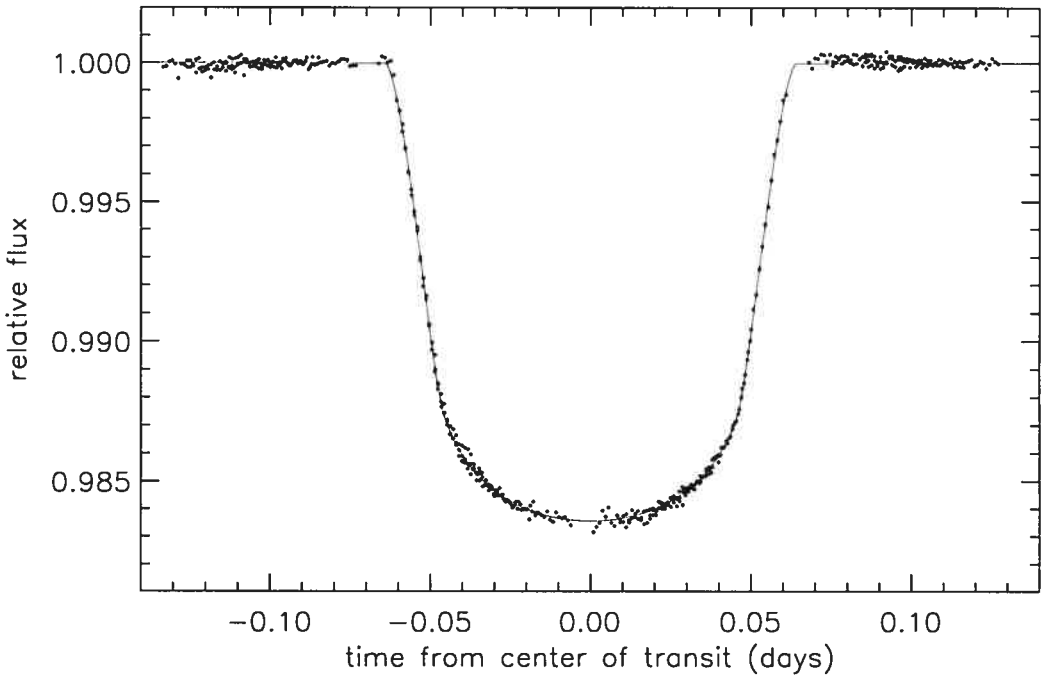

Figure 1.6 Courbe de lumière de l'étoile HD 209458 obtenue avec le *HST*. La diminution de brillance observée est due à l'occultation du disque de l'étoile par une planète de rayon 1.32 R_{Jup}, masse 0.69 M_{Jup}, et demi-grand axe 0.045 UA. De Brown et al. (2001).

vrir plusieurs exoplanètes par astrométrie.

1.2.3 Photométrie

L'occultation partielle d'une étoile par sa planète entraîne une variation de la brillance observée de l'étoile en fonction du temps alors que la planète cache différentes fractions et différentes parties du disque stellaire. La présence d'une planète peut donc être révélée par un suivi photométrique à haute précision de son étoile. Les premières observations de ce phénomène ont été réalisées par Charbonneau et al. (2000) et Henry et al. (2000) pour la planète orbitant l'étoile HD 209458 ; la courbe de lumière de cette étoile est montrée à la Figure 1.6.

La probabilité qu'une planète soit orientée telle qu'elle occulte son étoile lorsqu'ob-

servée de la Terre est plutôt faible, de l'ordre de 0.5% pour une planète sur une orbite de demi-grand axe égal à 1 UA (Charbonneau et al., 2007) ; cette probabilité est directement proportionnelle au rayon de l'étoile et inversement proportionnelle au demi-grand axe de l'orbite de la planète. Étant donné cette faible probabilité, l'efficacité de la technique d'occultation photométrique vient du fait qu'il est possible de sonder rapidement un très grand nombre d'étoiles. La précision photométrique des observations actuelles est typiquement de quelques millièmes de magnitude, permettant de détecter des planètes de rayon supérieur à $\sim$0.5 fois celui de Jupiter autour d'étoiles de type solaire.

L'analyse de la courbe de lumière d'une occultation permet non seulement la détermination précise de l'inclinaison de l'orbite de la planète par rapport à la ligne de visée, mais aussi celle du rayon de la planète, moyennant une supposition sur le rayon de l'étoile. Effectivement, la fraction de la lumière de l'étoile qui est bloquée par la planète est égale au rapport du carré de leur rayon. Une occultation photométrique ne peut à elle seule révéler la nature exacte d'un compagnon puisque les étoiles les plus tardives, les naines brunes, et les planètes géantes gazeuses ont toutes des rayons similaires (§1.1.1). Les détections par occultation photométrique doivent être vérifiées par mesure de vitesse radiale. Une fois combinée avec de telles mesures, la valeur de l'inclinaison orbitale permet une détermination précise de la masse du compagnon. La gravité de surface et la densité moyenne d'une planète peuvent par la suite être déterminées.

Un système planétaire dans lequel la planète passe devant le disque de son étoile offre des possibilités d'observations très intéressantes. La comparaison de spectres de l'étoile obtenus avant et pendant une occultation peut révéler certains constituants de l'atmosphère de la planète puisque, pendant l'occultation, une partie de la lumière de l'étoile passe à travers la haute atmosphère de la planète. Ainsi il a été possible de détecter du sodium dans l'atmosphère de l'exoplanète HD 209458b (Charbonneau et al., 2002). L'observation de l'éclipse secondaire, lorsque la planète passe derrière l'étoile, permet de mesurer le rapport du flux total (émis et réfléchi) de la planète à celui de l'étoile. En effet, le flux observé avant ou après l'éclipse secondaire correspond à la somme du flux

de la planète et de l'étoile alors que celui observé pendant l'éclipse correspond au flux de l'étoile uniquement. Lorsque ce rapport de flux est mesuré dans l'infrarouge thermique, ou le flux réfléchi par la planète peut être négligé, il est possible de déterminer la température de la planète puisqu'à ces longueurs d'ondes, le rapport de flux est proportionnel au rapport des températures de la planète et de l'étoile. Des observations faites avec le télescope spatial *Spitzer* à des longueurs d'onde de 4.5–24 μm ont permis de déterminer la température de deux exoplanètes par cette méthode (HD 209458b, $T \sim 1060$ K, Charbonneau et al., 2005 ; TReS-1, $T \sim 1130$ K, Deming et al., 2005). Une technique similaire peut aussi être utilisée pour mesurer le spectre d'une planète ; ceci a été accompli pour deux exoplanètes (HD 209458b, Richardson et al., 2007 ; HD 189733b, Grillmair et al., 2007).

Plusieurs programmes d'observation d'occultations photométriques sont actuellement en cours (voir Charbonneau et al. 2007 et les références qui s'y trouvent) ; ceux-ci ont déjà mené à plusieurs découvertes d'exoplanètes (e.g. Konacki et al., 2003; Alonso et al., 2004; Cameron et al., 2007) et plusieurs autres sont à prévoir pour les prochaines années. On connaît jusqu'à présent 14 exoplanètes géantes qui occultent leur étoile.[4] Dans le futur, des missions spatiales telles que *Kepler* (Koch et al., 2006) ou *CoRoT* (Aigrain et al., 2007) atteindront des précisions photométriques suffisantes pour détecter des planètes telluriques.

1.2.4 Micro-amplification gravitationnelle

Le champ gravitationnel d'une étoile peut agir comme une lentille et amplifier la brillance d'une étoile située derrière elle le long de la ligne de visée. Ce phénomène requiert l'alignement plutôt improbable de trois étoiles ; néanmoins, étant donné le très grand nombre d'étoiles dans la galaxie, il se produit assez fréquemment. Si l'étoile qui agit comme lentille gravitationnelle est orbitée par une planète, alors une deuxième amplification, plus faible, se produira lorsque la planète sera à son tour bien alignée avec

[4] *The extrasolar planets encyclopedia*, http ://exoplanet.eu/

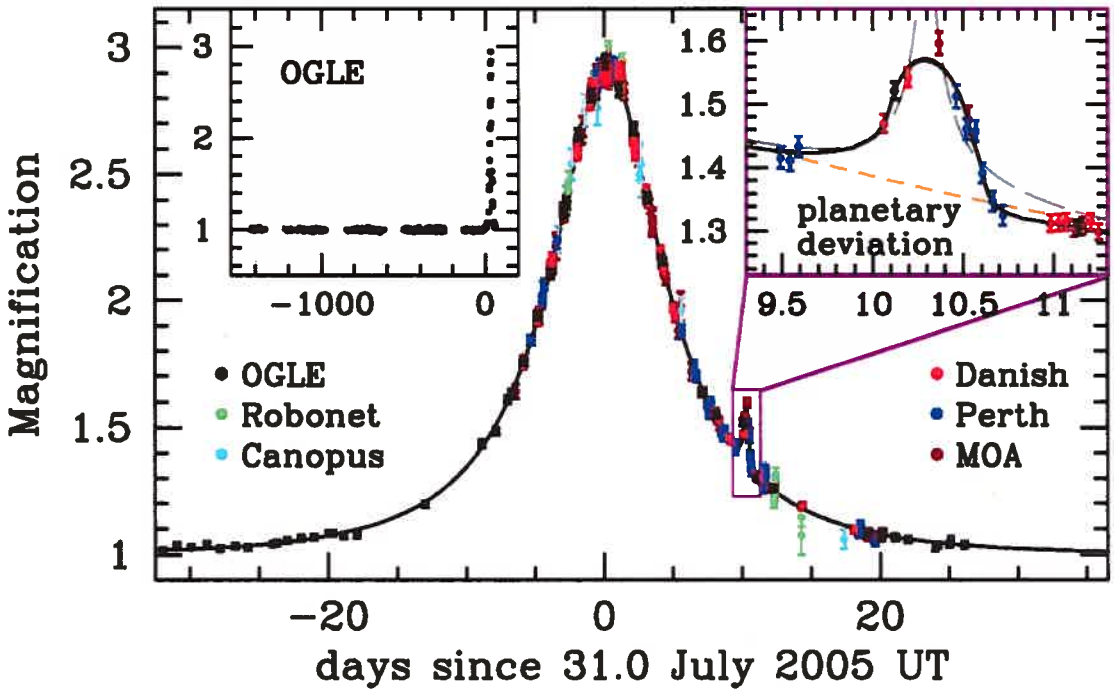

Figure 1.7 Courbe de lumière observée pendant un événement de micro-amplification gravitationnelle (OGLE 2005-BLG-390). Le plus faible pic à droite du pic principal est causé par le passage, le long de la ligne de visée, d'une planète de masse 5.5 $M_{\oplus}$ de demi-grand axe 2.6 UA orbitant l'étoile agissant comme lentille. De Beaulieu et al. (2006).

les deux autres étoiles. La Figure 1.7 montre une courbe de lumière observée pour un tel événement. Cette technique de recherche peut détecter des planètes aussi peu massives que la Terre sur des orbites de quelques UA (Rattenbury, 2006).

L'analyse assez complexe de la courbe de lumière d'un événement de micro-amplification gravitationnelle permet de déterminer la masse, le demi-grand axe, et la période de la planète (Beaulieu et al., 2006; Rattenbury, 2006). Malheureusement, l'alignement précis des étoiles et de la planète menant à l'amplification ne peut se produire qu'une seule fois, empêchant la répétition de la mesure.

Plusieurs programmes de recherche de planètes par micro-amplification gravitation-

nelle sont présentement en cours (e.g. OGLE[5], MOA[6]), et ont mené à la détection de 4 exoplanètes jusqu'à présent.[7] Deux de ces planètes sont des géantes, et les deux autres ont une masse 13 et 5.5 fois supérieure à celle de la Terre.

1.2.5 Imagerie directe

L'imagerie directe consiste à résoudre spatialement la lumière émise (ou diffusée) par une planète de celle émise par son étoile, autrement dit, il s'agit d'obtenir une image du système dans laquelle la planète peut être distinguée. Cette technique de détection est très intéressante car c'est la seule méthode qui, actuellement, pourrait détecter des planètes ayant des demi-grand axes supérieurs à 10–15 UA, pour lesquelles la période orbitale excède 25 ans. L'imagerie directe est aussi la seule méthode qui permettrait d'obtenir des mesures de photométrie, spectroscopie, ou polarimétrie pour des planètes qui n'occultent pas leur étoile primaire. Ces mesures sont essentielles pour contraindre la température et la composition atmosphérique des planètes.

La tâche est très difficile car elle requiert la détection d'une source très faible (la planète) et très rapprochée d'une source très brillante (l'étoile). Typiquement, selon son âge et sa masse, une planète géante gazeuse est d'un million à un milliard de fois moins brillante que son étoile. La séparation angulaire maximale d'une planète ayant un demi-grand axe de 1–100 UA est de $0.04''$–$4''$pour une étoile située à 25 pc du Soleil ; à ces séparations angulaires, la planète est complètement perdue dans le brillant éclat de son étoile.

Fondamentalement, l'image d'une étoile est déterminée par la fonction d'étalement de point (FÉP) du télescope utilisé pour l'observer. Par exemple, la FÉP d'un télescope ayant un miroir primaire circulaire correspond à une fonction d'Airy, qui possède un pic central entouré d'une série d'anneaux brillants dont l'intensité décroît avec la séparation angulaire. La résolution angulaire du télescope est égale à la pleine largeur à mi-hauteur

[5] http ://bulge.astro.princeton.edu/ogle/
[6] http ://www.phys.canterbury.ac.nz/moa/
[7] *The extrasolar planets encyclopedia*, http ://exoplanet.eu/

(PLMH) du pic de sa FÉP, qui est égale à λ/D dans le cas d'une fonction d'Airy, où λ est la longueur d'onde observée et D le diamètre du télescope.

À la lumière diffractée par le télescope s'ajoute la lumière diffusée par les irrégularités des surfaces optiques qui constituent le télescope et la caméra. Ces irrégularités introduisent des erreurs de phase et d'amplitude sur le front d'onde traversant le système et mènent à la formation de "points" de lumière, appelés tavelures, dans l'image de l'étoile ; ces tavelures sont essentiellement des répliques du coeur de la FÉP qui sont décalées spatialement et de moindre intensité. On qualifie les tavelures engendrées par les irrégularités de surface de *quasi-statiques* car elles ont de longues durées de vie comparativement aux temps de pose typiquement utilisés.

Pour un télescope situé au sol, la situation est plus compliquée car la turbulence atmosphérique introduit de très grandes erreurs de phase dans le front d'onde capté par le télescope, ce qui dégrade énormément la qualité de l'image. Cependant, des systèmes d'optique adaptative (OA) permettent de corriger ces erreurs de phase et obtenir une FÉP qui approche la limite de diffraction. Les erreurs résiduelles du front d'onde après correction par le système d'OA génèrent aussi des tavelures dans la FÉP. Par contre, comme la turbulence atmosphérique évolue sur une échelle de quelques millisecondes, pour une pose de plus de $\sim$1 seconde, le patron de tavelures atmosphériques aura plutôt l'aspect d'un halo de lumière diffusée.

La Figure 1.8*a* montre l'image d'une étoile (i.e. sa FÉP) obtenue avec le télescope Gemini Nord et le système d'optique adaptative Altair (Herriot et al., 2000). On peut très bien y distinguer le pic de diffraction, le halo atmosphérique, et les tavelures quasi-statiques. La Figure 1.8*b* montre, en fonction de la séparation angulaire, la brillance relative minimale d'un compagnon nécessaire pour qu'il soit détecté dans cette image. Tel que mentionné plus haut, le faible signal d'une planète géante serait indiscernable de celui de la FÉP de l'étoile.

Pour détecter une planète par imagerie directe, il faut donc parvenir à réduire l'intensité de la FÉP de l'étoile. Il existe plusieurs façons d'y parvenir, lesquelles peuvent

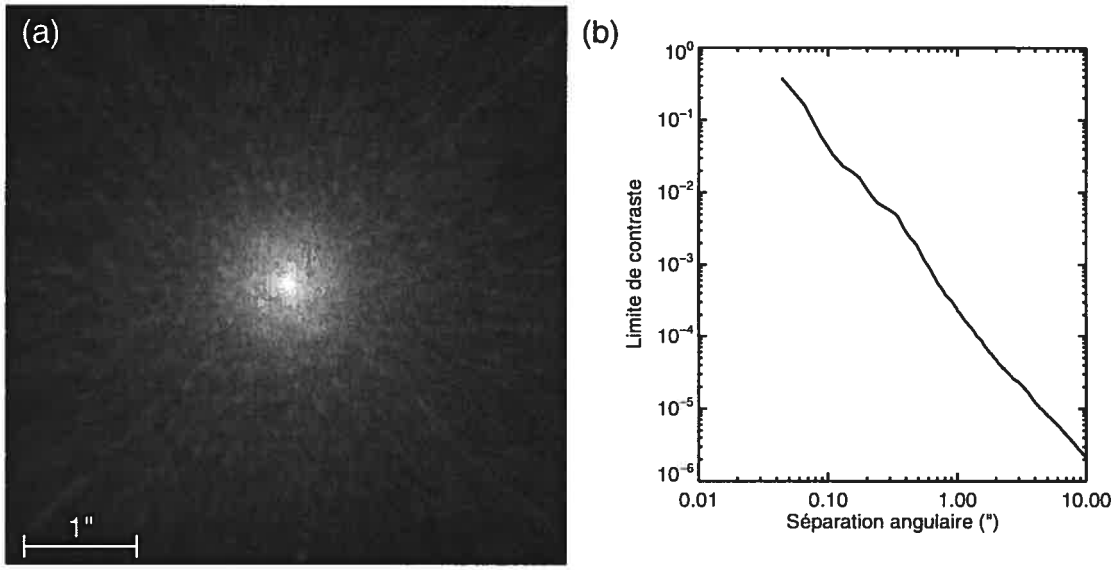

Figure 1.8 (*a*) Image d'une étoile obtenue avec le télescope Gemini Nord et le système d'optique adaptative Altair. Affichage logarithmique de 10^{-5} à 1 fois l'intensité du pic de la FÉP. (*b*) Limite de sensibilité aux compagnons faibles correspondante, exprimée en rapport de la brillance d'un compagnon sur celle de l'étoile.

être classées en deux grandes catégories : la coronographie et l'imagerie différentielle. La coronographie repose sur les principes de diffraction de la lumière et vise à bloquer la lumière d'une source alignée sur l'axe du télescope tout en laissant passer celle d'une source hors-axe. Ce but est généralement accompli en plaçant un masque, opaque ou apodisé, dans un plan focal du système optique, et un autre dans un plan pupille subséquent ; il existe cependant d'autres possibilités. Un survol des différents types de coronographes est présenté dans Guyon et al. (2006). Pour être efficace, la coronographie requiert de bons rapports de Strehl[8] (>80%, Sivaramakrishnan et al., 2001) ; de tels rapports de Strehl sont obtenus dans l'espace et pourront être atteints au sol dans quelques années avec des systèmes d'OA de nouvelle génération (Macintosh et al., 2006; Dohlen et al., 2006).

L'imagerie différentielle consiste à obtenir une image référence de la FÉP, et à sous-

[8]Le rapport de Strehl est le rapport de l'intensité au pic d'une FÉP observée sur celle d'une FÉP qui serait produite par un système d'imagerie parfait.

traire cette image référence d'une image cible pour éliminer le signal de l'étoile. L'image référence doit être une représentation aussi fidèle que possible de la FÉP de l'étoile, mais elle ne doit pas contenir l'image de la planète, sinon sa soustraction de l'image cible éliminerait la planète du même coup. L'image référence peut être celle d'une autre étoile, obtenue dans des conditions d'observation aussi semblables que possible à celles de la cible, ou elle peut être une image de la cible elle-même obtenue à une autre longueur d'onde, un autre état de polarisation, ou une autre orientation du champ de vue. Deux exemples particuliers d'imagerie différentielle sont présentés ici car ils seront abordés dans la thèse : l'imagerie différentielle spectrale simultanée (IDSS, Racine et al., 1999; Marois et al., 2000; Smith, 1987; Rosenthal et al., 1996) et l'imagerie différentielle angulaire (IDA, Marois et al., 2006).

L'IDSS consiste à obtenir simultanément l'image d'une étoile dans plusieurs bandes spectrales étroites dans une région spectrale où le spectre de l'étoile diffère significativement de celui des planètes recherchées. Au premier ordre, et en négligeant quelques complications, la FÉP de l'étoile est la même pour des longueurs d'ondes rapprochées. La combinaison et la soustraction judicieuse des images permettent donc d'éliminer le signal de l'étoile tout en gardant celui du compagnon recherché. Comme les images de la FÉP de l'étoile sont obtenues dans des bandes spectrales différentes, elles doivent être rapportées à la même échelle spatiale avant d'en faire la soustraction (l'échelle de la diffraction est proportionnelle à λ/D). L'IDSS peut donc être efficace aux plus grandes séparations angulaires, même en l'absence de différences entre le spectre de l'étoile et celui de la planète, car cette dernière ne serait pas superposée à elle-même dans les différentes images après le changement d'échelle.

L'IDA consiste à acquérir une séquence de plusieurs images de l'étoile avec un télescope altitude/azimut et le rotateur d'instrument éteint (au foyer Cassegrain) ou ajusté correctement (au foyer Nasmyth) pour garder la caméra et le télescope bien alignés au cour de la séquence. Cette configuration très stable mène à une bonne corrélation de la FÉP dans les différentes images et de plus, elle cause une rotation du champ de vue

pendant la séquence d'observation. Pour chaque image de la séquence, il est possible de construire une image référence de la FÉP à partir d'autres images de la même séquence dans lesquelles un compagnon serait suffisamment décalé à cause de la rotation du champ de vue. Après la soustraction des images références, les images résiduelles sont tournées pour aligner leur champ de vue, et elles sont co-additionnées. L'IDA est plus efficace aux grandes séparations angulaires ($\gtrsim 1''$), où la rotation de champ occasionne un déplacement linéaire du champ plus rapide.

Plusieurs recherches de planètes par imagerie directe ont été faites au cours des dernières années (Lowrance et al., 2005; Masciadri et al., 2005; Chauvin et al., 2006; Biller et al., 2006; Luhman & Jayawardhana, 2002; McCarthy & Zuckerman, 2004) ; selon la stratégie d'observation utilisée, les propriétés des étoiles visées, et les caractéristiques des instruments utilisés, ces recherches ont atteint des limites de détection de 10–13 magnitudes de contraste à des séparations angulaires de $1''$–$2''$. Ces limites permettent de détecter des planètes plus massives que $\sim 5\ M_{\rm Jup}$ à 25–100 UA autour d'étoiles âgées de $\sim$100 millions d'années situées à 25–50 pc du Soleil. Malgré ces recherches, aucune planète autour d'une étoile n'a encore été détectée par imagerie directe. Toutefois, un objet de masse planétaire (3–7 $M_{\rm Jup}$) a récemment été détecté par imagerie directe autour d'une naine brune de 25 $M_{\rm Jup}$ (Chauvin et al., 2004).

1.3 Les exoplanètes connues

On connaît aujourd'hui 216 exoplanètes[9], la très grande majorité de celles-ci ($\sim$200) ayant été découvertes par la technique de vélocimétrie. Avec un tel échantillon d'exoplanètes, qui est de plus sans cesse grandissant, il est très intéressant d'examiner leurs propriétés. D'abord, en comparant le nombre d'étoiles observées ayant au moins une planète avec le nombre total d'étoiles observées, on obtient que 6–7% des étoiles ont une planète de masse supérieure à $\sim 0.1\ M_{\rm Jup}$ et demi-grand axe inférieur à 5 UA (Marcy et al.,

[9]Mars 2007, *The extrasolar planets encyclopedia*, http ://exoplanet.eu/

2005). Ce pourcentage constitue une limite inférieure car les recherches de planètes par vélocimétrie sont grandement incomplètes pour des demi-grand axes supérieurs à 3 UA. Parmi les étoiles ayant au moins une planète détectée, 14% en possèdent une autre ou plus ; deux systèmes multiples comptent quatre planètes et quatre en comptent trois.

La Figure 1.9*a* montre la distribution des masses (minimum) des exoplanètes connues. Bien que la technique de vélocimétrie soit plus sensible aux planètes plus massives, cette distribution augmente très rapidement pour les plus faibles masses. La partie à plus faible masse de cette distribution est affectée par l'incomplétude des recherches par vélocimétrie.

La Figure 1.9*b* montre la distribution en demi-grand axe des exoplanètes ; cette distribution s'étend de 0.02 UA à $\sim$5 UA. La limite supérieure, qui correspond à une période orbitale de $\sim$10 ans, reflète le temps écoulé depuis le début des principaux programmes de recherche de planètes par vélocimétrie. La distribution en demi-grand axe des planètes découvertes par vélocimétrie ne s'étendra qu'au plus à 7–8 UA dans une dizaine d'années. À partir de $\sim$0.5 UA, le nombre de planètes connues augmente rapidement avec le demi-grand axe jusqu'à environ 3 UA, où les recherches commencent à être grandement affectées par l'incomplétude. Les données actuelles suggèrent donc qu'il y ait encore plus de planètes avec un demi-grand axe supérieur à $\sim$3 UA. Il y a une population importante de planètes avec un demi-grand axe inférieur à 0.1 UA, qu'on appelle les "Jupiters chaudes" ; ces planètes sont présentes autour d'environ 1.2% des étoiles (Marcy et al., 2005). L'existence de telles planètes était complètement inattendue car aucun des mécanismes de formation de planètes géantes ne peut opérer à d'aussi petites séparations. Ces planètes ont donc dû migrer vers leur étoile après leur formation dans une région plus éloignée.

La Figure 1.9*c* montre un diagramme de la masse minimum des exoplanètes en fonction de leur demi-grand axe. Ce diagramme montre qu'il y a un déficit de planètes massives à petites séparations ; ceci n'est pas le résultat d'un biais observationnel car les recherches par vélocimétrie sont plus sensibles aux planètes plus massives sur de plus

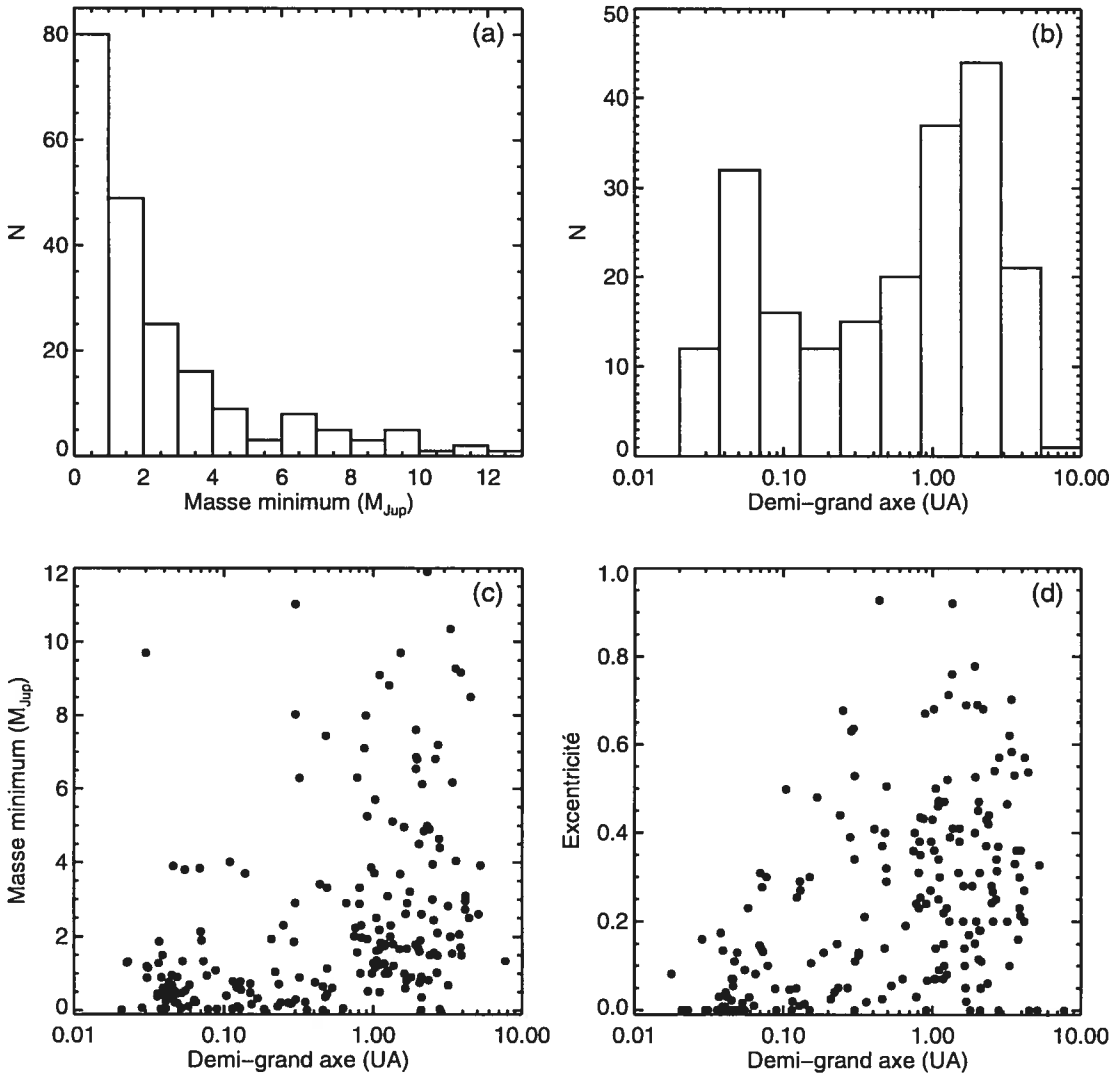

Figure 1.9 Quelques propriétés de la population d'exoplanètes connues. Données tirées de *The extrasolar planets encyclopedia*, http ://exoplanet.eu/. La masse réelle, et non la masse minimum, est montrée pour les planètes dont l'inclinaison orbitale est connue et pour celles découvertes par une méthode autre que la vélocimétrie.

petites orbites. Par contre, le manque apparent de planètes moins massives à plus grande séparation est probablement un biais observationnel car ces planètes sont plus difficiles à détecter.

Un graphique excentricité–demi-grand axe des exoplanètes connues est montré à la Figure 1.9*d*. Les planètes ayant un petit demi-grand axe ont une faible excentricité, qui découle fort probablement d'une circularisation par effet marémoteur. À plus grandes séparations, où le temps de circularisation est plus long que l'âge du système, la dispersion en excentricité des exoplanètes est remarquable, particulièrement considérant que les planètes géantes du système solaire ont toutes une excentricité inférieure à 0.06.

1.4 Cette thèse

Le but premier de cette thèse est la recherche de planètes géantes par imagerie directe afin de complémenter les recherches par vélocimétrie et de découvrir des planètes qui pourront ensuite être étudiées en détail par photométrie ou spectroscopie. Tel que mentionné précédemment, il s'agit d'une tâche très difficile qui requiert l'atténuation de la FÉP de l'étoile observée ; l'approche retenue pour ce travail est l'imagerie différentielle. Dans un premier temps, deux outils pour améliorer la qualité de la soustraction de la FÉP de l'étoile en imagerie différentielle sont développés. Ensuite, une importante campagne d'observation visant la détection de planètes géantes par imagerie directe est présentée.

Le chapitre 2 présente un nouveau concept instrumental permettant d'améliorer la corrélation des images obtenues à différentes longueurs d'onde en IDSS. Un prototype de caméra basé sur ce concept a été réalisé et testé au laboratoire d'Astrophysique Expérimentale de l'Université de Montréal. Ce chapitre présente le concept en détail, des estimés de performance basés sur des simulations numériques, une description du prototype réalisé en laboratoire et les résultats obtenus avec celui-ci, et enfin, une discussion de l'impact que pourrait avoir l'amélioration obtenue en laboratoire sur la recherche de

planètes et de la facilité d'implémenter le concept dans des instruments déjà existants.

Le chapitre 3 présente un nouvel algorithme permettant de combiner plusieurs images références de la FÉP de l'étoile en une image référence plus fidèle à l'image cible, ce qui permet d'effectuer une meilleure soustraction de la lumière de l'étoile. L'algorithme développé est général et peut être utilisé avec plusieurs types de données d'imagerie différentielle : images à plusieurs longueurs d'onde, images avec différentes orientations du champ de vue, images d'étoiles différentes. Dans ce chapitre l'algorithme est d'abord présenté en détail, et il est ensuite appliqué à une séquence d'IDA pour en illustrer les performances.

Finalement, le chapitre 4 présente le *Gemini Deep Planet Survey — GDPS*, une recherche de planètes géantes autour d'étoiles jeunes du voisinage solaire. Cette campagne de recherche a été menée avec le télescope Gemini Nord en utilisant l'IDA pour soustraire la FÉP de l'étoile centrale. Ce travail a bénéficié directement de l'algorithme développé au chapitre 3. Sont présentés dans l'ordre, les détails de la sélection de l'échantillon d'étoiles cibles, les observations, l'analyse des données, les sensibilités de détection atteintes, et l'identification et le suivi de candidates exoplanètes détectées. Aucune exoplanète n'a été découverte malgré les très bonnes sensibilités atteintes. Une analyse statistique des résultats, permettant de déterminer une limite supérieure à la fraction d'étoiles avec au moins une planète géante dans différents intervalles de masses et de séparations orbitales, est enfin présentée.

1.5 Déclaration de l'étudiant

J'ai écrit les trois articles présentés dans cette thèse, et j'ai accompli les travaux qui y sont présentés. Pour le premier article (chapitre 2), j'ai développé le modèle semi-analytique et fait les simulations numériques pour estimer l'atténuation possible avec ce concept de caméra. J'ai conçu et assemblé le prototype de caméra utilisé pour valider le concept proposé, et j'ai pris et analysé les données avec ce prototype. Finalement, j'ai fait

les simulations Monte Carlo pour estimer l'impact scientifique qu'aurait la performance atteinte en laboratoire.

L'algorithme présenté dans le deuxième article (chapitre 3) est l'aboutissement d'un travail que C. Marois et moi avons fait en proche collaboration sur une période de plusieurs mois. Pour cet article, j'ai perfectionné l'algorithme mis au point, conçu la méthode utilisée pour vérifier ses performances et optimiser son application. J'ai aussi fait toutes les analyses qui y sont présentées.

Pour le troisième article (chapitre 4), j'ai fait la sélection de l'échantillon d'étoiles cibles et la recherche de la littérature pour établir leurs propriétés. J'ai planifié toutes les observations, fait le dépouillement des données, et analysé les résultats. Finalement, j'ai fait, conjointement avec R. Doyon, l'analyse statistique portant sur la fraction d'étoiles ayant au moins une planète géante.

R. Doyon et D. Nadeau ont supervisé l'écriture de tous les articles, et leur travail rigoureux de révision a grandement contribué à en améliorer la qualité.

Bibliographie

Aigrain, S., Barge, P., Deleuil, M., Fressin, F., Moutou, C., Queloz, D., Auvergne, M., Baglin, A., & the CoRoT Exoplanet Science Team. 2007, ArXiv Astrophysics e-prints, astro-ph/0702062

Alibert, Y., Mordasini, C., Benz, W., & Winisdoerffer, C. 2005, A&A, 434, 343

Allard, F., Hauschildt, P. H., Alexander, D. R., Tamanai, A., & Schweitzer, A. 2001, ApJ, 556, 357

Alonso, R. et al. 2004, ApJ, 613, L153

Baraffe, I., Chabrier, G., Barman, T. S., Allard, F., & Hauschildt, P. H. 2003, A&A, 402, 701

Bate, M. R., & Bonnell, I. A. 2005, MNRAS, 356, 1201

Beaulieu, J.-P. et al. 2006, Nature, 439, 437

Benedict, G. F. et al. 2002, ApJ, 581, L115

Biller, B. A. et al. 2006, in IAU Colloq. 200 : Direct Imaging of Exoplanets : Science & Techniques, ed. C. Aime & F. Vakili, 53–60

Boss, A. P. 1997, Science, 276, 1836

—. 2001, ApJ, 563, 367

Brown, T. M., Charbonneau, D., Gilliland, R. L., Noyes, R. W., & Burrows, A. 2001, ApJ, 552, 699

Burrows, A., Hubbard, W. B., Lunine, J. I., & Liebert, J. 2001, Reviews of Modern Physics, 73, 719

Burrows, A. et al. 1997, ApJ, 491, 856

Cameron, A. C. et al. 2007, MNRAS, 375, 951

Campbell, B., Walker, G. A. H., & Yang, S. 1988, ApJ, 331, 902

Chabrier, G., Baraffe, I., Allard, F., & Hauschildt, P. 2000, ApJ, 542, 464

Chambers, J. E. 2006, ApJ, 652, L133

Charbonneau, D. et al. 2005, ApJ, 626, 523

Charbonneau, D., Brown, T. M., Burrows, A., & Laughlin, G. 2007, in Protostars and Planets V, ed. B. Reipurth, D. Jewitt, & K. Keil, 701–716

Charbonneau, D., Brown, T. M., Latham, D. W., & Mayor, M. 2000, ApJ, 529, L45

Charbonneau, D., Brown, T. M., Noyes, R. W., & Gilliland, R. L. 2002, ApJ, 568, 377

Chatterjee, S., Ford, E. B., & Rasio, F. A. 2007, ArXiv Astrophysics e-prints

Chauvin, G., Lagrange, A.-M., Dumas, C., Zuckerman, B., Mouillet, D., Song, I., Beuzit, J.-L., & Lowrance, P. 2004, A&A, 425, L29

Chauvin, G., Lagrange, A.-M., Udry, S., Fusco, T., Galland, F., Naef, D., Beuzit, J.-L., & Mayor, M. 2006, A&A, 456, 1165

Deming, D., Seager, S., Richardson, L. J., & Harrington, J. 2005, Nature, 434, 740

Dohlen, K. et al. 2006, in Proc. SPIE, Vol. 6269, Ground-based and Airborne Instrumentation for Astronomy, ed. I. S. McLean & M. Iye, 62690Q

Goldreich, P., & Tremaine, S. 1980, ApJ, 241, 425

Grillmair, C. J., Charbonneau, D., Burrows, A., Armus, L., Stauffer, J., Meadows, V., Van Cleve, J., & Levine, D. 2007, ApJ, 658, L115

Guyon, O., Pluzhnik, E. A., Kuchner, M. J., Collins, B., & Ridgway, S. T. 2006, ApJS, 167, 81

Haisch, Jr., K. E., Lada, E. A., & Lada, C. J. 2001, ApJ, 553, L153

Hale, A. 1995, PASP, 107, 22

Hatzes, A. P., Cochran, W. D., Endl, M., McArthur, B., Paulson, D. B., Walker, G. A. H., Campbell, B., & Yang, S. 2003, ApJ, 599, 1383

Henry, G. W., Marcy, G. W., Butler, R. P., & Vogt, S. S. 2000, ApJ, 529, L41

Herriot, G. et al. 2000, in Proc. SPIE, Vol. 4007, Adaptive Optical Systems Technology, ed. P. L. Wizinowich, 115–125

Hubbard, W. B., Burrows, A., & Lunine, J. I. 2002, ARA&A, 40, 103

Inaba, S., Wetherill, G. W., & Ikoma, M. 2003, Icarus, 166, 46

Koch, D. et al. 2006, Ap&SS, 304, 391

Konacki, M., Torres, G., Jha, S., & Sasselov, D. D. 2003, Nature, 421, 507

Latham, D. W., Stefanik, R. P., Mazeh, T., Mayor, M., & Burki, G. 1989, Nature, 339, 38

Levison, H. F., Morbidelli, A., Gomes, R., & Backman, D. 2007, in Protostars and Planets V, ed. B. Reipurth, D. Jewitt, & K. Keil, 669–684

Lin, D. N. C., Bodenheimer, P., & Richardson, D. C. 1996, Nature, 380, 606

Lowrance, P. J. et al. 2005, AJ, 130, 1845

Luhman, K. L., & Jayawardhana, R. 2002, ApJ, 566, 1132

Macintosh, B. et al. 2006, in Proc. SPIE, Vol. 6272, Advances in Adaptive Optics II, ed. B. L. Ellerbroek & D. Bonaccini Calia, 62720L

Marcy, G., Butler, R. P., Fischer, D., Vogt, S., Wright, J. T., Tinney, C. G., & Jones, H. R. A. 2005, Progress of Theoretical Physics Supplement, 158, 24

Marois, C., Doyon, R., Racine, R., & Nadeau, D. 2000, PASP, 112, 91

Marois, C., Lafrenière, D., Doyon, R., Macintosh, B., & Nadeau, D. 2006, ApJ, 641, 556

Marr, IV, J. C. 2006, in Proc. SPIE, Vol. 6268, Advances in Stellar Interferometry., ed. S. M. Monnier, J. D. & C. Danchi, 626822

Masciadri, E., Mundt, R., Henning, T., Alvarez, C., & Barrado y Navascués, D. 2005, ApJ, 625, 1004

Mayor, M., & Queloz, D. 1995, Nature, 378, 355

Mazeh, T., Latham, D. W., & Stefanik, R. P. 1996, ApJ, 466, 415

McCarthy, C., & Zuckerman, B. 2004, AJ, 127, 2871

Mignard, F. 2005, in ASP Conf. Ser. 338 : Astrometry in the Age of the Next Generation of Large Telescopes, ed. P. K. Seidelmann & A. K. B. Monet, 15

Murray, N., Hansen, B., Holman, M., & Tremaine, S. 1998, Science, 279, 69

Pollack, J. B., Hubickyj, O., Bodenheimer, P., Lissauer, J. J., Podolak, M., & Greenzweig, Y. 1996, Icarus, 124, 62

Racine, R., Walker, G. A. H., Nadeau, D., Doyon, R., & Marois, C. 1999, PASP, 111, 587

Rasio, F. A., & Ford, E. B. 1996, Science, 274, 954

Rattenbury, N. J. 2006, Modern Physics Letters A, 21, 919

Reipurth, B., & Clarke, C. 2001, AJ, 122, 432

Richardson, L. J., Deming, D., Horning, K., Seager, S., & Harrington, J. 2007, Nature, 445, 892

Rosenthal, E. D., Gurwell, M. A., & Ho, P. T. P. 1996, Nature, 384, 243

Rupprecht, G. et al. 2004, in Proc. SPIE, Vol. 5492, Ground-based Instrumentation for Astronomy, ed. A. F. M. Moorwood & M. Iye, 148–159

Shen, S., & Wadsley, J. 2006, ApJ, 651, L145

Sivaramakrishnan, A., Koresko, C. D., Makidon, R. B., Berkefeld, T., & Kuchner, M. J. 2001, ApJ, 552, 397

Smith, W. H. 1987, PASP, 99, 1344

Tanaka, H., Takeuchi, T., & Ward, W. R. 2002, ApJ, 565, 1257

Veras, D., & Armitage, P. J. 2004, MNRAS, 347, 613

Walker, G. A. H., Bohlender, D. A., Walker, A. R., Irwin, A. W., Yang, S. L. S., & Larson, A. 1992, ApJ, 396, L91

Weidenschilling, S. J., & Marzari, F. 1996, Nature, 384, 619

CHAPITRE 2

AMÉLIORATION DE L'ATTÉNUATION DU BRUIT DE TAVELURE EN IMAGERIE DIFFÉRENTIELLE SPECTRALE SIMULTANÉE AVEC UN DIFFUSEUR HOLOGRAPHIQUE AU PLAN FOCAL

IMPROVING THE SPECKLE NOISE ATTENUATION OF SIMULTANEOUS SPECTRAL DIFFERENTIAL IMAGING WITH A FOCAL PLANE HOLOGRAPHIC DIFFUSER

DAVID LAFRENIÈRE[a], RENÉ DOYON[a], DANIEL NADEAU[a], ÉTIENNE ARTIGAU[a,b], CHRISTIAN MAROIS[c], AND MATHILDE BEAULIEU[a]

Published in: *The Astrophysical Journal*, v.661, p.1208 (2007)

Abstract

Direct exoplanet detection is limited by speckle noise in the point spread function (PSF) of the central star. This noise can be reduced by subtracting PSF images obtained simultaneously in adjacent narrow spectral bands using a multi-channel camera (MCC), but only to a limit imposed by differential optical aberrations in the MCC. To alleviate this problem, we suggest the introduction of a holographic diffuser at the focal plane of the MCC to convert the PSF image into an incoherent illumination scene that is then re-imaged with the MCC. The re-imaging is equivalent to a convolution of the scene with the PSF of each spectral channel of the camera. Optical aberrations in the MCC

[a]Département de physique and Observatoire du Mont Mégantic, Université de Montréal, C.P. 6128, Succ. Centre-Ville, Montréal, QC, Canada H3C 3J7

[b]Gemini Observatory, Southern Operations Center, Association of Universities for Research in Astronomy, Inc., Casilla 603, La Serena, Chile

[c]Institute of Geophysics and Planetary Physics L-413, Lawrence Livermore National Laboratory, 7000 East Ave, Livermore, CA 94550

affect only the convolution kernel of each channel and not the PSF globally, resulting in better correlated images. We report laboratory measurements with a dual channel prototype (1.575 μm and 1.625 μm) to validate this approach. A speckle noise suppression factor of 12-14 was achieved, an improvement by a factor $\sim$5 over that obtained without the holographic diffuser. Simulations of realistic exoplanet populations for three representative target samples show that the increase in speckle noise attenuation achieved in the laboratory would roughly double the number of planets that could be detected with current adaptive optics systems on 8-m telescopes.

Subject headings: Instrumentation: adaptive optics — planetary systems — stars: imaging — techniques: image processing — techniques: high angular resolution

2.1 Introduction

Direct detections of faint exoplanets near bright stars are essential to extend the census of planetary companions to separations that are beyond the reach of radial velocity surveys and to enable measurements of exoplanets' physical properties through follow-up multi-color photometry and spectroscopy. This difficult endeavour, already being tackled by many, is one of the major goals for next generation instruments on 8-m class telescopes and future 30- to 100-m telescopes. The main difficulty stems from imperfections in the optics that produce bright quasi-static speckles in the point spread function (PSF) of the central star (Marois et al., 2005; Biller et al., 2004; Masciadri et al., 2005). The subtraction of reference PSF images is a very efficient way of reducing this speckle noise. A good example is angular differential imaging (ADI, Marois et al., 2006; Lafrenière et al., 2007), in which images of the target, obtained while the field of view rotates, are used for subtracting the stellar PSF. This technique is among the most successful at suppressing speckle noise for ground-based imaging; however, it is inefficient at small angular separation ($\lesssim 1''$) because the time required for sufficient natural rotation of the field of view is too long.

Simultaneous spectral differential imaging (SSDI) is a PSF subtraction technique that is efficient at all angular separations. It consists in the simultaneous acquisition of images in adjacent narrow spectral bands within a spectral range where the stellar and planetary spectra differ appreciably (Racine et al., 1999; Marois et al., 2000; Smith, 1987; Rosenthal et al., 1996). Judicious image combination and subtraction removes the stellar PSF and leaves that of any companion. Note that because the PSF images are acquired in different bandpasses, they must be rescaled prior to subtraction (diffraction scales as λ). At larger separations, this scaling allows the technique to work even in the absence of differential spectral features since a companion would not overlie itself in the rescaled images.

The standard implementation of SSDI is done with a multi-channel camera (MCC). The speckle noise suppression achievable with such instruments is hampered by differential aberrations between the spectral channels (Marois et al., 2005). For the triple imager TRIDENT (Marois et al., 2005, Canada-France-Hawaii Telescope) and the quadruple imager SDI (Lenzen et al., 2004, Very Large Telescope), the subtraction of two images obtained simultaneously through different channels yields a speckle noise attenuation of only $\sim$2-2.5 (Marois et al., 2005 and Appendix 2.A). Strategies such as multiple rotations of the instrument or observation of reference stars (Marois et al., 2005; Biller et al., 2004) have been used to attenuate further the residuals left by the incomplete simultaneous multi-channel subtraction, and 5σ contrast limits for magnitude differences of $\sim$9 and $\gtrsim$10 have been achieved at an angular separation of $0\farcs5$ with TRIDENT and SDI respectively (Marois et al., 2005; Biller et al., 2006). However, the approaches used to circumvent the problem of differential aberrations often complicate data acquisition and decrease the observing efficiency at the telescope. As several MCCs are currently being developed by major observatories for future exoplanet searches, e.g. NICI (Toomey & Ftaclas, 2003) for Gemini South, SPHERE/IRDIS (Dohlen et al., 2006) for the VLT, or HiCIAO (Tamura et al., 2006; Hodapp et al., 2006) for Subaru, the development of techniques to improve the PSF subtraction performance of MCCs is of great interest.

In this paper, we propose to minimize the effect of differential aberrations by introducing a holographic diffuser (HD) at the focal plane of an MCC (see also Lafrenière et al., 2006). This simple approach provides a direct gain in speckle attenuation without the need to modify the observing strategy. The concept and performance estimates are presented in §2.2. Measurements and results using a laboratory prototype are reported in §2.3, and §2.4 presents estimates of the detection limits that such a device should reach on 8-m telescopes using current adaptive optics (AO) systems, along with an assessment of the corresponding exoplanet detection efficiency. Improvements in performance for a dedicated camera, implications of the laboratory results for other types of SSDI instruments, and considerations for implementation of this concept in an existing camera are discussed in §2.5.

2.2 Multi-channel imager with holographic diffuser

2.2.1 Concept

A light shaping HD is a random surface relief hologram that diffuses the light incident upon it into a controlled angular distribution. When a coherent wavefront goes through an ideal HD, large phase errors are introduced over small scales and spatial coherence is lost; thus, every point of the wavefront effectively becomes an independent source emitting with an angular distribution controlled by the HD. Hence, an HD located at a focal plane converts the PSF image into an incoherent illumination scene, which can then be re-imaged by an MCC. This is equivalent to a convolution of the scene with the PSF of each channel of the MCC. Optical aberrations in the MCC affect only the convolution kernel of each channel rather than the PSF globally; the effect of differential aberrations is merely a convolution of the same PSF image with different kernels. Hence, contrary to standard MCC imaging, the speckle pattern remains the same in all channels and it is only the light distribution within each speckle that may vary slightly depending on the size of the convolution kernel and on the amount of aberrations present

in the MCC. If the size of the convolution kernel is smaller than the size of a speckle in the incident PSF image, then most of the light will remain inside the same speckle after convolution and the correlation between the different channels will be high.

An HD is a better choice than other diffuser types for use with an MCC because its diffusing cone angle can be made small, allowing efficient coupling to relatively large $f/\#$ ($\sim$8-32), typical of existing cameras. Moreover, the diffusing properties of an HD are wavelength independent. It should be noted that since the diffuser breaks the coherence of the wavefront, it precludes the use of a coronagraph downstream from it. However, the diffuser poses no problem for a coronagraph placed in front of it.

A real HD does not behave exactly as described above because the size of the structures on its surface is not nnegligible compared to the full-width-at-half-maximum (FWHM) of the incident PSF. The surface of an HD can be thought of as a random collection of microlenses, each refracting light slightly differently such that the overall diffusion of light results in the desired angular distribution. A real HD thus transforms the wavefront incident upon it into a random collection of sources, or micro-pupils, of finite size rather than ideal, infinitesimally spaced, point sources. Accordingly, the image recorded by an MCC equipped with a focal plane HD would correspond to the smooth illumination scene incident upon the HD broken up into many tiny spots, whose position and intensity are determined by the position and amount of light intercepted by the corresponding microlenses (see Figure 2.1). As the micro-pupils produced by the microlenses are usually not resolved by the MCC, the shape, or FWHM, of each tiny spot is determined by the focal ratio of the MCC. This breakup of the smooth illumination scene into a collection of tiny spots is problematic, but a simple solution exists. If the HD is moved slightly in a plane tangent to its surface, then each tiny spot will move on the detector by a corresponding amount, and the intensity of each spot will change according to the new amount of light intercepted by the corresponding microlens. In the limit where the HD moves continuously during an exposure, the detector is smoothly illuminated and, effectively, the image recorded by the MCC corresponds to a convolution of the illumination

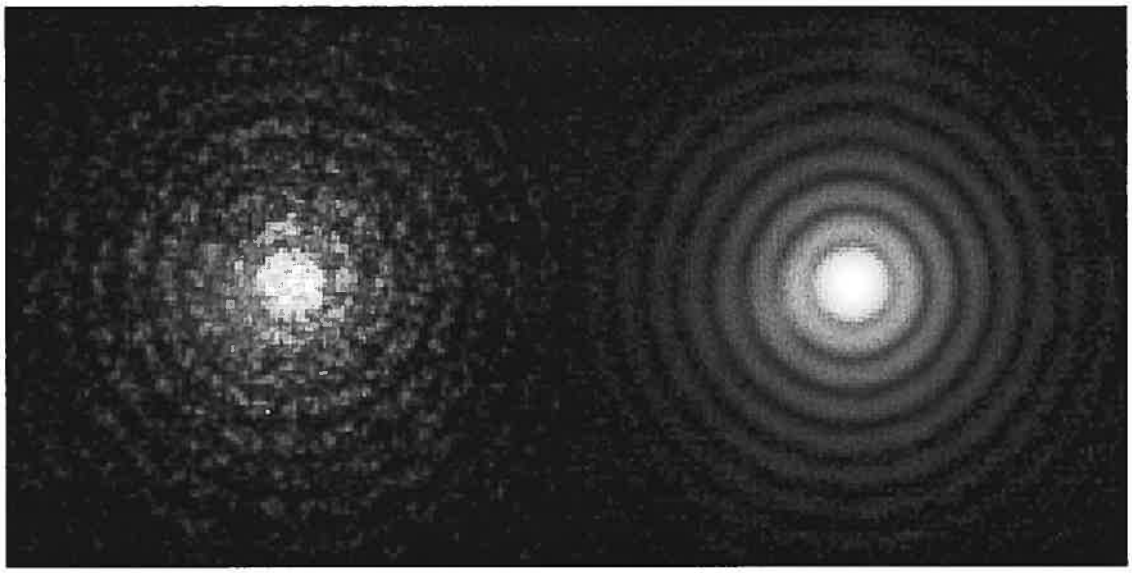

Figure 2.1 Images of a PSF obtained with a camera equipped with an HD at its entrance focal plane. The HD was fixed (*left*) or moving continuously (*right*) during the exposure; see §2.2.1 for more detail. The images are shown with a logarithmic intensity scale. They were acquired using the experimental setup described in §2.3.1.

scene incident upon the HD with the PSF of the MCC (see Figure 2.1).

The imaging process described above can be understood mathematically as follows. If I_1 and I_2 represent the PSFs of the two channels of a dual imager for a point source located at its entrance focal plane, and I_{inc} represents the PSF incident upon the HD, then the resulting image, in each channel, is given by the convolution $I_{\text{inc}} \star I_1$ or $I_{\text{inc}} \star I_2$. The residual image R obtained by subtracting the images of both channels is then given by

$$R = (I_{\text{inc}} \star I_1) - (I_{\text{inc}} \star I_2) = I_{\text{inc}} \star (I_1 - I_2). \tag{2.1}$$

The residual image can thus be viewed as being equal to the difference of the two MCC PSFs, convolved with the PSF incident upon the HD. As the spatial scale of the residual noise in $(I_1 - I_2)$ is the FWHM of I_1 and I_2, denoted θ_{MCC}, and the width of the convolution kernel is the FWHM of I_{inc}, denoted θ_{inc}, the above convolution should reduce the amplitude of the residual noise in $(I_1 - I_2)$ by a factor dependent upon the ratio

$\theta_{inc}/\theta_{MCC}$. This ratio represents the number of characteristic lengths over which the residuals are averaged by the convolution. A larger ratio $\theta_{inc}/\theta_{MCC}$ should lead to a larger attenuation of the noise.

It was demonstrated in Marois et al. (2005) that the noise attenuation achieved by a dual imager is given by $\sigma_{MCC}/\Delta\sigma_{MCC}$, where σ_{MCC} is the amount of aberration in each channel and $\Delta\sigma_{MCC}$ is the amount of differential aberration. Thus when using an HD one can expect, based on Eq. (2.1), that the residual noise also scales as $\sigma_{MCC}/\Delta\sigma_{MCC}$, but with an additional factor due to the convolution. While one should still minimize differential aberrations to maximize the attenuation, important leverage is introduced through the ratio $\theta_{inc}/\theta_{MCC}$, or equivalently through $(f/\#)_{inc}/(f/\#)_{MCC}$, where $(f/\#)_{inc}$ and $(f/\#)_{MCC}$ are the focal ratios of the beam incident upon the HD and of the MCC. For better performance, these ratios should be made as large as possible. This would also minimize the loss in spatial resolution resulting from the convolution of I_{inc} with I_1 or I_2. From convolutions of Airy functions, it can be shown that the loss in resolution is $\sim$12% for $(f/\#)_{inc}/(f/\#)_{MCC} = 2$ and less than 5% for $(f/\#)_{inc}/(f/\#)_{MCC} \geq 3$.

2.2.2 Speckle noise attenuation estimation

Numerical simulations were done to estimate the speckle noise attenuation that may be achieved with a dual channel camera equipped with an HD. For each simulation, three PSFs were created: the PSF incident upon the HD (I_{inc}) and the PSFs of both channels of the MCC (I_1 and I_2). Arrays of 2048×2048 pixels were used for all calculations. The PSFs were obtained as the square modulus of the Fourier Transform of the complex pupil function. The MCC PSFs FWHM, θ_{MCC}, was fixed to 5 pixels, and the incident PSF FWHM, θ_{inc}, was varied to test the effect of the ratio $\theta_{inc}/\theta_{MCC}$. Wavefront aberrations having a power-law power spectrum of index -2.7, a value appropriate for AO systems and astronomical cameras (Marois et al., 2005), were included in the simulations. Different values of the wavefront error of the incident PSF σ_{inc}, of σ_{MCC}, and of $\Delta\sigma_{MCC}$ were tried to see their effect.

Table 2.1. Speckle noise attenuation from numerical simulations.

Optical aberrations			Att. for $\theta_{inc}/\theta_{MCC}$ equal to				Fit of Eq. (2.2)	
σ_{inc}	σ_{MCC}	$\frac{\sigma_{MCC}}{\Delta\sigma_{MCC}}$	1	2	3	4	α	β
80	50	1	2.1	6.9	15.2	25.3	2.1	1.80
80	50	2	4.1	13.4	29.5	49.3	2.0	1.80
80	50	3	6.1	20.0	44.2	73.8	2.0	1.81
80	25	1	4.1	16.2	37.6	65.7	4.1	2.01
80	25	2	8.1	32.1	74.5	130.3	4.0	2.01
80	25	3	12.2	48.0	111.6	195.2	4.0	2.01
120	50	1	3.8	13.4	27.7	42.9	3.9	1.76
120	50	2	7.4	26.0	54.1	83.7	3.8	1.76
120	50	3	11.0	38.8	81.0	125.8	3.7	1.77
120	25	1	8.2	31.9	70.7	115.5	8.3	1.92
120	25	2	16.2	63.0	139.9	228.2	8.2	1.92
120	25	3	24.3	94.3	209.4	342.3	8.2	1.92

Once the three PSFs have been obtained, I_1 and I_2 are normalized to a sum of unity and are subtracted from each other. This difference is then convolved with I_{inc} to obtain the residual image. The noise attenuation is finally determined. The PSF noise is defined as the standard deviation over an annulus of the PSF image after subtraction of an azimuthally averaged profile. The noise attenuation η is defined as the ratio of the PSF noise in one channel over the noise in the residual image. Many values of $\theta_{inc}/\theta_{MCC}$, σ_{inc}, σ_{MCC}, and $\Delta\sigma_{MCC}$ were tried; the results are presented in Table 2.1 and Figure 2.2. We note that the total amount of static aberration for TRIDENT at the CFHT was estimated at 130 nm, of which 50 nm originated from the camera, and 120 nm originated from the AO system and telescope (Marois et al., 2005); the values of σ_{inc} and σ_{MCC} tested here are therefore representative of real systems. The results indicate that the noise attenuation increases with $\sigma_{MCC}/\Delta\sigma_{MCC}$ and with $\theta_{inc}/\theta_{MCC}$, in agreement with the previous discussion.

Using a dual channel camera, the maximum value of the attenuation, limited by chro-

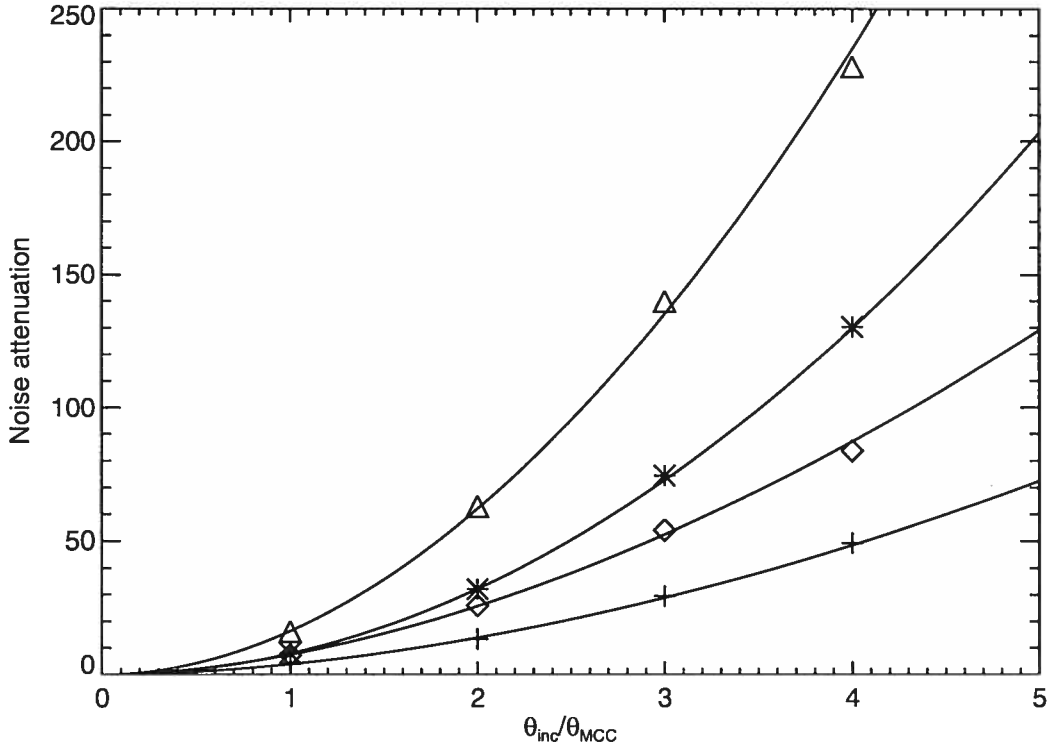

Figure 2.2 Speckle noise attenuation from numerical simulations as a function of $\theta_{inc}/\theta_{MCC}$, the ratio of the FWHM of the PSF incident on the HD over that of the intrinsic MCC PSF. The values of σ_{inc} and σ_{MCC}, in nm, are respectively 80 and 50 (*crosses*), 80 and 25 (*stars*), 120 and 50 (*diamonds*), and 120 and 25 (*triangles*). All results are for $\sigma_{MCC}/\Delta\sigma_{MCC} = 2$. The curves are the fit of Eq. (2.2) to each set of points.

maticity of the PSF, is equal to $\lambda/\Delta\lambda$ (Marois et al., 2000, 2005), where λ is the wavelength of the first channel and $\Delta\lambda$ is the difference in wavelength of the two channels. The maximum attenuation is thus ~30 for bandpasses located just outside and just inside the methane absorption feature in the spectrum of cold dwarfs at ~1.6 μm (e.g. $\lambda_1 \sim 1.575\mu$m and $\lambda_2 \sim 1.625\mu$m). From Table 2.1, the attenuation should be limited by chromaticity of the PSFs rather than by differential aberrations for $(f/\#)_{inc}/(f/\#)_{MCC} \gtrsim$3-4.

It is found that the attenuation is very well approximated by the function

$$\eta = \alpha \left(\frac{\sigma_{MCC}}{\Delta\sigma_{MCC}}\right) \left(\frac{\theta_{inc}}{\theta_{MCC}}\right)^{\beta}, \tag{2.2}$$

where α and β are parameters that depend upon σ_{inc} and σ_{MCC} (see Figure 2.2); their values are indicated in Table 2.1. Thus in a regime representative of real AO systems and MCC cameras, the attenuation that may be achieved with a system equipped with an HD roughly scales as the square of $\theta_{inc}/\theta_{MCC}$.

2.3 Experimental results

2.3.1 Dual imager testbed

A simple testbed operating in the 1.55-1.65 μm wavelength range was assembled on an optical bench to validate the concept presented in the last section. The experimental setup consists of a PSF generating system followed by a two-channel camera.

The PSF generating imaging system is composed of a bi-convex and a plano-convex lens (Thorlabs, LB1056 and LA1172) and a 6.3 mm diameter pupil stop, which is located immediately before the first lens. The system is telecentric and has an exit focal ratio of $(f/\#)_{inc} = 64$. This focal ratio was chosen based on the results of the previous section and the $f/16$ focal ratio of the dual imager described below. The PSF is generated by imaging a 25 μm pinhole illuminated from the back by a white light source. Due to the small number of optical components in this system and to the small dimension of the beam, the Strehl ratio achieved is very high and no speckles are visible in the resulting PSF image. This is problematic for testing a technique aimed specifically at reducing speckle noise; it was thus necessary to introduce more aberrations in the system. This was achieved by placing an H-band filter just before the pupil of the system, resulting in a Strehl ratio of $\sim$92%, or $\sim$75 nm rms of aberrations.

The exit focal plane of the PSF generating system corresponds to the entrance focal plane of the two-channel camera. An HD can be put in/taken out of the light path at this precise location without altering any other part of the setup. For reasons explained in §2.2, the HD is mounted inside a ball bearing coupled to a small electric motor by a gear belt and spins at a rate of $\sim$10 Hz. The rotation axis (center) of the HD is offset

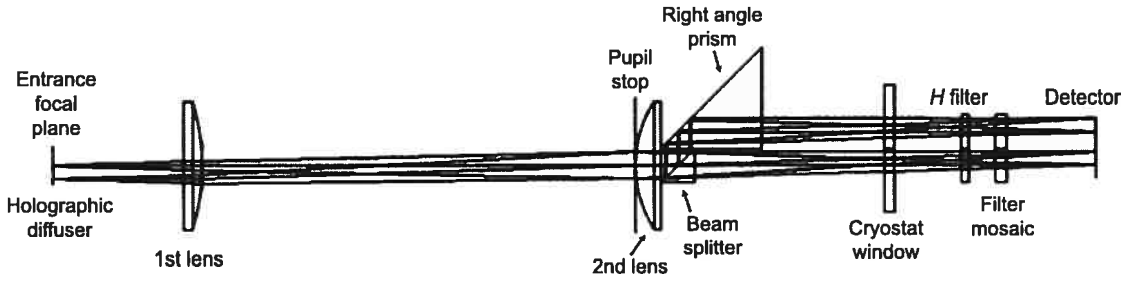

Figure 2.3 Optical layout of the dual imager testbed. Rays are drawn from two field positions at the entrance focal plane. A separate optical system (not shown) is placed in front of the dual imager to produce a PSF on the surface of the HD. See text for more detail.

by ~6 mm from the optical axis to maximize the effective area of the HD seen by the dual imager. The rotation rate was chosen to ensure that at least a few complete rotations would occur during a single exposure.

A diagram of the two-channel camera is shown in Figure 2.3. The camera consists primarily of two plano-convex lenses (CVI Laser, PLCX-38.1-64.4-C and JML Optical Industries, PPX12925/000); an 8 mm pupil stop is located immediately before the second lens. This camera has an entrance focal ratio of $(f/\#)_{\mathrm{MCC}} = 16$; this is roughly the smallest focal ratio that could be realized easily using simple commercially available lenses. A magnification of unity was chosen for simplicity. Beam splitting is made directly after the second lens with a 50/50 beamsplitter cube (Thorlabs, BS012). The beam reflected at 90 degrees is folded back toward the detector by mean of a right angle prism (Bernhard Halle, UPB0.30); the side dimension of this prism was selected such that the extra path length in glass compensates precisely the increased physical path length of this channel, allowing both channels to reach focus in the same plane. The detector used is a Hawaii-1 (Rockwell Scientific Company), it is housed inside an IRLab cryostat. A square filter mosaic consisting of two abutted rectangular filters of bandwidth 3%, centered on 1.575 μm and 1.625 μm respectively, is located in front of the detector and allows imaging through different bandpasses in the two channels. An additional

H-band filter is placed inside the cryostat to block radiation longward of 1.8 μm as the narrow band filters are not blocked outside of the H band. This dual imager has a square field of view 4 mm on a side and a Strehl ratio $> 95\%$ over the entire field of view in each channel, as estimated from Zemax. The FWHM of the PSF at the detector is 5.5 pixels. There is no anti-reflection coating on any of the optical components; hence, many ghosts are present.

2.3.2 Data acquisition and reduction

The speckle noise attenuation capability of the testbed MCC was first quantified without the HD. These measurements were made by acquiring a sequence of images in the same bandpass for both channels by rotating the filter mosaic by 90°, which made both channels fall on the same side of the mosaic. This eliminates chromatic effects and ensures that any decorrelation between the PSFs of the two channels is induced by differential aberrations. Then we obtained a sequence of images in the same configuration but with the HD in place. This sequence was obtained only a few hours after the first one, the only difference being the presence of the HD. It thus provides a direct measurement of the improvement in speckle noise attenuation provided by the HD. Finally, a third sequence was acquired with the HD using different bandpasses for the two channels, which is more representative of astronomical observations. Two diffusers (1° and 5° FWHM) from Physical Optics Corporation were tried and no significant difference in speckle attenuation was found between them; however, the 1° diffuser barely fills up the MCC pupil stop and yields a transmission of 85% while the 5° one largely overfills the MCC pupil stop and yields a transmission of 30%.

All sequences of images were acquired in a similar fashion. Five images with the illumination source ON and OFF were alternately obtained for a total of 40-50 PSF images and darks. Each image consisted of $\sim$5 minutes of coadditions. The intensity of the illumination source was adjusted to saturate the PSF center out to $\sim$3-4 λ/D to improve the signal-to-noise ratio of the speckles at large separations.

Basic image reduction consisted in dark subtraction and division by the flat field. Bad pixels were replaced by the median value of neighboring pixels. For each sequence of images, the center of the first image was found by cross-correlation with a theoretical PSF having the same FWHM in an annulus where the image is not saturated. Then the other images of the sequence (including images of the second channel) were registered to the first one by cross-correlation in the same annulus. The image areas affected by ghost artifacts were masked out for cross-correlation and noise calculation purposes. When images were acquired in two bandpasses simultaneously, the short channel images were spatially scaled up to compensate for the change in diffraction scale with wavelength; the scaling factor was found by cross-correlation. In performing the subtraction, the second channel PSF intensity was normalized by the ratio of the radial profiles of the two channels. For each sequence, all images and all differences were finally median combined.

2.3.3 Attenuation results

A comparison of the images before and after subtraction is shown in Figure 2.4 and the corresponding attenuation curves are shown in Figure 2.5. The single bandpass attenuation without HD is $\sim$3.5 on average; this is slightly better than, but of the order of what is achieved with TRIDENT and SDI. The addition of the HD boosts the attenuation to $\sim$25, and even $\sim$40 on Airy rings, an improvement by a factor $\sim$7-10 over the configuration without the HD. This is a clear demonstration that the effect of differential aberrations is indeed reduced by using an HD. Even though the residual noise in this case is dominated by pixel-to-pixel noise, some residual speckles are present. The attenuation achieved with our testbed may be limited by a combination of interpolation errors (when shifting the images), flat-field errors, differential pixel cross-talk, differential persistence, slight optical distortion of the MCC, or differential aberrations. Misalignment of the cube and prism may also result in slight field rotation and focus differences between the two channels.

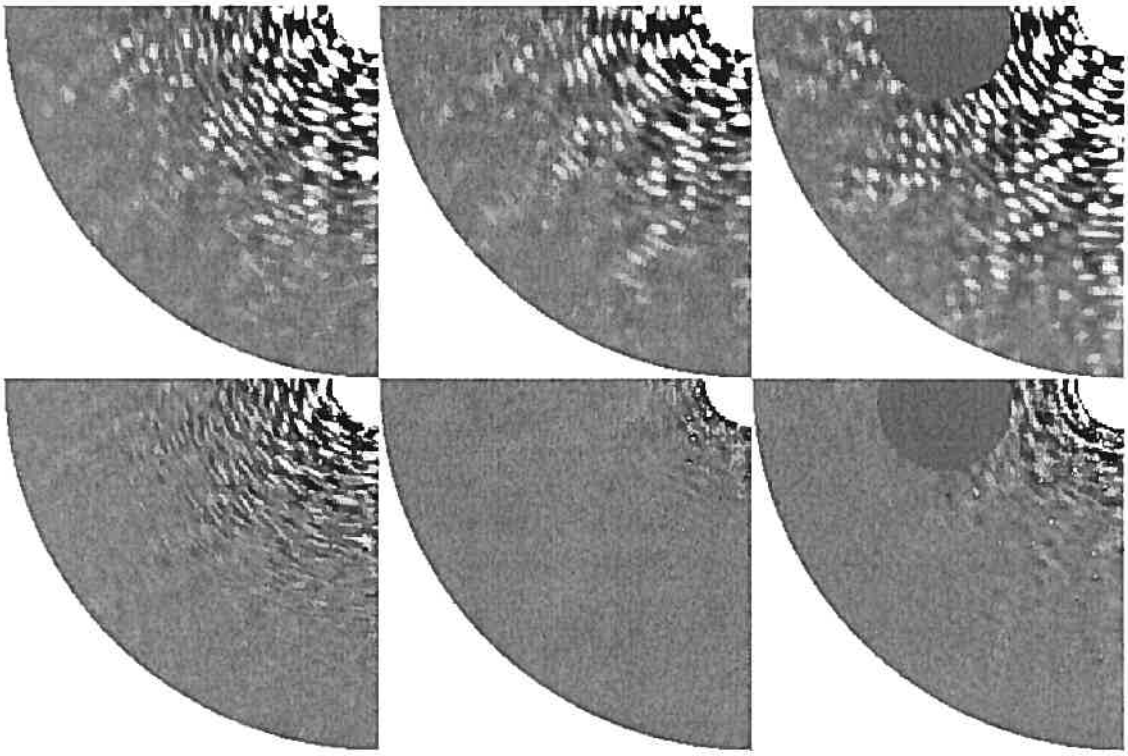

Figure 2.4 Comparison of the image of the first channel after subtraction of a radial profile (*top row*) with the difference of the two channels (*bottom row*). The configurations are: single bandpass without HD (*left*), single bandpass with HD (*middle*), and two-bandpass with HD (*right*). Display intensity range is $\pm 2 \times 10^{-5}$ of PSF peak for all images. The center of the images (white) is saturated. Regions affected by the presence of a ghost are masked out.

Using the HD and two bandpasses, the speckle noise attenuation achieved is ~12-14. For the two wavelengths of our filter mosaic, the maximum attenuation possible for identically shaped bandpasses is $\lambda/\Delta\lambda \sim 30$. However, the transmission profiles of our filters have slopes in opposite directions; this decorrelates the two PSFs further. When taking this into consideration, the maximum attenuation attainable with our mosaic is ~25. Our results show an attenuation lower than this. One possible explanation for the difference, in addition to the ones mentioned previously, is an inadequate calibration of the structures produced by the irregular surface of the HD. During our measurements, we noticed a slow drift of the detector with respect to the pinhole as a function of time.

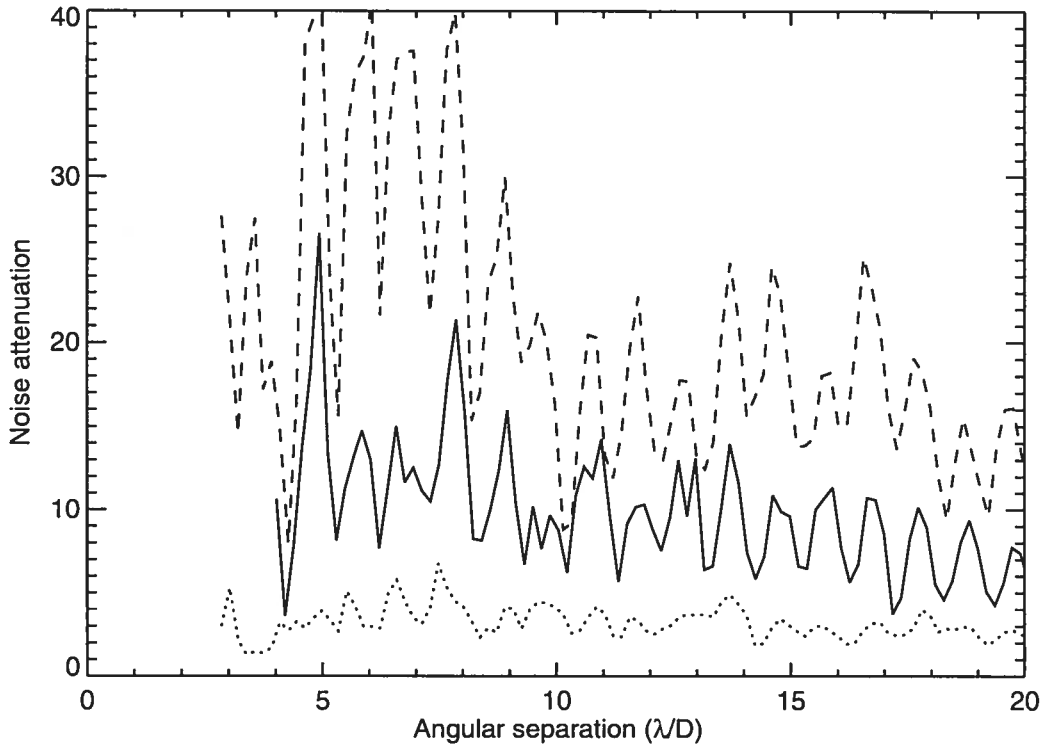

Figure 2.5 Speckle noise attenuation: single bandpass without HD (*dotted line*), single bandpass with HD (*dashed line*), and two-bandpass with HD (*solid line*).

This drift is likely correlated with the level of liquid nitrogen in the cryostat. Hence, the flat field could not be acquired in exactly the same configuration as the PSF images and slight calibration errors may be present. Such residuals, in the form of arcs due to the rotation of the HD, are noticeable in the residual image. The calibration of the surface of the HD is important only when different bandpasses are used because the images have to be rescaled, i.e. a given structure produced by an irregularity on the HD surface will not spatially coincide with itself after rescaling. For this reason, the performance of the two-bandpass configuration can be regarded as a lower limit; a larger attenuation could be achieved using a more stable setup.

2.4 Projected on-sky performance

2.4.1 Detection limit

Numerical simulations were done to estimate the detection limits that currently could be achieved by a dual channel camera under three possible scenarios: (1) without an HD; (2) with an HD added to an existing MCC – requiring the addition of a focal enlarger (§2.2) that reduces the field of view; and (3) with an MCC designed with an HD ab initio – avoiding the focal enlarger and the reduction of the field of view. For case (2), a 4× magnification was assumed, yielding $(f/\#)_{\mathrm{MCC}}/(f/\#)_{\mathrm{inc}} = 4$ as in the laboratory experiment. The baseline camera was assumed to be similar to NICI, i.e. featuring a 1024×1024 pixels detector with a pixel scale of 0.″018 and installed on an 8-m telescope equipped with an 85-actuator AO system. The simulation was done for a wavelength of 1.587 μm, the central wavelength of the first differential imaging filter of NICI. Coronagraphy was not considered as it does not provide significant gain in contrast for Strehl ratios typically achieved today, i.e. <50% (Sivaramakrishnan et al., 2001).

A pupil of diameter 456 pixels placed at the center of a 2048×2048 pixels array was used to produce a PSF with a FWHM equal to 4.5 pixels; the corresponding pixel scale is 0.″009 at the wavelength of the simulation. Atmospheric phase screens were generated for $r_0 = 20$ cm at 0.5 μm. Additionally, a static wavefront phase error having 80 nm rms and a power-law power spectrum of index -2.7 was used. AO phase filtering was simulated by multiplying the amplitude of the phase Fourier transform by a high-pass filter equal to $(k/k_{\mathrm{AO}})^n$ for $k < k_{\mathrm{AO}}$ and to 1 for $k \geq k_{\mathrm{AO}}$, where k is the spatial frequency of the phase aberration and k_{AO} is the AO cutoff frequency (Sivaramakrishnan et al., 2001). The filter index n was set to 1.55 to produce an average Strehl ratio of 0.3, the baseline value expected for NICI[1]. A long exposure monochromatic PSF was obtained by coadding the result of 5000 independent atmospheric wavefront realiza-

[1] see the NICI Campaign Science documentation at http://www.gemini.edu/sciops/instruments/nici/niciCampaign_orig.html.

tions. A polychromatic PSF image was then obtained by coadding 101 spatially scaled versions of the monochromatic image, each representing a different wavelength within the 1% bandwidth of the filter. This PSF image was then either spatially scaled up by a factor of 2, or its pixels binned 2×2 to obtain proper sampling for the configuration with the $4\times$ magnification module ($0\farcs0045$/pixel), or without this module ($0\farcs018$/pixel), respectively. The speckle noise profiles were computed from these images.

The residual speckle noise was then obtained by assuming attenuation factors of 2.5 and 14 for the configuration without and with HD respectively. The pixel-to-pixel noise was computed for a star of given H-band magnitude assuming a total system efficiency of 24%[2] and 19% per channel without and with the HD respectively, a sky background of 14 mag/arcsec^2 in H, a dark current of 0.15 e^-/s per pixel, 30 exposures of 120 s and a read noise of 10 e^-/pixel per exposure. Since the statistical distribution of static speckles is non Gaussian, a 5σ detection limit is not appropriate; rather, to reach a confidence level similar to that of a 5σ Gaussian confidence interval, the detection limits were obtained as the quadratic sum of $10\sigma_{\rm speckle}$ and $5\sigma_{\rm pixel}$ (C. Marois et al., in preparation), where $\sigma_{\rm speckle}$ is the speckle noise (dominating at small separations) and $\sigma_{\rm pixel}$ is the pixel-to-pixel noise (dominating at large separations). A correction was applied to these limits to account for the partial loss in planet flux from the two-channel subtraction[3]; this loss is maximal at zero separation and decreases to zero at a separation where the spatial scaling of the images displaces sufficiently (by $\sim$1 λ/D) the planet. The results for an $H = 6$ star are shown in Figure 2.6. The higher asymptotic limit for the HD with $4\times$ magnification is due to the higher relative importance of read noise for this largely oversampled configuration. The slightly higher asymptotic limit of the HD without magnification compared to the configuration without HD is explained by the

[2]This is the estimated total system efficiency of NICI,
see http://www.gemini.edu/sciops/instruments/nici/niciCampaign_orig.html.

[3]A maximum loss of 12% was assumed; this is the expected flux loss for a T8 dwarf ($T_{\rm eff} \sim 800$ K) using the narrow band filters of NICI. According to the models of Baraffe et al. (2003), giant planets of 5 $M_{\rm Jup}$ or less and older than a few 10 Myr should have $T_{\rm eff} < 800$ K and thus methane absorption redward of 1.6 μm is expected to be at least as important for such objects as for T8 dwarfs.

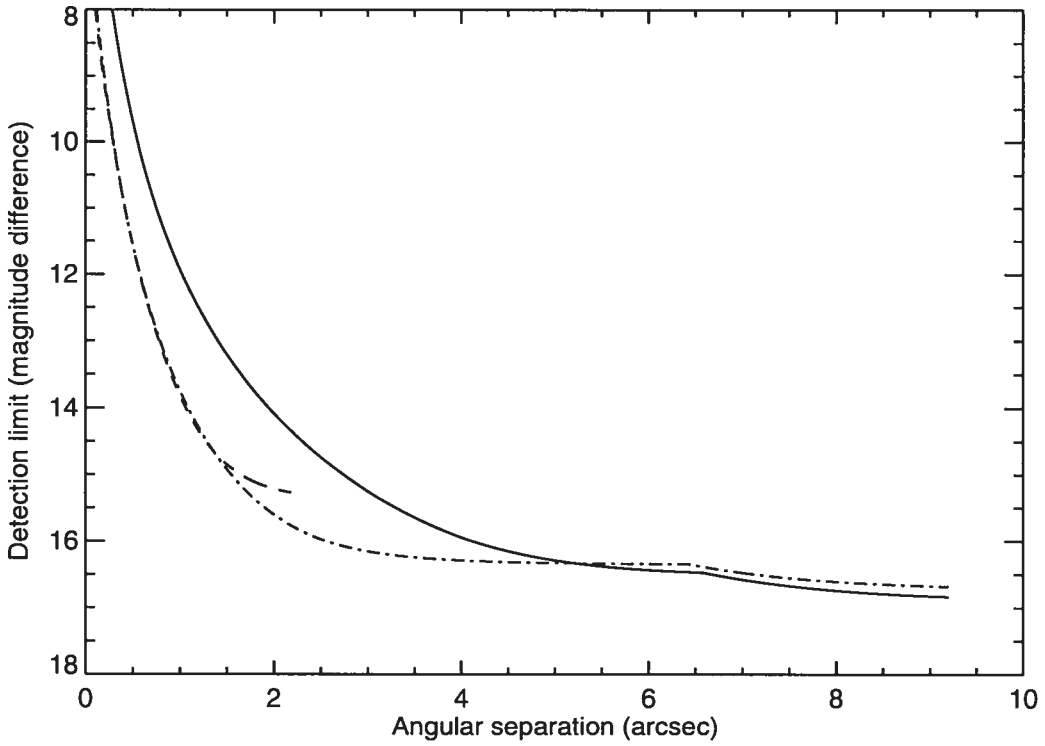

Figure 2.6 Detection limit in difference of magnitude for an $H = 6$ star and exposure time of 3600 s without HD (*solid line*), with HD and 4× focal enlarger (*dashed line*), and with HD and no focal enlarger (*dot-dashed line*). The curve for the configuration with the focal enlarger is shorter due to the reduced field of view.

20% loss in throughput caused by the HD.

The detection limits presented in Figure 2.6 should not be regarded as predictions of the best contrast that a dual-channel camera could reach in practice since other speckle suppression strategies, such as angular differential imaging or subtraction of images obtained after rotation of the instrument, could be used to attenuate the noise further. We note however that the detection limit without HD presented in this figure is very similar to the estimated baseline performance of NICI[4].

[4]see the NICI Campaign Science documentation at http://www.gemini.edu/sciops/instruments/nici/niciCampaign_orig.html. When comparing both curves, one should keep in mind that the detection limits of Figure 2.6 assume a $10\sigma_{\text{speckle}}$ criterion whereas the curve in the NICI documentation is for $5\sigma_{\text{speckle}}$, this translates into a difference of 0.75 mag.

2.4.2 Detection efficiency

A Monte Carlo simulation was done to investigate the impact of using an HD in terms of actual planet detections. First, realistic target samples were constructed for three representative populations of interest for planet searches. In particular, the distance, the age, and the H-band magnitude of each star of the samples were determined. The three samples are:

1. NYS – Nearby young stars ($\lesssim 150$ Myr, < 50 pc). This sample includes 72 stars at a distance less than 50 pc from the Sun, obtained from Tables 3 and 4 of Wichmann et al. (2003); these stars have ages similar to those of the Pleiades stars (20 – 150 Myr) based on lithium abundance measurements. The stellar distances were taken from the same reference. Since the precise age of most of these stars is not well known, the stars were randomly assigned an age from a Gaussian distribution of mean 2.0 and standard deviation 0.15 in log(Age/Myr).

2. TWA – TW Hydrae Association ($\sim$8 Myr, 30-60 pc). This sample includes 23 stars from Table 1 in Zuckerman & Song (2004). The stellar distances were taken from the same reference. The stars were randomly assigned an age from a Gaussian distribution of mean 0.9 and standard deviation 0.04 in log(Age/Myr).

3. ρ Oph – ρ Ophiuchus star forming cloud ($\sim$2 Myr, $\sim$135 pc). This sample includes 27 stars with $R < 15$ from Table 4 of Wilking et al. (2005). The ages were taken from the same reference. The stellar distances were uniformly sampled in the 120-150 pc interval (Knude & Hog, 1998).

In all cases the H-band magnitudes were taken from the 2MASS point source catalog (PSC, Cutri et al., 2003). For the simulation purpose, all samples were artificially increased to a total of 50000 targets by re-using the same stars with different values for the random parameter. A population of exoplanets (one planet per star) was then generated

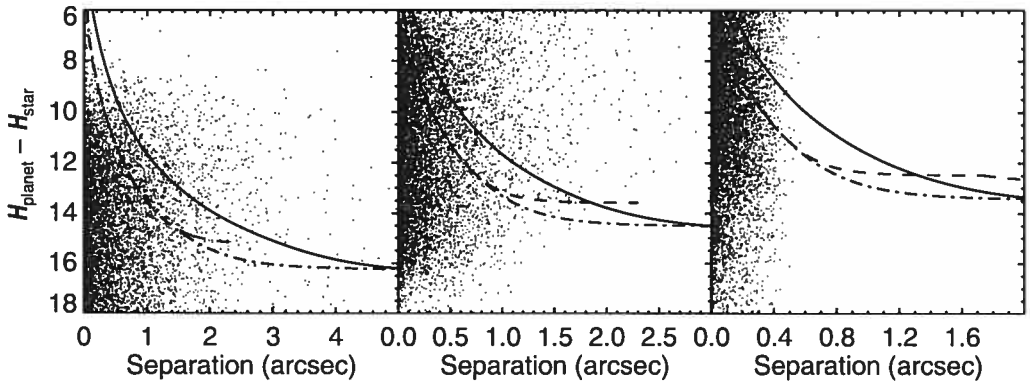

Figure 2.7 Result of the Monte Carlo simulation for the NYS (*left*), TWA (*middle*), and ρ Oph (*right*) samples. The curves show the detection limits for a star having an H magnitude equal to the median of the sample for the configuration without HD (*solid line*), with HD and 4× magnification unit (*dashed line*), and with HD and no magnification unit (*dot-dashed line*). On the left and middle panels, the curve for the configuration with the focal enlarger is shorter due to the reduced field of view.

using a mass distribution following $\mathrm{d}N/\mathrm{d}M \propto M^{-1}$ with $0.5 < M/\mathrm{M_{Jup}} < 12$, a semi-major axis distribution following $\mathrm{d}N/\mathrm{d}a \propto a^{-0.5}$ with $0.1 < a/\mathrm{AU} < 50$, and a Gaussian eccentricity distribution of mean 0.25, standard deviation 0.19 and with $0 \leq e \leq 0.8$; these properties were taken from Marcy et al. (2005) except for $\mathrm{d}N/\mathrm{d}a$ which was set according to a minimum mass solar nebula. All distributions are consistent with the exoplanet population from radial velocity surveys. The orbital inclination and phase were obtained by uniformly sampling respectively the orbital orientation and the orbital area swept by the planet. Using the stellar distances and the orbital parameters, the apparent separation in arcsec was computed for all planets. Models of Baraffe et al. (2003) were used to derive the apparent H-band magnitude of the planets given their mass, age and distance. The magnitude difference between the planets and their primary star was finally compared to the detection limits. The results are shown in Figure 2.7 and the corresponding detection efficiencies are presented in Table 2.2. The detection efficiencies for the configuration without an HD are respectively 6%, 17.5%, and 12.5% for the NYS, TWA, and ρ Oph samples respectively. The use of an HD roughly doubles these

Table 2.2. Planet detection efficiency

Configuration	Target sample		
	NYS	TWA	ρ Oph
No HD	0.063	0.175	0.125
HD w/ 4× mag.	0.113	0.299	0.256
HD w/o mag.	0.128	0.295	0.244

numbers. In all cases it is interesting to note that one would not suffer from the reduction in FOV needed to use an HD with an existing camera, the reason being that most planets are located at small angular separations. Given these relatively small planet detection efficiencies, the relatively small number of stars in real target samples, and the unknown but likely small fraction of stars with giant planets on large orbits, it is reasonable to expect that a dedicated search for planets using actual AO systems on 8-m telescopes will uncover at most a handful of planets. In this case, i.e. for small number statistics, the factor of two in detection efficiency resulting from the use of an HD could make a significant difference.

2.5 Discussion

The experiment presented in this paper validates the concept of breaking the wavefront coherence before separating it into multiple wavelengths for SSDI. It is clearly demonstrated that this strategy reduces the limitations imposed by differential aberrations. Still, the two-bandpass attenuation obtained with our testbed could have been as high as 25 considering the wavelengths of the filter mosaic used. We do not believe that the attenuation achieved was limited by differential aberrations, nor that it represents a fundamental limit to the attenuation achievable with such a system. The fact that the single-bandpass attenuation was higher offers evidence for this claim. We believe that a dedicated MCC built with more care, i.e. with baffles to reduce scattered light, with

coatings on all surfaces to reduce ghost artifacts, with a better alignment of the prism with respect to the beam splitter to minimize differential rotation and distortion between channels, with a more precise control of co-focality between channels, and with better mechanical stability, would provide better noise attenuation. The design of NICI correctly addresses these issues and thus NICI should not suffer from these shortcomings. For completeness, we estimated how the planet detection efficiency would improve with better speckle noise attenuation. It was previously mentioned that the maximum attenuation is $\sim$30 for bandpasses appropriate for exoplanet searches. With such an attenuation, the planet detection efficiency would increase further by $\sim$25%.

The experimental validation of the concept that we presented also offers a good indication that an integral field spectrograph based on a microlens array (e.g. GPI, Macintosh et al., 2006a; SPHERE/IFS, Dohlen et al., 2006; or PFI, Macintosh et al., 2006b) should work well. In such a system, a microlens array is placed at the focal plane to spatially sample the PSF. Each microlens produces a small pupil that is dispersed and re-imaged onto a detector by a spectrograph; a spectrum of each spatial sample of the PSF is thus obtained. Data processing allows the construction of a PSF data cube, containing a spectrum for each spatial pixel. Similarly to the HD, the spatial sampling of the PSF made by the microlens array breaks the coherence of the wavefront and each "micro pupil" becomes an independent source for the spectrograph. In this case, differential aberrations in the spectrograph affect only the light distribution within the spectra and not the speckles of the PSF imaged. Hence, images of the PSF at different wavelengths should be highly correlated. Preliminary laboratory tests of an integral field spectrograph prototype seem to corroborate this hypothesis (Lavigne et al., 2006). Based on a similar argument, the use of a microlens array at the entrance focal plane of an MCC, a concept presented in Lafrenière et al. (2004), should be a good alternative solution.

It was previously mentioned that an existing MCC could be adapted for use with an HD, we take NICI as an example and briefly state the type of work that would be needed

to do so. The NICI system (see Toomey & Ftaclas (2003))[5] consists of a complete AO system followed by a dual-channel camera operating in the 1-5 μm wavelength interval. The focal plane of the camera is located outside of the cryostat. At this focal plane, a wheel mechanism is used to select between various occulting masks for coronagraphy. To implement an HD in this system it would thus be necessary to replace the occulting mask wheel by a mechanism to hold the HD and make it rotate or move continuously as explained in Sect. 2.2. This mechanism would not be technically challenging to realize as it would be warm. The entrance focal ratio of the camera $(f/\#)_{\mathrm{MCC}}$ is 16, thus a diffuser diverging light within a cone of half-angle equal to 1.8° would be needed; a custom HD matched to this angle should be manufacturable as this is in the range of angles available from Physical Optics Corporation. As explained previously, it would be necessary to enlarge the exit focal ratio of the AO system ($f/16$); based on our numerical simulations and experimental results, a factor of 3-4 appears adequate. This magnification would be provided by a system of lenses placed between the dichroic of the AO system and the HD mechanism; these lenses would be warm. Accordingly, the field of view would be reduced by the same factor. These modifications would preclude the use of coronagraphy and would increase the thermal background at longer wavelengths. However, the latter is irrelevant for planet searches as SSDI observations are made in the H-band, and the loss of coronagraphic capabilities would be largely over compensated by the increase in speckle noise suppression given the modest Strehl ratios expected.

2.6 Conclusion

The concept of placing an HD at the entrance focal plane of an MCC to minimize the impact of differential aberrations in SSDI was presented. This concept was shown experimentally to improve significantly the speckle noise attenuation: our dual-beam dual-bandpass experimental testbed produced a speckle noise attenuation of ~12-14, a

[5] see also http://www.gemini.edu/sciops/instruments/nici/niciIndex.html

factor of ~5 improvement over existing SSDI cameras. Using Monte Carlo simulations of realistic exoplanet populations, it was shown that such an improvement in speckle noise attenuation could yield an increase by a factor ~2 of the number of potentially detectable exoplanets. The option presented in this paper should be considered seriously for upcoming multi-channel cameras and instruments dedicated to exoplanet detection.

Acknowledgments

The authors would like to thank René Racine for helpful discussions, and Philippe Vallée, Todd Szarlan, Jean-Sébastien Mayer and Guillaume Provencher for their help in designing and machining parts used for the experimental setup. The authors would also like to thank the anonymous referee for suggestions that improved the quality of the paper. This work was supported in part through grants from the Natural Sciences and Engineering Research Council, Canada, and from the Fonds Québécois de Recherche sur la Nature et les Technologies. This research was performed in part under the auspices of the US Department of Energy by the University of California, Lawrence Livermore National Laboratory under contract W-7405-ENG-48, and also supported in part by the National Science Foundation Science and Technology Center for Adaptive Optics, managed by the University of California at Santa Cruz under cooperative agreement AST 98-76783.

2.A VLT SDI two-channel subtraction attenuation

Since the speckle noise attenuation resulting from a two-channel subtraction of images using SDI is unavailable in the literature, it is estimated here[6]. Observations of the star AB Dor obtained on 2004 February 1 (Close et al., 2005) were retrieved from the European Southern Observatory science archive and used to quantify the performance

[6]Based on observations made with ESO Telescopes at the Paranal Observatories under program ID 60.A-9026.

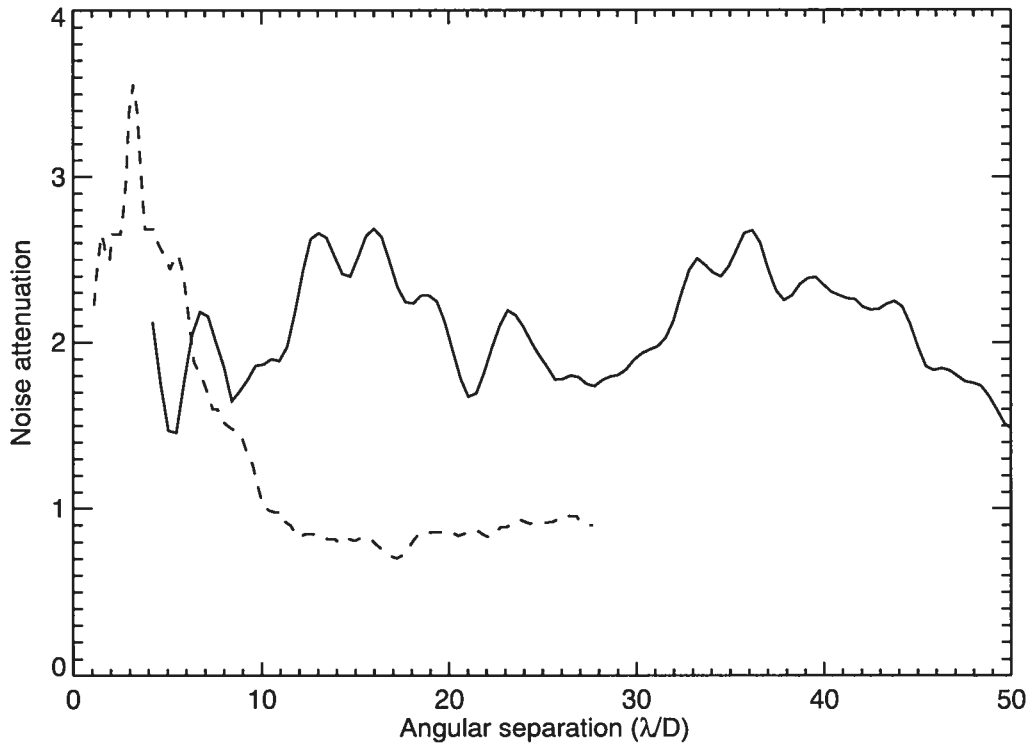

Figure 2.8 Noise attenuation resulting from the subtraction of the two 1.625 μm images with SDI on the VLT (*solid line*). For completeness, the noise attenuation resulting from the subtraction of the 1.58 μm and 1.625 μm images with TRIDENT at the CFHT is shown as a dashed line; these observations were read noise limited beyond 10 λ/D (curve adapted from Marois et al., 2005).

of SDI. This dataset consists in two sets of images at five dither positions obtained at position angles differing by 33 degrees. SDI produces four simultaneous PSF images: one at 1.575 μm, one at 1.600 μm, and two at 1.625 μm. The reduction steps consisted in the subtraction of a sky frame, division by a flat field image and correction of bad pixels using the median of neighboring pixels. The PSF images of all channels were then spatially scaled to match the 1.625 μm channel and registered to a common center with subpixel accuracy. When two PSF images were subtracted, their intensity was adjusted to minimize the residual noise. The six possible two-channel subtractions were performed and a noise attenuation ~2.-2.5 was obtained for all cases. Figure 2.8 shows

the mean attenuation curve over the ten images for the subtraction of the two 1.625 μm channels. We stress that this attenuation is not the best achievable with the SDI device, subtraction of simultaneous multi-channel difference images obtained at different instrument rotation angles have been shown to attenuate further the residuals; see Biller et al. (2004) for more detail.

References

Baraffe, I., Chabrier, G., Barman, T. S., Allard, F., & Hauschildt, P. H. 2003, A&A, 402, 701

Biller, B. A., Close, L., Lenzen, R., Brandner, W., McCarthy, D. W., Nielsen, E., & Hartung, M. 2004, in Proc. SPIE, Vol. 5490, Advancements in Adaptive Optics, ed. D. Bonaccini Calia, B. L. Ellerbroek, & R. Ragazzoni, 389–397

Biller, B. A. et al. 2006, in Proc. SPIE, Vol. 6272, Advances in Adaptive Optics II, ed. B. L. Ellerbroek & D. Bonaccini Calia, 62722D

Close, L. M. et al. 2005, Nature, 433, 286

Cutri, R. M. et al. 2003, 2MASS All Sky Catalog of point sources. (NASA/IPAC Infrared Science Archive. http://irsa.ipac.caltech.edu/applications/Gator/)

Dohlen, K. et al. 2006, in Proc. SPIE, Vol. 6269, Ground-based and Airborne Instrumentation for Astronomy, ed. I. S. McLean & M. Iye, 62690Q

Hodapp, K. W. et al. 2006, in Proc. SPIE, Vol. 6269, Ground-based and Airborne Instrumentation for Astronomy, ed. I. S. McLean & M. Iye, 62693V

Knude, J., & Hog, E. 1998, A&A, 338, 897

Lafrenière, D., Doyon, R., Artigau, É., Marois, C., Beaulieu, M., Nadeau, D., & Racine, R. 2006, in Proc. SPIE, Vol. 6269, Ground-based and Airborne Instrumentation for Astronomy, ed. I. S. McLean & M. Iye, 62692H

Lafrenière, D., Doyon, R., Racine, R., Marois, C., & Nadeau, D. 2004, in Proc. SPIE, Vol. 5492, Ground-based Instrumentation for Astronomy, ed. A. F. M. Moorwood & M. Iye, 500–506

Lafrenière, D., Marois, C., Doyon, R., Artigau, E., & Nadeau, D. 2007, ApJ, 660, 770

Lavigne, J.-F., Doyon, R., Thibault, S., & Lafrenière, D. 2006, in Proc. SPIE, Vol. 6269, Ground-based and Airborne Instrumentation for Astronomy, ed. I. S. McLean & M. Iye, 62693X

Lenzen, R., Close, L., Brandner, W., Biller, B., & Hartung, M. 2004, in Proc. SPIE, Vol. 5492, Ground-based Instrumentation for Astronomy, ed. A. F. M. Moorwood & M. Iye, 970–977

Macintosh, B. et al. 2006a, in Proc. SPIE, Vol. 6272, Advances in Adaptive Optics II, ed. B. L. Ellerbroek & D. Bonaccini Calia, 62720L

Macintosh, B. et al. 2006b, in Proc. SPIE, Vol. 6272, Advances in Adaptive Optics II, ed. B. L. Ellerbroek & D. Bonaccini Calia, 62720N

Marcy, G., Butler, R. P., Fischer, D., Vogt, S., Wright, J. T., Tinney, C. G., & Jones, H. R. A. 2005, Progress of Theoretical Physics Supplement, 158, 24

Marois, C., Doyon, R., Nadeau, D., Racine, R., Riopel, M., Vallée, P., & Lafrenière, D. 2005, PASP, 117, 745

Marois, C., Doyon, R., Racine, R., & Nadeau, D. 2000, PASP, 112, 91

Marois, C., Lafrenière, D., Doyon, R., Macintosh, B., & Nadeau, D. 2006, ApJ, 641, 556

Masciadri, E., Mundt, R., Henning, T., Alvarez, C., & Barrado y Navascués, D. 2005, ApJ, 625, 1004

Racine, R., Walker, G. A. H., Nadeau, D., Doyon, R., & Marois, C. 1999, PASP, 111, 587

Rosenthal, E. D., Gurwell, M. A., & Ho, P. T. P. 1996, Nature, 384, 243

Sivaramakrishnan, A., Koresko, C. D., Makidon, R. B., Berkefeld, T., & Kuchner, M. J. 2001, ApJ, 552, 397

Smith, W. H. 1987, PASP, 99, 1344

Tamura, M. et al. 2006, in Proc. SPIE, Vol. 6269, Ground-based and Airborne Instrumentation for Astronomy, ed. I. S. McLean & M. Iye, 62690V

Toomey, D. W., & Ftaclas, C. 2003, in Proc. SPIE, Vol. 4841, Instrument Design and Performance for Optical/Infrared Ground-based Telescopes, ed. M. Iye & A. F. M. Moorwood, 889–900

Wichmann, R., Schmitt, J. H. M. M., & Hubrig, S. 2003, A&A, 399, 983

Wilking, B. A., Meyer, M. R., Robinson, J. G., & Greene, T. P. 2005, AJ, 130, 1733

Zuckerman, B., & Song, I. 2004, ARA&A, 42, 685

CHAPITRE 3

UN NOUVEL ALGORITHME DE SOUSTRACTION DE LA FONCTION D'ÉTALEMENT DE POINT EN IMAGERIE À HAUTE GAMME DYNAMIQUE : UNE DÉMONSTRATION AVEC L'IMAGERIE DIFFÉRENTIELLE ANGULAIRE

A NEW ALGORITHM FOR POINT SPREAD FUNCTION SUBTRACTION IN HIGH-CONTRAST IMAGING: A DEMONSTRATION WITH ANGULAR DIFFERENTIAL IMAGING

DAVID LAFRENIÈRE[a], CHRISTIAN MAROIS[a,b], RENÉ DOYON[a], DANIEL NADEAU[a], AND ÉTIENNE ARTIGAU[a,c]

Published in: *The Astrophysical Journal*, v.660, p.770 (2007)

Abstract

Direct imaging of exoplanets is limited by bright quasi-static speckles in the point spread function (PSF) of the central star. This limitation can be reduced by subtraction of reference PSF images. We have developed an algorithm to construct an optimized reference PSF image from a set of reference images. This image is built as a linear combination of the reference images available and the coefficients of the combination are optimized inside multiple subsections of the image independently to minimize the residual noise within each subsection. The algorithm developed can be used with many high-contrast imaging observing strategies relying on PSF subtraction, such as angular

[a]Département de physique and Observatoire du Mont Mégantic, Université de Montréal, C.P. 6128, Succ. Centre-Ville, Montréal, QC, Canada H3C 3J7

[b]Institute of Geophysics and Planetary Physics L-413, Lawrence Livermore National Laboratory, 7000 East Ave, Livermore, CA 94550

[c]Gemini Observatory, Southern Operations Center, Association of Universities for Research in Astronomy, Inc., Casilla 603, La Serena, Chile

differential imaging (ADI), roll subtraction, spectral differential imaging, reference star observations, etc. The performance of the algorithm is demonstrated for ADI data. It is shown that for this type of data the new algorithm provides a gain in sensitivity by up to a factor 3 at small separation over the algorithm used in Marois et al. (2006).
Subject headings: Instrumentation: adaptive optics — planetary systems — stars: imaging — techniques: image processing — techniques: high angular resolution

3.1 Introduction

Direct imaging of exoplanets, circumstellar disks, jets, winds or other structures around stars is difficult due to the angular proximity of the star and the very large luminosity ratios involved. Current attempts, both from the ground with adaptive optics (AO) and from space, are limited by a swarm of bright quasi-static speckles that completely mask out the faint planets or structures that are sought after (Schneider & Silverstone, 2003; Biller et al., 2004; Marois et al., 2005; Masciadri et al., 2005). These speckles are caused mainly by imperfections in the optics and are long-lived, hence the "quasi-static" appellation. As the exposure time is increased, the quasi-static speckles add coherently and their intensity eventually becomes dominant over signals that add incoherently, such as sky or read noise and general (non-static) speckles.

This problem is more important closer to the star, as the relative speckle intensity is higher there, and the size of the region in which the noise is dominated by quasi-static speckles will depend upon the exposure time, the sky and read noise levels, the telescope and camera used, the target brightness, etc. For example, the observations of Masciadri et al. (2005) obtained at the Very Large Telescope are limited by speckles only at subarcsecond separations, while in the search for planets on wide orbits that we are currently carrying at the Gemini telescope (D. Lafrenière et al., in preparation), the observations, which use longer individual exposure times (30 s), are typically limited by quasi-static speckle noise out to separations of $\sim 5''$-$10''$. Quasi-static speckles even

dominate the noise at separations well past 10″ in the observations of the bright star Vega obtained by Marois et al. (2006) at the Gemini telescope; this also appears to be the case for similar observations obtained on the Keck and Palomar 5-m telescopes (Macintosh et al., 2003; Metchev et al., 2003). At a given angular separation, no gain in contrast is achieved by increasing the exposure time once the noise is dominated by quasi-static speckles.

When this regime is reached, it is possible to subtract the quasi-static speckles by using reference point spread function (PSF) images. A reference PSF image is any image whose subtraction from the target image would reduce the signal from the speckles while preserving that of the object sought after. For example, reference PSF images can be obtained from observations of reference stars, or from observations of the target itself obtained at different field of view orientations (e.g. Schneider & Silverstone, 2003), wavelengths (e.g. Racine et al., 1999), or polarizations (e.g. Kuhn et al., 2001).

Obtaining a reference PSF image highly correlated with the target image is a difficult task because even though quasi-static speckles are long lived, they still vary with time due to temperature or pressure changes, mechanical flexures, guiding errors or other phenomena (Marois et al., 2005, 2006). On the other hand, even when a reference PSF image is acquired simultaneously with the target image at other wavelengths or polarizations, differential aberrations within the camera decorrelate the PSFs (Marois et al., 2005; Lenzen et al., 2004). Thus, when trying to subtract speckles one must always work with slightly decorrelated reference PSF images and the specific way in which the available data are used to perform the subtraction may have a significant impact on the speckle noise attenuation achieved. This paper presents a way of combining reference PSF images to optimize the noise attenuation. In particular the algorithm is applied to angular differential imaging (ADI) (Marois et al., 2006), which is currently one of the most efficient quasi-static speckle suppression technique for ground-based observations. Although emphasis is given to point source detection throughout the paper, the algorithm can be optimized to search for any other structure in the close vicinity of a star.

The new reference PSF construction algorithm is presented in §3.2. Then, a review of ADI and the algorithm used by Marois et al. (2006) is presented in §3.3. In §3.4, the new algorithm is applied to ADI and its performance is presented. The possibility of using this algorithm with other observing strategies is finally discussed in §3.5.

3.2 Reference PSF construction by locally optimized combination of images

Consider a single target image, from which speckles are to be subtracted, and suppose that N reference PSF images are available for this purpose. The heart of the algorithm described here is to divide the target image into subsections and to obtain, for each subsection independently, a linear combination of the reference images whose subtraction from the target image will minimize the noise. By optimizing the weights given to the N available reference PSF images according to the residual noise obtained, this approach produces a representation of the target PSF image that is better than any predefined combination of the reference PSF images. Further, it is advantageous to optimize the coefficients of the linear combination for subsections of the image because the correlation between the target and the reference PSF images generally varies with position within the target image. We refer to the algorithm described here as "locally optimized combination of images", or LOCI.

The coefficients used for subtraction of the speckles within subsection S^T of the target image are determined by a minimization of the noise within a generally larger, so-called optimization, subsection O^T, which encompasses S^T. The corresponding optimization subsections in the reference PSF images are denoted O^n, $n = 1, \ldots, N$.

Ideally, to achieve the optimal noise attenuation everywhere in the target image, one would want to optimize the coefficients for subsections S^T that are as small as possible, ultimately consisting of a single pixel. In practice, to avoid a computationally prohibitive repetition of the algorithm, one uses subsections that contain many pixels, within which the same linear combination of reference images is used.

While the size of the subsection S^T is limited by computation resources, the size of O^T is determined by the need to preserve the signal from any point source sought after. From the point of view of the algorithm described below, a point source in O^T is a residual that it tries to minimize and will partially subtract. The amount of partial subtraction depends upon the fractional area of O^T that is occupied by the point source. So, even though smaller optimization subsections lead to a better noise attenuation, they also lead to a larger subtraction of the signal of the point sources sought after. Thus the size of O^T must be properly determined and the amount of partial subtraction of point sources must be well characterized. The area A of the optimization subsection is determined by the parameter N_A through the expression

$$A = N_A \pi \left(\frac{W}{2}\right)^2 \tag{3.1}$$

where W is the full-width-at-half-maximum (FWHM) of the PSF; N_A thus corresponds to the number of "PSF cores" that fit in the optimization subsection.

If the set of reference PSF images contains target images, it is necessary to construct the optimized PSF to be subtracted from a given subsection S^T by using only the subset of these images in which a companion point source appearing in S^T would be displaced by at least a distance $\delta_{\min}$ or would have an intensity smaller by at least a factor α with respect to its position or intensity in the image from which speckles are to be subtracted. In other words, this subset includes all reference PSF images of index $k \in K$, where

$$K = \{k \in [1,N] : |\mathbf{r}_k - \mathbf{r}_T| > \delta_{\min} \vee f_k/f_T < \alpha\}, \tag{3.2}$$

$\mathbf{r}_T$ being any field position in the subtraction subsection of the target image and $\mathbf{r}_k$ the corresponding position in image k, while f_k/f_T is the intensity ratio in those images of any companion sought after. If the set of reference PSF images does not contain target images, then $K = \{1,\ldots,N\}$. The parameters $\delta_{\min}$ and α, when applicable, affect both the speckle noise attenuation and the amount of partial subtraction of point sources,

similarly to N_A. The best values to use, which depend on the type of data being analyzed and the level of correlation between the target and reference images, may be determined from a comparison of the results obtained with different values, see §3.4.1. For the remainder of the section, it is assumed that values for N_A, $\delta_{\min}$, and α have been selected by the user.

The reference PSF for the optimization subsection is then constructed according to

$$O^R = \sum_{k \in K} c^k O^k, \tag{3.3}$$

where the coefficients c^k are to be determined by the algorithm. They are computed by minimizing the sum of the squared residuals of the subtraction of O^R from O^T, which is given by

$$\sigma^2 = \sum_i m_i \left(O_i^T - O_i^R\right)^2 = \sum_i m_i \left(O_i^T - \sum_k c^k O_i^k\right)^2, \tag{3.4}$$

where i denotes a pixel in the optimization subsection and m is a binary mask that may be used to ignore some pixels. The quantity to minimize is a sum and can be biased by cosmic ray hits or bad pixels if they have not been properly corrected or filtered before the algorithm is used. When bad pixels remain in the image, the bias can be completely remedied by setting the mask m to zero for these pixels. Generally, the fraction of pixels affected is small and their exclusion from the computation of the residuals has practically no impact on the solution found. The minimum of σ^2 occurs when all its partial derivatives with respect to the coefficients c^k are equal to zero, i.e. when

$$\frac{\partial \sigma^2}{\partial c^j} = \sum_i -2 m_i O_i^j \left(O_i^T - \sum_k c^k O_i^k\right) = 0, \quad \forall\, j \in K. \tag{3.5}$$

Reversing the summation order and rearranging the terms we find

$$\sum_k c^k \left(\sum_i m_i O_i^j O_i^k\right) = \sum_i m_i O_i^j O_i^T, \quad \forall\, j \in K. \tag{3.6}$$

This is a simple system of linear equations of the form $\mathbf{Ax} = \mathbf{b}$ where

$$A_{jk} = \sum_i m_i O_i^j O_i^k, \qquad x_k = c^k, \qquad b_j = \sum_i m_i O_i^j O_i^T. \tag{3.7}$$

Solving this system gives the coefficients c^k needed to construct the optimized reference PSF image for the subsection S^T. By construction, assuming that all the O^k are linearly independent, the matrix $\mathbf{A}$ is always invertible. Thus, the system always has a unique solution, meaning that for the given optimization subsection and set K the solution found leads to an *absolute* minimum of the residuals. Finally, using the set of optimized coefficients, the optimized reference PSF image subsection to be subtracted from S^T is constructed as

$$S^R = \sum_{k \in K} c^k S^k, \tag{3.8}$$

where S^k denotes the corresponding subtraction subsection in the reference PSF image k.

3.3 Review of angular differential imaging

The ADI technique, as detailed in Marois et al. (2006), consists in acquiring a sequence of many exposures of the target using an altitude/azimuth telescope with the instrument rotator turned off (at the Cassegrain focus) or adjusted (at the Nasmyth focus) to keep the instrument and telescope optics aligned. This is a very stable configuration and ensures a high correlation of the sequence of PSF images. This setup also causes a rotation of the field of view (FOV) during the sequence. For each target image in such a sequence, it is possible to build a reference image from other target images in which any companion would be sufficiently displaced due to FOV rotation. After subtraction of the reference image, the residual images are rotated to align their FOV and co-added. Because of the rotation, the PSF residual speckle noise is averaged incoherently, ensuring

an ever improving detection limit with increasing exposure time.

In building a reference image, a compromise has to be reached between the quasi-static speckle noise correlation, which is highest for the shortest time delays between images, as shown in Figure 2 of Marois et al. (2006), and the need to ensure a sufficient companion displacement. The minimum time delay τ_{min} between an image and the ones which can be used as references decreases as the inverse of the angular separation. Accordingly, it is possible to use images more closely separated in time to build the reference image at larger angular separations.

In the speckle subtraction algorithm used in Marois et al. (2006) (see their §5.2 and their Table 2), the first step is to subtract the median of all the images from each individual image. Each target image is then broken into many annuli to reflect the dependence of τ_{min} on the distance from the center of the PSF. A reference image is obtained within each annulus by median combining the four images obtained closest in time but at least τ_{min} from the target image. The intensity of this reference image is also scaled to minimize the noise after reference subtraction. All the resulting images are then rotated to align their FOV and a median is taken over them.

3.4 Application of the LOCI algorithm to angular differential imaging data

3.4.1 Definition of the arbitrary parameters specific to ADI

As mentioned in §3.2, some parameters must be chosen by the user before the algorithm is used. For ADI data, as images are generally acquired in a single bandpass, the parameter α does not apply. On the other hand, the area and shape of the subtraction and optimization subsections must be defined as well as the minimum displacement δ_{min} between sources in the target and reference images.

The dependence of τ_{min} on angular separation suggests the use of annular geometry for the subtraction subsections. These subsections are obtained by further dividing the annuli azimuthally to reduce their spatial extent, which enables a better fit of local PSF

variations as explained above. Since $\tau_{\min}$ is proportional to $1/r$, the set of images that can be used to construct a reference PSF changes rapidly with radius at small separation and it is best to use narrow subsections at small radii to ensure that the largest possible set of reference PSF images is used at any separation. The subtraction subsections S^T are described by their inner radius r, mean angular position ϕ, radial width dr, and angular width $\Delta\phi$.

The optimization subsections O^T share the same inner radius, mean angular position, and angular width as their corresponding subtraction subsection. As explained in §3.2, the area A of the optimization subsections has to be chosen to maximize noise attenuation while minimizing point source subtraction. For an annular subsection O^T of inner radius r, radial width Δr, and azimuthal width $(r+\Delta r/2)\Delta\phi$,

$$A = \Delta r(r+\Delta r/2)\Delta\phi. \tag{3.9}$$

We define the ratio of the radial and azimuthal widths of the optimization subsections as

$$g = \frac{\Delta r}{(r+\Delta r/2)\Delta\phi} = \Delta r^2/A. \tag{3.10}$$

Then, by Eq.(3.1), Δr and $\Delta\phi$ are uniquely determined by the parameters g and N_A and the PSF width W:

$$\Delta r = \sqrt{\pi g N_A W^2/4}, \tag{3.11}$$

and

$$\Delta\phi = \left(\frac{g}{2} + \frac{2r}{W}\sqrt{\frac{g}{\pi N_A}}\right)^{-1}. \tag{3.12}$$

The optimization subsections were chosen not to be centered radially on the subtraction subsections but to extend to larger radii because, in the optimization, the radial dependence of the PSF noise gives more weight to the inner pixels, i.e. to the pixels in S^T.

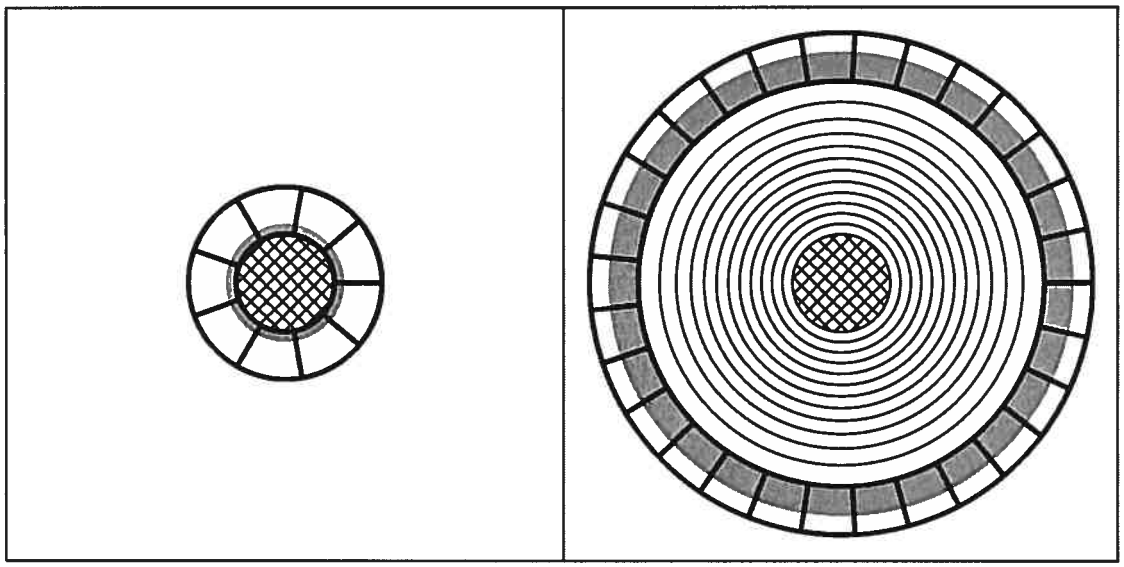

Figure 3.1 Example of subtraction (*shaded in grey*) and optimization (*delimited by thick lines*) subsections for ADI using the procedure of §3.4.1. The left and right panels show the subtraction and optimization subsections for the 1st and 13th subtraction annuli respectively. In the right panel, the first 12 subtraction annuli (of width dr) are marked by thin lines; dr increases with separation in this specific example. The central circle (cross-hatched) represents the saturated region.

Figure 3.1 shows an example of subsections that can be used with this procedure.

For ADI data, the set of target images is the same as the set of reference PSF images. The subset of images that can be used as references for a given subsection S^T of a given target image depends upon the parameter $\delta_{\min}$ introduced in §3.2, whose value is set by the parameter N_δ through the expression

$$\delta_{\min} = N_\delta W + r\,\mathrm{d}\theta_n, \tag{3.13}$$

where $\mathrm{d}\theta_n$ is the angle of FOV rotation that occurred during exposure n. The last term of the expression above represents the azimuthal smearing of an off-axis point source that occurs during an exposure due to FOV rotation. The parameter N_δ represents the minimum gap allowed, in units of the PSF FWHM, between a source position in image n and the corresponding positions in the images used as references.

The values of N_A, g, dr and N_δ that maximize the sensitivity to faint point sources will be determined in the next section using real data.

3.4.2 Parameter determination

Observations of the star HD97334b (G0V, $H = 5$) were used to determine the values of the algorithm parameters. These observations are part of the Gemini Deep Planet Survey (GDPS, D. Lafrenière et al., in preparation), which is an ongoing direct imaging search for Jupiter mass planets on large orbits (> 40 AU) around young nearby stars ($\sim$100 Myr, $<$35 pc). This particular dataset consists in a sequence of 90 30-s images in the CH_4-short (1.58 μm, 6.5%) filter obtained with ALTAIR/NIRI at the Gemini North telescope (program GN-2005A-Q-16). The $f/32$ focal ratio of the camera and 8-m primary mirror diameter lead to $0\farcs022$ pixel^{-1}. The images are saturated inside a radius of $\sim 0\farcs7$ from the PSF center. Short unsaturated exposures were acquired before and after the saturated sequence to calibrate photometry and detection limits. The corrected PSF FWHM was measured to be 3.4 pixels, or $0\farcs074$, and the Strehl ratio was $\sim$16%. The Cassegrain rotator was fixed during all observations. Basic image reduction and registering was done as in Marois et al. (2006).

The same procedure was used for optimizing each of N_δ, N_A, g and dr. First, the unsaturated PSF image was used to introduce artificial point sources to the images at angular separations in the range 50-300 pixels (27-160 λ/D) in steps of 5 pixels (2.75 λ/D). Each artificial source was smeared according to its displacement during an integration, and its intensity was set so that its S/N would be $\sim$10 in the final residual combination. Next, a symmetric radial profile was subtracted from each image to remove the seeing halo. Then the subtraction algorithm was run on the sequence of images with a range of values for the parameter under consideration. Finally, the noise and the flux of each artificial point source in an aperture diameter of one FWHM were measured in the residual image. This process was repeated 50 times by placing the artificial sources at different angular positions each time. The trial values for the optimization of each parameter are

Table 3.1. Parameter values used for optimization

Parameter	Trial values	Adopted value
N_δ	0.25, 0.5, 0.75, 1.0, 1.5, 2.0	0.5
N_A	50, 100, 150, 300, 500	300
g	0.5, 1.0, 2.0	1.0
dr	1.5, 3, 6, 9, 15, (1.5-15)[a]	(1.5-15)[a]

[a]dr equal to 1.5 for separations less than 60 λ/D and 15 for larger separations.

listed in Table 3.1. For dr either a fixed value is used throughout the image or one that varies from 1.5 to 15 in units of the PSF FWHM. The optimal value of a parameter was determined recursively, with the values of the other parameters set first to the medians of the values listed in Table 3.1 and then to their most recently determined optimal value except for dr set at a fixed value of 1.5. The results are shown in Figures 3.2-3.5.

As can be seen in Figure 3.2, the minimum spacing has little impact on the recovered flux at separations $\gtrsim 100\ \lambda/D$, where ~80-90% of the flux is recovered independently of N_δ. However, at small separations the effect is important and significant loss in signal occurs, particularly for the smallest minimum displacements. This is because the fraction of images in the subset K for which the point source partially overlaps that in the target image is greater for smaller separations, where linear motion of the point source is slower. The best overall S/N is obtained with $N_\delta = 0.5$, for which the loss in the recovered flux is more than compensated by the improvement in quasi-static speckle noise attenuation.

Figure 3.3 shows that the residual signal of point sources is strongly dependent upon the size of the optimization subsections, as expected from the discussion in §3.2. When N_A is too small, the gain in attenuation is not sufficient to compensate for the larger point source subtraction and lower S/N ratios are obtained, especially at large separations.

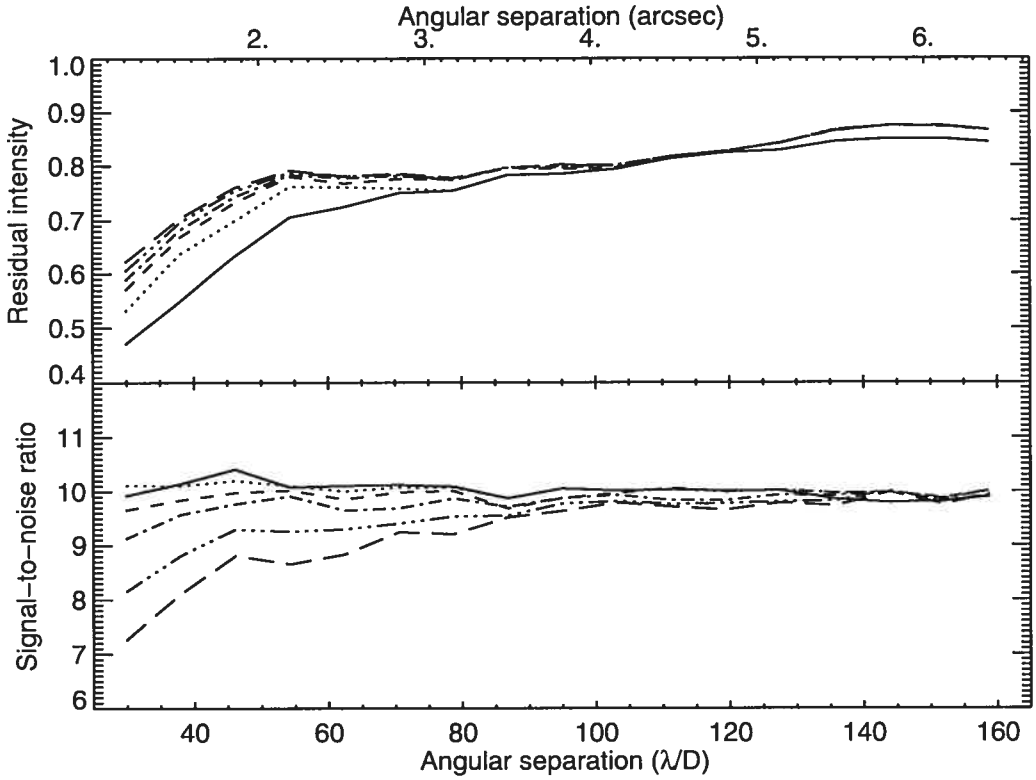

Figure 3.2 Average residual intensity of the artificial point sources normalized to their initial intensity (*top*), and their S/N ratio (*bottom*) as a function of angular separation, for different values of N_δ. The solid, dotted, dashed, dot-dashed, triple-dot-dashed, and long-dashed curves are respectively for $N_\delta = 0.25, 0.5, 0.75, 1.0, 1.5$, and 2.0.

On the other hand, when N_A is too large, the quasi-static speckles are not subtracted as efficiently at small separations and lower S/N ratios result. A value of $N_A = 300$ provides the best overall S/N ratio.

The parameter g has little effect on the performance, see Figure 3.4, although for angular separations $\lesssim 50\ \lambda/D$ regions more extended radially ($g = 2$) fare slightly better than regions more extended azimuthally. Nevertheless, we adopt $g = 1$ as the optimal value.

Finally, Figure 3.5 shows that at small separations ($\lesssim 60\ \lambda/D$), a $dr \gtrsim 6$ leads to a lower S/N ratio because it poorly matches the evolution of $\tau_{\min}$ with separation, as expected. Since a larger dr leads to a faster execution of the algorithm, because fewer

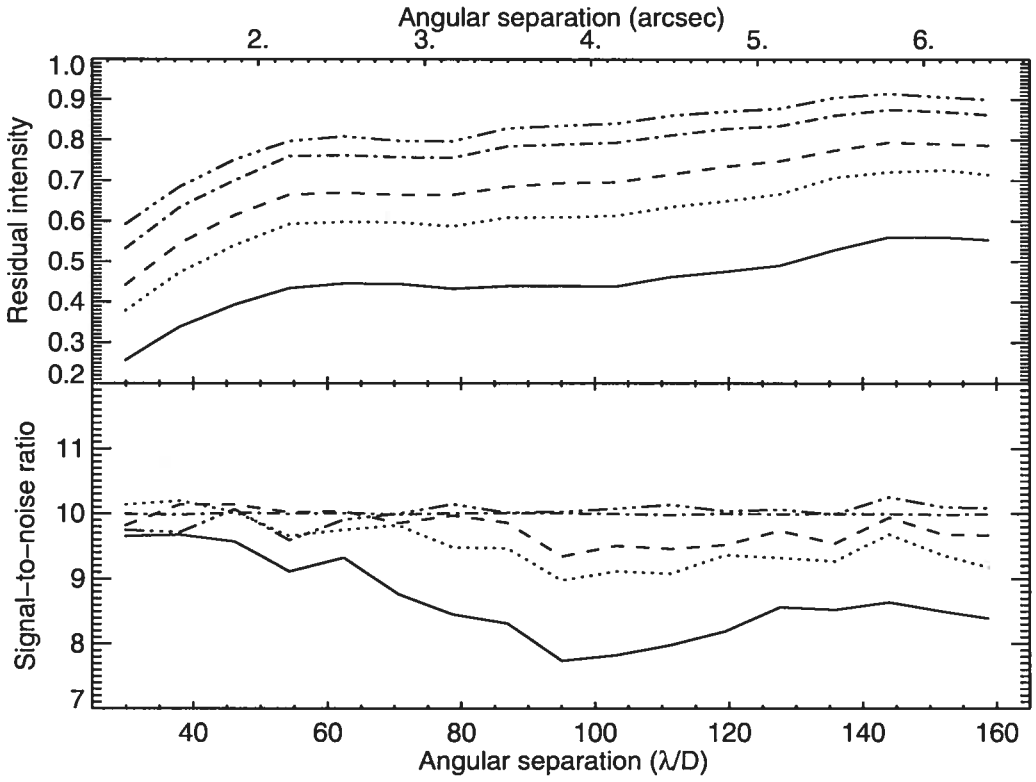

Figure 3.3 Average normalized residual intensity (*top*) and S/N ratio (*bottom*) as a function of angular separation for different values of N_A. The solid, dotted, dashed, dot-dashed, and triple-dot-dashed curves are respectively for $N_A = 50$, 100, 150, 300, and 500.

subtraction subsections are required to cover the entire image, we use as the optimal value a dr equal to 1.5 for separations less than 60 λ/D and 15 for larger separations.

The optimal parameter values may vary slightly from those found above for other sets of data depending on the telescope, instrument, seeing, FOV rotation rate, target brightness, etc. They are optimized here for a specific set of data only to illustrate the potential of the LOCI algorithm for ADI. For all computations that follow, the optimal values listed in Table 3.1 are used.

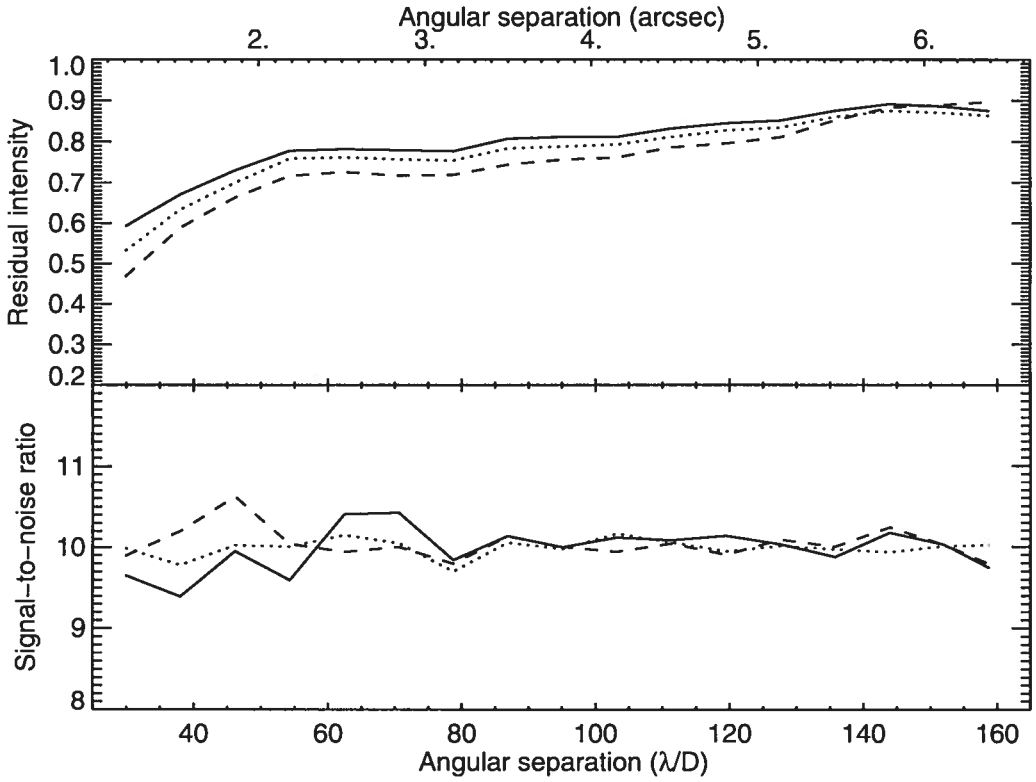

Figure 3.4 Average normalized residual intensity (*top*) and S/N ratio (*bottom*) as a function of angular separation for different values of g. The solid, dotted, and dashed curves are respectively for $g = 0.5$, 1, and 2.

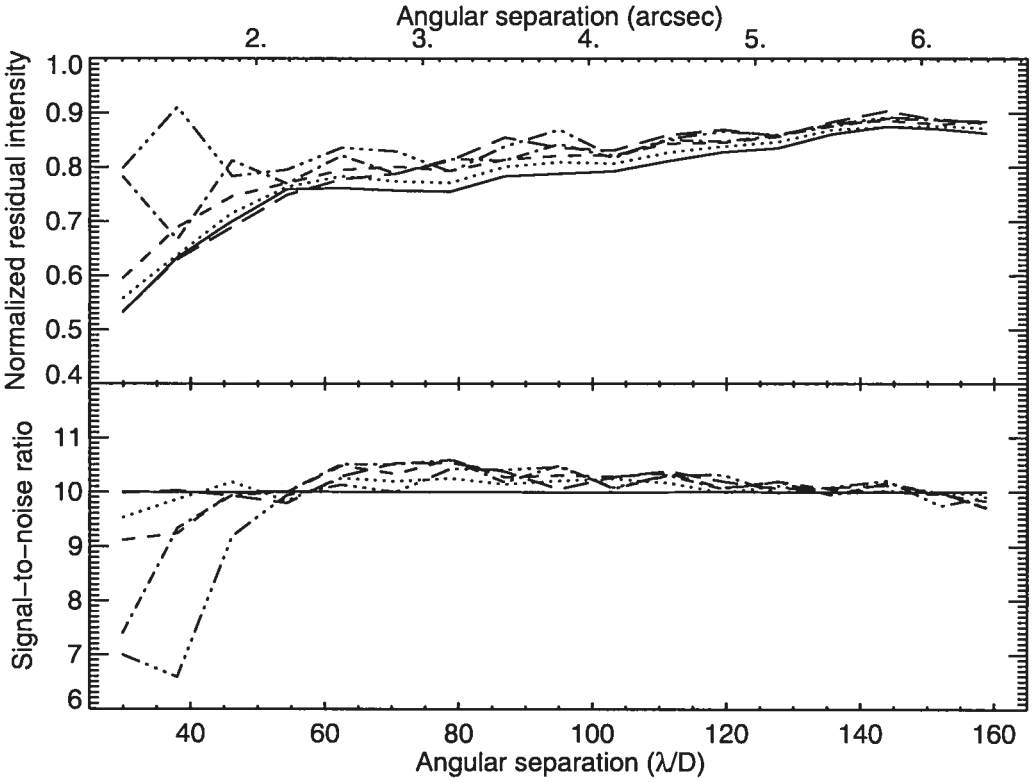

Figure 3.5 Average normalized residual intensity (*top*) and S/N ratio (*bottom*) as a function of angular separation for different values of dr. The solid, dotted, dashed, dot-dashed, triple-dot-dashed, and long-dashed curves are respectively for dr = 1.5, 3, 6, 9, 15, and dr varying with radius (see text).

3.4.3 Point source photometry

Since the algorithm reduces the flux of point sources significantly, especially at small separations, it is important to verify that the true flux can be recovered accurately and that the uncertainty on this value can be well determined. The algorithm was run on the sequence of images, with artificial companions of various intensities added at all angular separations in the range 50-300 pixels (27-160 λ/D) by steps of 5 pixels (2.75 λ/D). Four intensities were used, yielding S/N of 3, 6, 10 and 25 in the final residual image. This process was repeated 50 times with the sources at different azimuthal positions. The mean normalized residual source intensities and residual intensity dispersions over the 50 azimuthal positions were then computed and the results are shown in Figure 3.6.

The top panel of this figure shows that the normalized residual intensities do not vary with the intensity of the sources, i.e. *the fraction of the signal of a source that is subtracted by the algorithm is independent of the source brightness*. Hence, a normalized residual intensity curve obtained by implanting artificial point sources of a given brightness can be used to calculate the true flux of sources of any brightness and to correct the detection limit curve computed from the variance of the residual noise.

The bottom panel of Figure 3.6 shows that the noise measured in the residual image is an adequate measure of the uncertainty on the intensity of sources at 10σ or less. For brighter sources ($\sim 25\sigma$), the uncertainty is slightly larger for small separations. This is probably due to the larger bias introduced by brighter point sources and the more important dependence of the amount of partial subtraction on the specific PSF structure underlying the point source in regions strongly dominated by quasi-static speckle noise. Thus, the noise in the residuals may be used as the uncertainty on the flux for most sources but it may be necessary to carry out an analysis using artificial point sources for brighter sources at small separations.

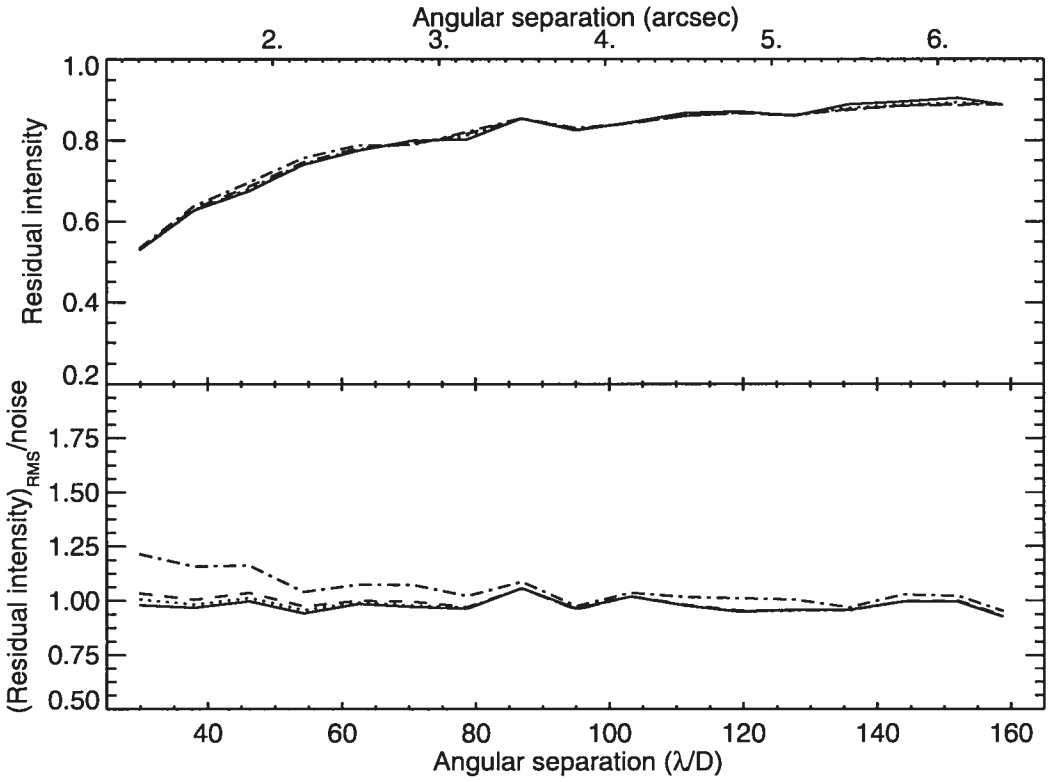

Figure 3.6 Average normalized residual intensity (*top*) and ratio of the measured dispersion of the residual intensity of sources over the residual noise (*bottom*). The solid, dotted, dashed, and dot-dashed lines are respectively for point source intensities yielding S/N of 3, 6, 10, and 25 in the final residual image.

3.4.4 Comparison with previous algorithm

A comparison of the LOCI algorithm with that used by Marois et al. (2006) is presented. Artificial point sources were added to the images at several separations in the range 40-500 pixels (22-275 λ/D) by steps of 5 pixels (2.75 λ/D). The intensities of the artificial sources were adjusted to yield a final S/N$\sim$10 with the LOCI algorithm. Both subtraction algorithms were then run on the images. This was repeated 25 times with the artificial sources at different azimuthal positions. The mean residual intensity and S/N over the 25 azimuthal positions were then computed for each algorithm and separation. The results are shown in Figure 3.7. At all separations, the LOCI algorithm yields a

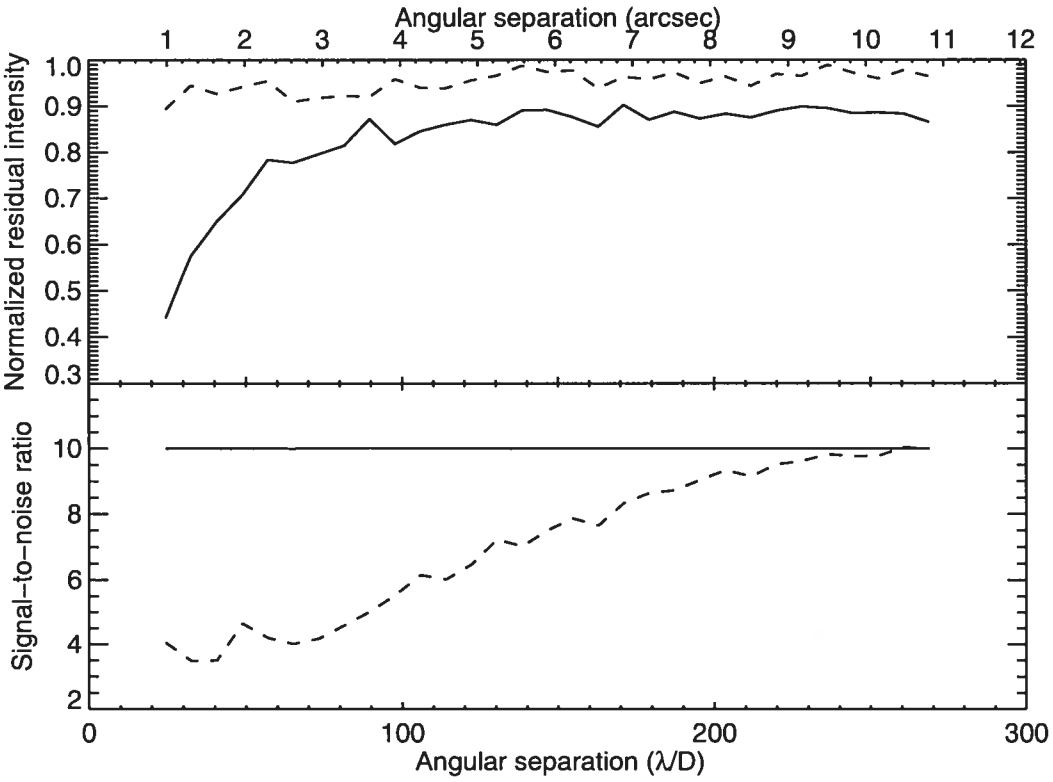

Figure 3.7 Average normalized residual intensity (*top*) and S/N ratio (*bottom*) as a function of angular separation for the LOCI algorithm (*solid line*) and the algorithm of Marois et al. (2006) (*dashed line*).

S/N that is better or equal to that obtained with the algorithm of Marois et al. (2006). The gain is highest at small separations, where it reaches a factor ~3, and steadily decreases for larger separations. The decrease is most likely due to the increasing relative importance of sky background noise. A comparison of the residual image of the two algorithms is shown in Figure 3.8; the lower level of noise of the LOCI algorithm is clearly visible. The new algorithm yields a better attenuation because it can adapt more easily to temporal and spatial variations of the PSF quasi-static speckle pattern by using all the images available with proper weights (the coefficients) and optimizing the reference image combination in smaller subsections.

The subtraction algorithms were then applied to the original sequence of images, i.e.

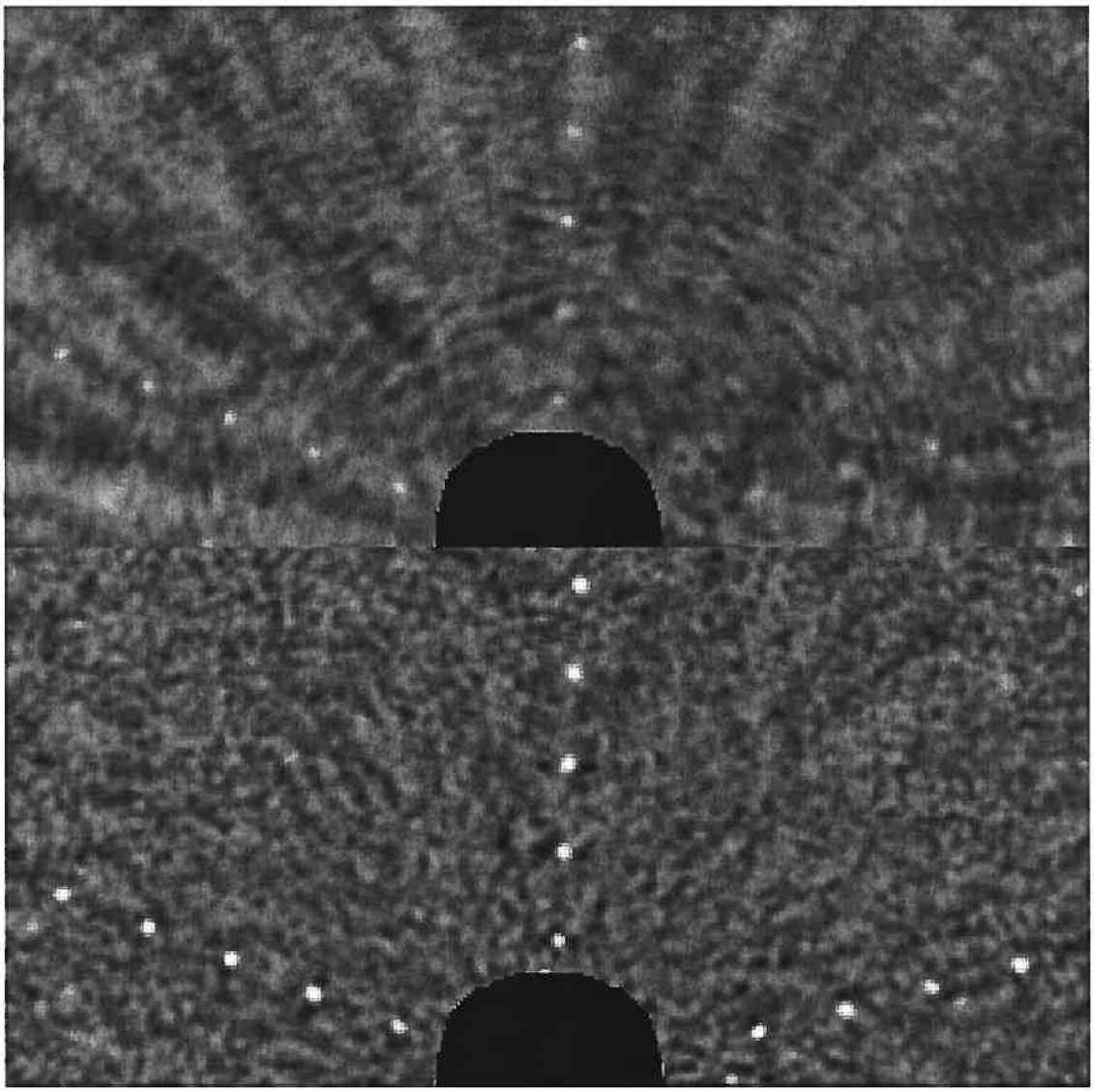

Figure 3.8 Residual S/N image (including artificial point sources) using the algorithm of Marois et al. (2006) (*top*) and the LOCI algorithm (*bottom*). Both panels are shown with a (-5,+10) intensity range. Each panel is 6.″5 by 3.″25. The images have been convolved by a circular aperture of diameter equal to W. The saturated region at the center of the PSF is masked out.

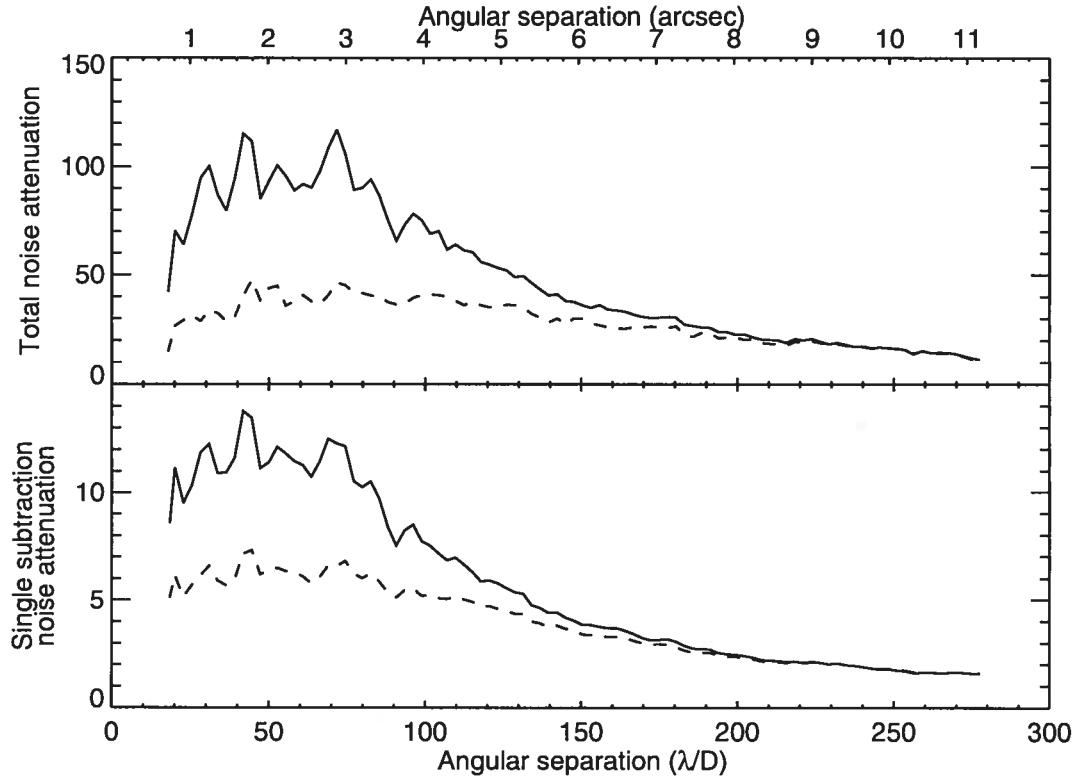

Figure 3.9 Noise attenuation resulting from a single reference image subtraction (*bottom*) and total noise attenuation (*top*). The noise attenuation is defined as the ratio of the noise in the target image over that in the residual image; the noise is computed as the standard deviation of the pixel values inside an annulus of width ~1 PSF FWHM. The dashed and solid lines are respectively for the algorithm of Marois et al. (2006) and the LOCI algorithm. The attenuations have been corrected for the partial subtraction of point sources. Before computation of the initial noise level, a 7×7 PSF FWHM median filter was subtracted from the images to remove the low spatial frequency structures that do not prevent point source detection.

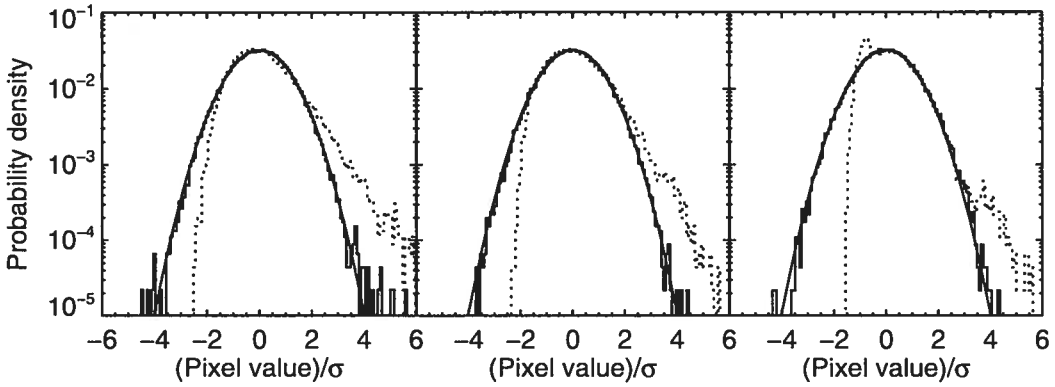

Figure 3.10 Statistical distributions of the pixel values of one original S/N image after subtraction of a radial profile (*dotted line*) and of the final S/N residual image (*solid line*) obtained with the LOCI algorithm. From left to right, the three panels are for angular separations of 25, 50 and 150 λ/D respectively. Both images have been convolved by a circular aperture of diameter equal to W and annuli of area equal to 5000 $\pi(W/2)^2$ were used to obtain the distributions at each separation. The continuous solid curve shows a Gaussian distribution of unit standard deviation.

without artificial sources, to compare the quasi-static speckle noise attenuation they provide and the detection limits they achieve. The quasi-static speckle noise attenuation is shown in Figure 3.9; a single subtraction using the LOCI algorithm provides an attenuation of ~10-12 at separations of 1-3 arcsec. The formulation of a simple and universal criterion for speckle-limited point source detection is usually complicated because the distribution of speckle noise is non Gaussian (Schneider & Silverstone, 2003; Aime & Soummer, 2004; Marois, 2004; Fitzgerald & Graham, 2006); it possesses an important tail at the higher end. However, ADI leads to residuals whose distribution closely resembles a Gaussian; this is studied in more detail elsewhere (C. Marois et al., in preparation). This was indeed verified for the data presented here, see Figure 3.10; a few events above a Gaussian distribution are seen only at the smallest angular separations. A 5σ threshold is thus adequate for estimating detection limits. The final 5σ detection limits in difference of magnitudes reach 13.9, 16.1 and 16.9 at angular separations of 1, 2 and 3 arcsec respectively, see Figure 3.11. The speckle noise attenuation and the detection limits have

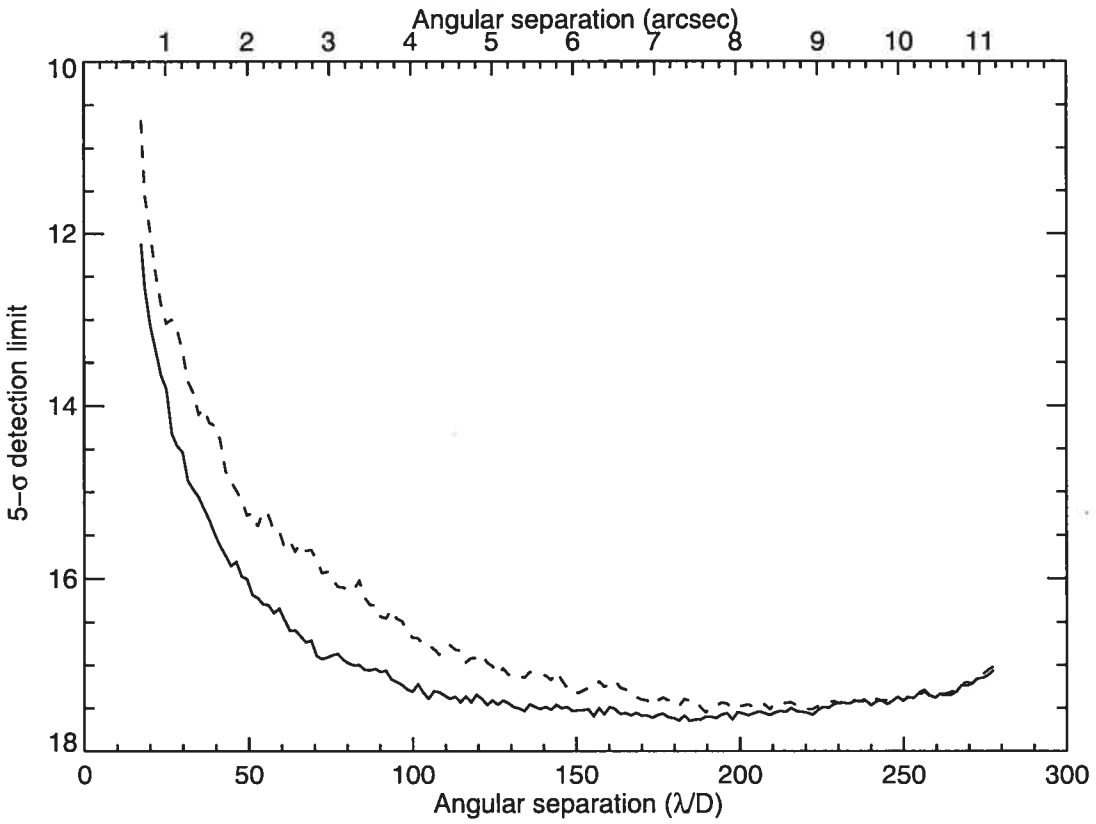

Figure 3.11 Point source detection limit. The dashed and solid lines are respectively for the algorithm of Marois et al. (2006) and the LOCI algorithm. The detection limits have been corrected for the partial subtraction of point sources, for the anisoplanatism observed with ALTAIR and for the slight smearing of point sources during an exposure due to FOV rotation.

been properly corrected for the partial loss of signal of point sources as measured from the residual signal of artificial sources.

Comparison of the two algorithms were made using a few different observation sequences and similar results were obtained every time.

3.5 Conclusion

An algorithm to construct an optimized reference PSF image used to subtract the speckle noise and improve the sensitivity to faint companion detection was developed and tested. For a given target image limited by speckle noise, the algorithm linearly

combines many reference PSF images such that the subtraction of this combination from the target image minimizes the speckle noise. Optimization of the coefficients of the linear combination is done for multiple subsections of the image independently and the procedure ensures that the minimum residual noise is reached within each subsection. The application of the algorithm to ADI yielded a factor of up to 3 improvement at small separations over the algorithm used in Marois et al. (2006).

The algorithm presented in §3.2 is general and can be used with most high contrast imaging observations aimed at finding point sources. In particular, it can be used with a sequence of images of the target itself obtained at different FOV orientations (ADI, roll subtraction for HST (Schneider & Silverstone, 2003), ground-based observations with discrete instrument rotations, etc.), with images of the same target at different wavelengths (simultaneous spectral differential imaging (SSDI, Racine et al., 1999; Marois et al., 2000) or non-simultaneous spectral differential imaging (NSDI) with, for example, a tunable filter) or with images of reference stars acquired with the same instrument in a similar configuration. The latter could be particularly interesting for HST for which the PSF is more stable than at any ground-based telescope and for which suitable observations of reference stars may be readily retrieved from the archive. This should also be the case for the James Webb Space Telescope (JWST), whose temperature is expected to be much more stable as a result of its more stable environment. Future ground-based instrumentation designed specifically for finding exoplanets will have a small FOV, rendering SSDI inefficient to detect planets whose spectrum has no steep feature and ADI inefficient because of the very long time baseline required for sufficient rotation. For such cases, discrete instrument rotations may be critical and the algorithm developed here could be used directly. The Fine Guidance Sensor onboard JWST (Rowlands et al., 2004a), which will include a tunable filter imager (Rowlands et al., 2004b) and coronagraph (Doyon et al., 2004), is a very interesting prospect for NSDI. Again, the algorithm developed here could be applied directly to this case.

Acknowledgments

This work is based on observations obtained at the Gemini Observatory, which is operated by the Association of Universities for Research in Astronomy, Inc., under a cooperative agreement with the NSF on behalf of the Gemini partnership: the National Science Foundation (United States), the Particle Physics and Astronomy Research Council (United Kingdom), the National Research Council (Canada), CONICYT (Chile), the Australian Research Council (Australia), CNPq (Brazil) and CONICET (Argentina). This work was supported in part through grants from the Natural Sciences and Engineering Research Council, Canada, from Fonds Québécois de la Recherche sur la Nature et les Technologies and from the Faculté des Études Supérieures de l'Université de Montréal. This research was performed in part under the auspices of the US Department of Energy by the University of California, Lawrence Livermore National Laboratory under contract W-7405-ENG-48, and also supported in part by the National Science Foundation Science and Technology Center for Adaptive Optics, managed by the University of California at Santa Cruz under cooperative agreement AST 98-76783.

References

Aime, C., & Soummer, R. 2004, ApJ, 612, L85

Biller, B. A., Close, L., Lenzen, R., Brandner, W., McCarthy, D. W., Nielsen, E., & Hartung, M. 2004, in Proc. SPIE, Vol. 5490, Advancements in Adaptive Optics, ed. D. Bonaccini Calia, B. L. Ellerbroek, & R. Ragazzoni, 389-397

Doyon, R., Lafrenière, D., Rowlands, N., Evans, C., Murowinski, R., Hutchings, J. B., & Alexander, R. 2004, in Proc. SPIE, Vol. 5487, Optical, Infrared, and Millimeter Space Telescopes, ed. J. C. Mather, 746-753

Fitzgerald, M. P., & Graham, J. R. 2006, ApJ, 637, 541

Kuhn, J. R., Potter, D., & Parise, B. 2001, ApJ, 553, L189

Lenzen, R., Close, L., Brandner, W., Biller, B., & Hartung, M. 2004, in Proc. SPIE, Vol. 5492, Ground-based Instrumentation for Astronomy, ed. A. F. M. Moorwood & M. Iye, 970-977

Macintosh, B. A., Becklin, E. E., Kaisler, D., Konopacky, Q., & Zuckerman, B. 2003, ApJ, 594, 538

Marois, C. 2004, Ph.D. Thesis

Marois, C., Doyon, R., Nadeau, D., Racine, R., Riopel, M., Vallée, P., & Lafrenière, D. 2005, PASP, 117, 745

Marois, C., Doyon, R., Racine, R., & Nadeau, D. 2000, PASP, 112, 91

Marois, C., Lafrenière, D., Doyon, R., Macintosh, B., & Nadeau, D. 2006, ApJ, 641, 556

Masciadri, E., Mundt, R., Henning, T., Alvarez, C., & Barrado y Navascués, D. 2005, ApJ, 625, 1004

Metchev, S. A., Hillenbrand, L. A., & White, R. J. 2003, ApJ, 582, 1102

Racine, R., Walker, G. A. H., Nadeau, D., Doyon, R., & Marois, C. 1999, PASP, 111, 587

Rowlands, N. 2004a, in Proc. SPIE, Vol. 5487, Optical, Infrared, and Millimeter Space Telescopes, ed. J. C. Mather, 664-675

Rowlands, N. 2004b, in Proc. SPIE, Vol. 5487, Optical, Infrared, and Millimeter Space Telescopes, ed. J. C. Mather, 676-687

Schneider, G., & Silverstone, M. D. 2003, in Proc. SPIE, Vol. 4860, High-Contrast Imaging for Exo-Planet Detection, ed. A. B. Schultz, 1-9

CHAPITRE 4

UNE RECHERCHE DE PLANÈTES GÉANTES PAR IMAGERIE DIFFÉRENTIELLE ANGULAIRE

THE GEMINI DEEP PLANET SURVEY – GDPS

DAVID LAFRENIÈRE[a], RENÉ DOYON[a], CHRISTIAN MAROIS[b], DANIEL NADEAU[a], BEN R. OPPENHEIMER[c], PATRICK F. ROCHE[d], FRANÇOIS RIGAUT[e], JAMES R. GRAHAM[f], RAY JAYAWARDHANA[g], DOUG JOHNSTONE[h], PAUL G. KALAS[f], BRUCE MACINTOSH[b], AND RENÉ RACINE[a]

Submitted to: *The Astrophysical Journal*, 28 May 2007

Abstract

We present the results of the Gemini Deep Planet Survey, a near-infrared adaptive optics search for giant planets and brown dwarfs around nearby young stars. The observations were obtained with the Altair adaptive optics system at the Gemini North telescope and angular differential imaging was used to suppress the speckle noise of the

[a]Département de physique and Observatoire du Mont Mégantic, Université de Montréal, C.P. 6128 Succ. Centre-Ville, Montréal, QC, H3C 3J7, Canada

[b]Institute of Geophysics and Planetary Physics L-413, Lawrence Livermore National Laboratory, 7000 East Ave, Livermore, CA 94550

[c]Department of Astrophysics, American Museum of Natural History, Central Park West at 79th Street, New York, NY 10024

[d]Astrophysics, Physics Department, University of Oxford, 1 Keble Road, Oxford, OX1 3RH, UK

[e]Gemini Observatory, Southern Operations Center, Association of Universities for Research in Astronomy, Inc., Casilla 603, La Serena, Chile

[f]Department of Astronomy, University of California at Berkeley, 601 Campbell Hall, Berkeley, CA 94720

[g]Department of Astronomy and Astrophysics, University of Toronto, 50 St. George Street, Toronto, ON, M5S 3H4, Canada

[h]National Research Council Canada, Herzberg Institute of Astrophysics, 5071 West Saanich Road, Victoria, BC, V9E 2E7, Canada

central star. Detection limits for the 85 stars observed are presented, along with a list of all faint point sources detected around them. Typically, the observations are sensitive to angular separations beyond 0.5″ with 5σ contrast sensitivities in magnitude difference at 1.6 μm of 9.5 at 0.5″, 12.9 at 1″, 15.0 at 2″, and 16.5 at 5″. For the typical target of the survey, a 100 Myr old K0 star located 22 pc from the Sun, the observations are sensitive enough to detect planets more massive than 2 $M_{\rm Jup}$ with a projected separation in the range 40–200 AU. Depending on the age, spectral type, and distance of the target stars, the detection limit can be as low as $\sim$1 $M_{\rm Jup}$. Second epoch observations of 48 stars with candidates (out of 54) have confirmed that all candidates are unrelated background stars. A detailed statistical analysis of the survey results, yielding upper limits on the fractions of stars with giant planet or low mass brown dwarf companions, is presented. Assuming a planet mass distribution $dn/dm \propto m^{-1.2}$ and a semi-major axis distribution $dn/da \propto a^{-1}$, the 95% credible upper limits on the fraction of stars with at least one planet of mass 0.5–13 $M_{\rm Jup}$ are 0.28 for the range 10–25 AU, 0.13 for 25–50 AU, and 0.093 for 50–250 AU; this result is weakly dependent on the semi-major axis distribution power-law index. The 95% credible interval for the fraction of stars with at least one brown dwarf companion having a semi-major axis in the range 25–250 AU is $0.019^{+0.083}_{-0.015}$, irrespective of any assumption on the mass and semi-major axis distributions. The observations made as part of this survey have resolved the stars HD 14802, HD 166181, and HD 213845 into binaries for the first time.

Subject headings: Planetary systems — stars: imaging — binaries: close — stars: low-mass, brown dwarfs

4.1 Introduction

More than 200 exoplanets have been discovered over the last decade through precise measurements of variations of the radial velocity (RV) of their primary star. Besides establishing that at least 6–7% of FGK stars have at least one giant planet with a semi-

major axis smaller than ~5 AU (Marcy et al., 2005), the profusion of data following from the RV discoveries has propelled the field of giant planet formation and evolution into an unprecedented state of activity. For a review of the main characteristics of the RV exoplanets, the reader is referred to Udry et al. (2007); Butler et al. (2006); Marcy et al. (2005). Besides the RV technique, the photometric transit method has lead successfully to the discovery of new exoplanets on small orbits (e.g. Konacki et al., 2003; Alonso et al., 2004; Cameron et al., 2007) and has provided the first measurements of the radius and mean density of giant exoplanets (e.g. Charbonneau et al., 2000). Very recently, a few exoplanets have been detected by gravitational microlensing (Bond et al., 2004; Udalski et al., 2005; Beaulieu et al., 2006; Gould et al., 2006); these planets have separations of ~2–5 AU. Notwithstanding their great success in finding planets on small orbits, these techniques cannot be used to search for and characterize planets on orbits larger than ~10 AU. As a result, the population of exoplanets on large orbits is currently unconstrained.

The two main models of giant planet formation are core accretion (Pollack et al., 1996) and gravitational instability (Boss, 1997, 2001). In the core accretion model, solid particles within a proto-planetary disk collide and grow into solid cores which, if they become massive enough before the gas disk dissipates, trigger runaway gas accretion and become giant planets. Models predict that the timescale for formation of a planet like Jupiter through this process is about 5 Myr (Pollack et al., 1996), or about 1 Myr if migration of the core through the disk is allowed as the planet forms (Alibert et al., 2005). These timescales are comparable to or below the estimated proto-planetary dust disk lifetime (~6 Myr, Haisch et al., 2001) and gas disk lifetime ($\lesssim$10 Myr, Jayawardhana et al., 2006). Formation through core accretion is strongly dependent on the surface density of solid material (hence [Fe/H]) in the proto-planetary disk , precluding formation of Jupiter mass planets at distances greater than 15–20 AU (e.g. Pollack et al., 1996; Ida & Lin, 2004), where the low density of planetesimals would lead to prohibitively long formation timescales. Neptune mass planets can be formed out to slightly larger

distances and can further migrate outward owing to interaction with the disk.

In the gravitational instability model, small instabilities in a proto-planetary disk grow rapidly into regions of higher density that subsequently evolve into spiral arms owing to Keplerian rotation. Further interactions between these spiral arms lead to the formation of hot spots which then collapse to form giant planets. The range of orbital separation over which this mechanism may operate efficiently is not yet clear. Some studies indicate that it may lead to planet formation only at separations exceeding $\sim$100 AU (Whitworth & Stamatellos, 2006; Matzner & Levin, 2005), where the radiative cooling timescale is sufficiently short compared to the dynamical timescale, while others have been able to produce planets only at separations below 20–30 AU (Boss, 2000, 2003, 2006).

A few other models are capable of forming giant planets on large orbits directly. One such mechanism is shock-induced formation following collision between disks (Shen & Wadsley, 2006). In this model, the violent collision of two proto-planetary disks triggers instabilities that lead to the collapse of planetary or brown dwarf (BD) mass clumps. Results of numerical simulations indicate that planets and BDs may form at separations of several tens of AU or more through this process (Shen & Wadsley, 2006). The competitive accretion and ejection mechanism that was proposed initially to explain the formation of BDs (Reipurth & Clarke, 2001) could also form planetary mass companions on large orbits, as suggested by the results of recent simulations by Bate & Bonnell (2005).

Even in a scenario in which all giant planets form on small orbits, through either core accretion or gravitational collapse, a significant fraction of planets could be found on stable orbits of tens of AU because of outward orbital migration. Indeed, numerical simulations have shown that gravitational interactions between planets in a multi-planet system may send one of the planets, usually the least massive one, out to an eccentric orbit of semi-major axis of tens to hundreds of AU (Chatterjee et al., 2007; Veras & Armitage, 2004; Rasio & Ford, 1996; Weidenschilling & Marzari, 1996). This pro-

cess could be involved frequently in the shaping of the orbital parameters of planetary systems as we have learned from RV surveys that multi-planet systems are common, representing ~14% of known planetary systems (Marcy et al., 2005). Outward migration of massive planets can be induced also by interactions between the planet and the gaseous disk; the simulations of Veras & Armitage (2004) reveal that this process is capable of carrying Jupiter mass planets out to several tens of AU. Similarly, angular momentum exchange between two planets (or more), achieved through viscous interactions with the disk, could drive the outer planet to a separation of hundreds of AU (Martin et al., 2007). Outward planet migration can result further from interaction of the planet with the solid particles in the disk after the gas has dissipated (e.g. Levison et al., 2007); there is in fact strong evidence that this mechanism has played an important role in the Solar system (Fernandez & Ip, 1984; Malhotra, 1995; Hahn & Malhotra, 2005). Based on numerical simulations, it is likely that all giant planets of the Solar system formed interior to ~15 AU and migrated outward (except Jupiter) to their current location (Tsiganis et al., 2005).

From an observational point of view, there is some evidence that planets on large orbits may exist. Many observations of dusty disks around young stars, made either in emitted light (e.g. Vega, ε Eri, Fomalhaut; Holland et al., 1998; Greaves et al., 1998) or in scattered light (e.g. HD 141569, HR 4796, Fomalhaut; Augereau et al., 1999; Weinberger et al., 1999; Schneider et al., 1999; Kalas et al., 2005), have unveiled asymmetric or ring-like dust distributions. These peculiar morphologies could arise from gravitational dust confinement imposed by one or more (unseen) giant planets on orbits of tens to hundreds of AU. In fact, detailed numerical simulations of the effect of giant planets on the dynamical evolution of dusty disks have been able to reproduce the observed morphologies with remarkable agreement (Ozernoy et al., 2000; Wilner et al., 2002; Deller & Maddison, 2005). Typically, Jupiter mass planets on orbits of ~60 AU are needed to reproduce the observations, although in some cases less massive planets (similar to Neptune) may be able to reproduce the observed features.

In the last few years, there have been a few discoveries of planetary mass or low-mass BD companions located beyond several tens of AU, in projection, from their primary: an $\sim$8 $M_{\rm Jup}$ companion 40 AU from the BD 2M 1207$-$3932 (Mohanty et al., 2007; Chauvin et al., 2005a, 2004), a $\sim$25 $M_{\rm Jup}$ companion 100 AU from the T Tauri star GQ Lup (Marois et al., 2007a; Seifahrt et al., 2007; Neuhäuser et al., 2005), a $\sim$12 $M_{\rm Jup}$ companion 210 AU from the young star CHXR 73 (Luhman et al., 2006), a $\sim$25 $M_{\rm Jup}$ companion 240 AU from the young BD 2M 1101$-$7732 (Luhman, 2004), a $\sim$12 $M_{\rm Jup}$ companion 260 AU from the young star AB Pic (Mohanty et al., 2007; Chauvin et al., 2005b), a 7–19 $M_{\rm Jup}$ companion 240–300 AU from the young BD Oph 1622$-$2405 (Luhman et al., 2007a; Close et al., 2007; Jayawardhana et al., 2006), an $\sim$11 $M_{\rm Jup}$ companion 330 AU from the T Tauri star DH Tau (Luhman et al., 2006; Itoh et al., 2005), and a $\sim$21 $M_{\rm Jup}$ companion 790 AU from the star HN Peg (Luhman et al., 2007b). These discoveries might indicate that more similar companions, and less massive ones, do exist and remain to be found.

Perhaps even more compelling is the fact that the number of exoplanets found by RV surveys increases as a function of semi-major axis for the range 0.1–3 AU (Butler et al., 2006); these surveys are incomplete at larger separations. Conservative extrapolation suggests that there may be at least as many planets beyond 3 AU as there are within (Butler et al., 2006). In fact, long-term trends in RV data have been detected for about 5% of the stars surveyed (Marcy et al., 2005), suggesting the presence of planets between 5 AU and 20 AU around them.

Given all of the considerations above, it is clear that a determination of the frequency of giant planets as a function of orbital separation out to hundreds of AU is necessary to elucidate the relative importance of the various modes of planet formation and migration. Direct imaging is currently the only viable technique to probe for planets on large separations and achieve this goal. However, detecting giant planets directly through imaging is very difficult due to the angular proximity of the star and the very large luminosity ratios involved. Currently, the main technical difficulty when trying to image giant

planets directly does not come from diffraction of light by the telescope aperture, from light scattering due to residual atmospheric wavefront errors after adaptive optics (AO) correction, nor from photon noise of the stellar point spread function (PSF), but rather from light scattering by optical imperfections of the telescope and camera that produce bright quasi-static speckles in the PSF of the central star. These speckles are usually much brighter than the planets sought after. More in depth discussions of this problem, as well as possible venues to circumvent it using current instrumentation, can be found in Lafrenière et al. (2007); Hinkley et al. (2007); Marois et al. (2006, 2005); Masciadri et al. (2005); Biller et al. (2004); Schneider & Silverstone (2003); Marois et al. (2003); Sparks & Ford (2002); Marois et al. (2000); Racine et al. (1999). As AO systems continue to improve and eventually achieve Strehl ratios above ~90%, the light diffracted by the telescope aperture will become more important compared to scattered light and the use of a coronagraph will be mandatory. But even then, after removal of diffracted light by the coronagraph, high-contrast imaging applications will likely be limited by residual quasi-static speckles (e.g. Macintosh et al., 2006).

Many direct imaging searches for planetary or brown dwarf companions to stars have been done during the last five years, see for example Biller et al. (2007); Chauvin et al. (2006); Metchev (2006); Lowrance et al. (2005); Masciadri et al. (2005); McCarthy & Zuckerman (2004); and Luhman & Jayawardhana (2002) for searches carried out in J, H, or K, or Kasper et al. (2007) and Heinze et al. (2006) for searches made in L' or M'. Depending on the observing strategy employed, the properties of the target stars, and the characteristics of the instrument used, each of these surveys was sensitive to a different regime of companion masses and separations. Typically, these surveys have reached detection contrasts of 10–13 mag for angular separations beyond $1''$–$2''$, sufficient to detect planets more massive than $\sim 5\ M_{\rm Jup}$ for targets aged ~100 Myr. Unfortunately, rigorous statistical analyses allowing derivation of clear constraints on the population of planets in the regimes of mass and separation to which these surveys were sensitive

are only beginning to be reported in the literature[1]; an assessment of the current status of knowledge is thus rather difficult to make. Nonetheless, it is fair to say that the population of planets less massive than $\sim$5 $M_{\rm Jup}$, having orbits with a semi-major axis of tens to hundreds of AU, is poorly constrained.

In this paper we report the results of the Gemini Deep Planet Survey (GDPS), a direct imaging survey of 85 nearby young stars aimed at constraining the population of Jupiter mass planets with orbits of semi-major axis in the range 10-300 AU. The selection of the GDPS target sample is explained in §4.2, and the observations and data reduction are detailed in §4.3. The detection limits achieved for each target are then presented in §4.4 along with all candidate companions detected. A statistical analysis of the results allowing determination of the maximum fraction of stars that could bear planetary companions is presented in §4.5. Concluding remarks follow in §4.6.

4.2 Target sample

In light of the luminosity ratio and angular separation problem highlighted above, the list of target stars was assembled mainly on the basis of young age and proximity to the Sun, the latter yielding a larger angular separation for a given physical distance between the star and an eventual planet. Equivalently, a given detection threshold is achieved at a smaller physical separation for a star closer to the Sun, and planets on smaller orbits can be detected. Additionally, for angular separations where planet detection is limited by sky background noise or read noise, lower mass planets can be detected around a star closer to the Sun as their apparent brightness would be larger. Giant planets are intrinsically more luminous at young ages and fade with time (e.g. Marley et al., 2007; Baraffe et al., 2003; Burrows et al., 1997); therefore, for a given detection threshold, observations of younger stars are sensitive to planets having a lower mass. The proximity and age criteria used in building the target list thus maximize the range of mass and

[1] In addition to the present work, analyses by Nielsen et al. (2007) and Kasper et al. (2007) have become available during the review process of this manuscript.

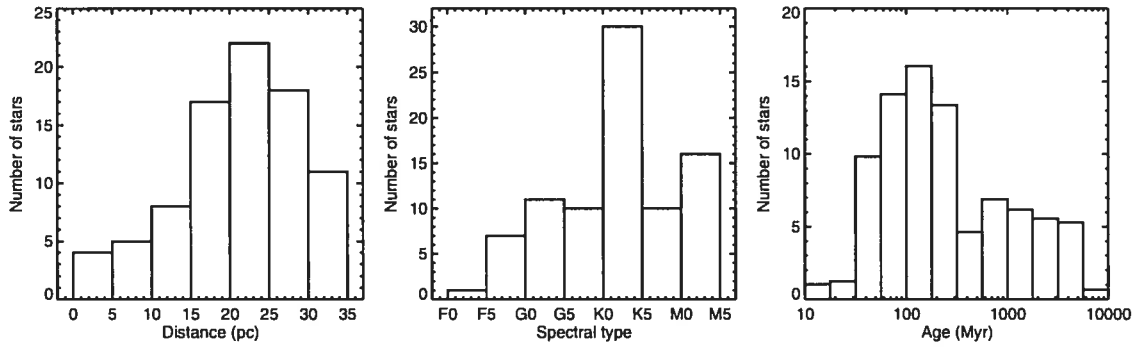

Figure 4.1 Distribution of distance, spectral type, and age of the target stars. For the age distribution, each star was distributed over all the age bins according to the fraction of their estimated age interval falling inside each bin.

separation over which the survey is sensitive.

The target stars were selected from three sources: (1) Tables 3 and 4 of Wichmann et al. (2003), which list nearby stars with an estimated age below or comparable to that of the Pleiades (∼100 Myr), based on measurements of lithium abundance, space velocity, and X-ray activity; (2) Tables 2 and 5 of Zuckerman & Song (2004b), which list members of the β Pictoris (∼12 Myr) and AB Doradus (∼50 Myr) moving groups respectively; and (3) Tables 2 and 5 of Montes et al. (2001b), which list late-type single stars that are possible members of the Local Association (Pleiades moving group, 20–150 Myr) and IC 2391 supercluster (35–55 Myr) respectively, based on space velocity measurements. The stars listed in Montes et al. (2001b) were initially selected based on various criteria indicative of youth, such as kinematic properties, rotation rate, chromospheric activity, lithium abundance, or X-ray emission, but for many of these stars the space velocity is the only indication of youth as other measurements are either unavailable or inconclusive; the young age of such stars is therefore uncertain. This uncertainty will be taken into account in our statistical analysis (§4.5). A few stars known to have a circumstellar disk were added to these lists.

From this preliminary compilation, we have retained only stars with a distance smaller than 35 pc, and we have excluded stars of declination below $-32°$ since observations

were to be made from the Gemini North observatory. Finally, we have further excluded stars indicated to be multiple in Zuckerman & Song (2004b). This procedure yielded a list of slightly over 100 target stars, of which 85 were actually observed. The properties of these 85 stars are presented in Table 4.1 and Figure 4.1. The median spectral type of our sample is K0, the median H magnitude is 5.75, the median distance is 22 pc, the median proper motion amplitude is 240 mas yr^{-1}, and the median [Fe/H] is 0.00 dex (standard deviation of 0.21 dex).

Despite our effort to select only single stars, our observations show that 16 of the 85 target stars are close double or triple systems; this is indicated in the last column of Table 4.1. A thorough review of the literature revealed that 11 of these were known at the time the target list was compiled, two of which are astrometric multiples that had never been resolved prior to our observations (HD 14802 and HD 166181). Five other multiple systems were resolved with AO only after the target list was compiled (HD 77407, HD 129333, HD 135363, HD 160934, and HD 220140). Finally, the star HD 213845 is reported to be part of a binary system for the first time here. The multiple systems observed are discussed further in §4.4.3.

Age estimates for the stars in our sample, needed to convert the observed contrasts into mass detection limits using evolution models of giant planets,[2] are reported in Table 4.1 along with the references used for their determination. Whenever possible, we have used ages stated explicitly in the literature or the age of the association to which a star belongs. When no specific age estimate was available for stars taken from Wichmann et al. (2003), ages of 10–50 Myr or 50–150 Myr were assigned to the stars having a lithium abundance above or comparable to that of the Pleiades, respectively. For other stars that have lithium and/or X-ray measurements, ages were estimated from a comparison of the Li I 6708 Å equivalent width and/or the ratio of the X-ray to bolometric luminosity with Figures 3 and/or 4 of Zuckerman & Song (2004b) respectively. When lithium or X-ray measurements were not available, the kinematic ages were used

[2]It is assumed that any planet and its primary star would be coeval.

as lower limits while the ages derived from the chromospheric activity index, $\log R_{\rm HK}$, were used as upper limits, as Song et al. (2004) showed that the latter ages tend to be systematically higher than those derived from lithium abundance or X-ray emission. When only the value of $\log R_{\rm HK}$ was available, the calibration of Donahue (1993)[3] was used to obtain an age estimate. Finally, when only kinematics measurements were available for a given star, an age of 100–5000 Myr or 50–5000 Myr was assigned if the star is a possible member of the Local Association or the IC 2391 supercluster respectively.

[3]This calibration is given explicitly in Henry et al. (1996).

Table 4.1. GDPS target sample

Names				α	δ	Spectral	H	Dist.[a]	$\mu_\alpha \cos\delta$[a]	μ_δ[a]	[Fe/H]	[Fe/H]	Age	Age	Notes
HD	GJ	HIP	Other	(J2000)	(J2000)	Type	(mag)	(pc)	(mas/yr)	(mas/yr)		Ref.	(Myr)	Ref.	
166	5	544	-	$00^h06^m36^s.78$	+29°01′17.″4	K0 V	4.63	13.7	379.9	−178.3	0.18	V05	150–300	G98,G00,F04,L06	Her-Lyr
691	-	919	V344 And	$00^h11^m22^s.44$	+30°26′58.″5	K0 V	6.26	34.1	210.7	35.3	0.32	V05	50–280	W03,W04,C05	-
1405	-	-	PW And	$00^h18^m20^s.90$	+30°57′22.″0	K2 V	6.51	30.6[b]	143.7[b]	−171.5[b]	-0.78	N04	50–50	Z04b	AB Dor
5996	-	4907	-	$01^h02^m57^s.22$	+69°13′37.″4	G5 V	5.98	25.8	223.9	−148.4	-0.28	K02	100–650	M01a,G03	?LA
9540	59A	7235	-	$01^h33^m15^s.81$	−24°10′40.″7	K0 V	5.27	19.5	271.9	−159.5	-0.02	V05	100–1350	M01a,W04	?LA
10008	-	7576	-	$01^h37^m35^s.47$	−06°45′37.″5	G5 V	5.90	23.6	171.0	−97.7	-	-	150–300	F04,L06	Her-Lyr
-	82	9291	V596 Cas	$01^h59^m23^s.51$	+58°31′16.″1	dM4e	7.22	12.0	321.8	−195.3	-	-	50–50	M06	α Per
14802	97	11072	kap For	$02^h22^m32^s.55$	−23°48′58.″8	G2 V	3.71	21.9	197.3	−4.4	-0.04	T05b	5000–6700	L99,W04,B99	m
16765	-	12530	84 Cet	$02^h41^m14^s.00$	−00°41′44.″4	F7 V	4.64	21.6	218.9	−125.3	-0.27	N04	100–400	M01a,H98,F95	LA,m
17190	112	12926	-	$02^h46^m15^s.21$	+25°38′59.″6	K1 V	6.00	25.7	238.7	−149.9	-0.11	V05	50–3500	M01a,W04	?IC 2391
17382	113	13081	-	$02^h48^m09^s.14$	+27°04′07.″1	K1 V	5.69	22.4	264.2	−127.8	0.12	T05b	50–600	M01a,W04	?IC 2391
17925	117	13402	EP Eri	$02^h52^m32^s.13$	−12°46′11.″0	K2 V	4.23	10.4	398.1	−189.6	0.18	V05	40–128	W03,M01a,M01b,L99	LA
18803	120.2	14150	51 Ari	$03^h02^m26^s.03$	+26°36′33.″3	G8 V	5.02	21.2	234.2	−168.2	0.11	V05	800–3600	W04,T05a	-
19994	128	14954	94 Cet	$03^h12^m46^s.44$	−01°11′46.″0	F8 V	3.77	22.4	193.4	−69.2	0.19	V05	800–3500	W04,T05a	m
20367	-	15323	-	$03^h17^m40^s.05$	+31°07′37.″4	G0 V	5.12	27.1	−103.1	−56.6	0.17	S04a	50–150	W03	-
-	-	-	2E 759	$03^h20^m49^s.50$	−19°16′10.″0	K7 V	7.66	27.0	90.8	−43.8	-	-	50–150	M01a,L06	LA
22049	144	16537	eps Eri	$03^h32^m55^s.84$	−09°27′29.″7	K2 V	1.88	3.2	−976.4	18.0	-0.03	V05	530–930	S00	-
-	-	17695	-	$03^h47^m23^s.35$	−01°58′19.″9	M3e	7.17	16.3	186.7	−271.8	-	-	80–120	L06	LA (B4)
25457	159	18859	-	$04^h02^m36^s.74$	−00°16′08.″1	F6 V	4.34	19.2	151.2	−252.0	0.02	T05b	80–120	L06	LA (B4)
283750	171.2	21482	V833 Tau	$04^h36^m48^s.24$	+27°07′55.″9	K2 V	5.40	17.9	232.4	−147.1	-	-	50–150	W03	-
30652	178	22449	1 Ori	$04^h49^m50^s.41$	+06°57′40.″6	F6 V	1.76	8.0	463.4	11.6	0.03	V05	50–500	M01a,H99	IC 2391
-	182	23200	V1005 Ori	$04^h59^m34^s.83$	+01°47′00.″7	M1 V	6.45	26.7	37.1	−93.9	-	-	10–50	F98,B99	-
-	234A	30920	V577 Mon	$06^h29^m23^s.40$	−02°48′50.″3	M4	5.75	4.1	694.7	−618.6	-	-	100–3000	M01a,M03	?LA,m
-	281	37288	-	$07^h39^m23^s.04$	+02°11′01.″2	K7	6.09	14.9	−147.9	−246.6	-	-	150–300	L06	Her-Lyr
-	285	37766	YZ CMi	$07^h44^m40^s.17$	+03°33′08.″8	M4.5 V	6.01	5.9	−344.9	−450.8	-	-	50–50	Z,M01	LA
72905	311	42438	3 Uma	$08^h39^m11^s.70$	+65°01′15.″3	G1.5 V	4.28	14.3	−27.7	87.9	-0.09	T05b	300–300	S93,M01b	U Ma
75332	-	43410	-	$08^h50^m32^s.22$	+33°17′06.″2	F7 Vn	5.04	28.7	−62.2	−85.0	0.14	V05	50–150	W03	-
77407	-	44458	-	$09^h03^m27^s.08$	+37°50′27.″5	G0	5.53	30.1	−86.3	−168.8	0.10	V05	10–50	W03,M01a,M01b	LA,m
78141	-	-	-	$09^h07^m18^s.08$	+22°52′21.″6	K0 V	5.92	21.4[c]	−0.4[d]	−67.6[d]	-	-	50–150	W03	-
82558	355	46816	LQ Hya	$09^h32^m25^s.57$	−11°11′04.″7	K0 V	5.60	18.3	−248.2	35.1	0.33	V05	50–100	W03,M01b	-
82443	354.1	46843	DX Leo	$09^h32^m43^s.76$	+26°59′18.″7	K0 V	5.24	17.7	−147.5	−246.3	-0.10	T05b	50–150	W03,M01b	LA
-	393	51317	-	$10^h28^m55^s.55$	+00°50′27.″6	M2	5.61	7.2	−602.3	−731.9	-	-	80–120	L06	LA (B4)
90905	-	51386	-	$10^h29^m42^s.23$	+01°29′28.″0	F5	5.60	31.6	−151.4	−125.3	0.07	V05	50–150	W03	-
91901	-	51931	-	$10^h36^m30^s.79$	−13°50′35.″8	K2 V	6.64	31.6	−164.6	23.8	-0.03	K02	50–5000	M01a	?IC 2391
92945	3615	52462	-	$10^h43^m28^s.27$	−29°03′51.″4	K1 V	5.77	21.6	−215.4	−48.5	0.13	V05	80–120	L06,W03,S04b,W04	LA (B4)
93528	-	52787	-	$10^h47^m31^s.16$	−22°20′52.″9	K0 V	6.56	34.9	−122.7	−29.4	0.11	K02	50–150	W03,S02	-
-	402	53020	EE Leo	$10^h50^m52^s.06$	+06°48′29.″3	M4	6.71	5.6	−804.4	−809.6	-	-	150–300	L06	Her-Lyr

Table 4.1 — continued

Names				α	δ	Spectral	H	Dist.[a]	$\mu_\alpha \cos\delta$[a]	μ_δ[a]	[Fe/H]	[Fe/H]	Age	Age	Notes
HD	GJ	HIP	Other	(J2000)	(J2000)	Type	(mag)	(pc)	(mas/yr)	(mas/yr)		Ref.	(Myr)	Ref.	
96064	-	54155	-	$11^h04^m41\overset{s}{.}47$	$-04°13'15\overset{''}{.}9$	G4	5.90	24.6	−178.0	−104.1	-0.01	T05b	50–150	W03	m
97334	417	54745	-	$11^h12^m32\overset{s}{.}35$	$+35°48'50\overset{''}{.}7$	G0 V	5.02	21.7	−248.6	−151.3	0.09	V05	80–300	K01,M01a	?LA
102195	-	57370	-	$11^h45^m42\overset{s}{.}29$	$+02°49'17\overset{''}{.}3$	K0 V	6.27	29.0	−190.3	−111.4	0.05	S06	100–5000	M01a	?LA
102392	-	57494	-	$11^h47^m03\overset{s}{.}83$	$-11°49'26\overset{''}{.}6$	K2	6.36	24.6	−206.3	−60.7	-	-	100–5000	M01a	?LA,m
105631	3706	59280	-	$12^h09^m37\overset{s}{.}26$	$+40°15'07\overset{''}{.}4$	K0 V	5.70	24.3	−314.0	−51.3	0.20	V05	1600–1600	M01b,W04	-
107146	-	60074	-	$12^h19^m06\overset{s}{.}50$	$+16°32'53\overset{''}{.}9$	G2 V	5.61	28.5	−175.7	−148.3	-0.03	V05	50–100	W03,Z04a	-
108767B	-	-	del Crv B	$12^h29^m51\overset{s}{.}85$	$-16°30'55\overset{''}{.}6$	K0 V	6.37	26.9	−210.0	−139.3	-	-	40–260	R05,G01,M01a	LA
109085	471.2	61174	eta Crv	$12^h32^m04\overset{s}{.}23$	$-16°11'45\overset{''}{.}6$	F2 V	3.37	18.2	−424.4	−58.4	-0.05	N04	600–1300	M03,W05	-
-	-	-	BD+60 1417	$12^h43^m33\overset{s}{.}28$	$+60°00'52\overset{''}{.}7$	K0	7.36	17.7[c]	−125.2[d]	−66.4[d]	-	-	50–150	W03	-
111395	486.1	62523	-	$12^h48^m47\overset{s}{.}05$	$+24°50'24\overset{''}{.}8$	G5 V	4.71	17.2	−334.6	−106.1	0.13	V05	600–1200	H99,W04,T05a	-
113449	-	63742	-	$13^h03^m49\overset{s}{.}65$	$-05°09'42\overset{''}{.}5$	G5 V	5.67	22.1	−189.8	−219.6	-0.22	T05b	80–120	L06	LA (B4)
-	507.1	65016	-	$13^h19^m40\overset{s}{.}12$	$+33°20'47\overset{''}{.}5$	M1.5	6.64	17.4	−298.8	−143.9	-	-	100–5000	M01a	?LA
116956	-	65515	-	$13^h25^m45\overset{s}{.}53$	$+56°58'13\overset{''}{.}8$	G9 V	5.48	21.9	−217.4	11.2	0.06	T05b	100–500	M01a,G00	LA
118100	517	66252	EQ Vir	$13^h34^m43\overset{s}{.}21$	$-08°20'31\overset{''}{.}3$	K5 Ve	6.31	19.8	−287.4	−91.0	0.00	C97	50–50	L05,M01a	?LA
-	524.1	67092	-	$13^h45^m05\overset{s}{.}34$	$-04°37'13\overset{''}{.}2$	K5	7.33	25.7	−159.9	−95.3	-	-	100–5000	M01a	?LA
124106	3827	69357	-	$14^h11^m46\overset{s}{.}17$	$-12°36'42\overset{''}{.}4$	K1 V	5.95	23.1	−257.5	−179.5	-0.10	V05	800–1500	H99,M01a,W04	-
125161B	9474B	-	-	$14^h16^m12\overset{s}{.}16$	$+51°22'34\overset{''}{.}7$	K1	6.32	29.8	−150.0	89.4	-	-	50–5000	M01a	?IC 2391
129333	559.1	71631	EK Dra	$14^h39^m00\overset{s}{.}21$	$+64°17'30\overset{''}{.}0$	G0 V	6.01	33.9	−138.6	−11.9	0.16	V05	20–120	M01b,W03,L06	LA (B4),m
130004	-	72146	-	$14^h45^m24\overset{s}{.}18$	$+13°50'46\overset{''}{.}7$	K0 V	5.67	19.5	−232.9	−225.7	-0.24	K02	100–5000	M01a	?LA
130322	-	72339	-	$14^h47^m32\overset{s}{.}73$	$-00°16'53\overset{''}{.}3$	K0 V	6.32	29.8	−129.6	−140.8	0.01	V05	770–2400	W04,S05	-
130948	564	72567	-	$14^h50^m15\overset{s}{.}81$	$+23°54'42\overset{''}{.}6$	G1 V	4.69	17.9	144.7	32.4	0.05	V05	50–150	W03	-
135363	-	74045	-	$15^h07^m56\overset{s}{.}26$	$+76°12'02\overset{''}{.}7$	G5	6.33	29.4	−131.9	169.3	-0.10	K02	35–100	W03,M01a,C05	IC 2391,m
139813	-	75829	-	$15^h29^m23\overset{s}{.}59$	$+80°27'01\overset{''}{.}0$	G5	5.56	21.7	−217.4	105.5	0.14	V05	50–150	W03	-
141272	3917	77408	-	$15^h48^m09\overset{s}{.}46$	$+01°34'18\overset{''}{.}3$	G8 V	5.61	21.3	−176.2	−166.7	-0.08	T05b	150–340	G98,G00,W04,L06	LA
147379B	617B	79762	EW Dra	$16^h16^m45\overset{s}{.}31$	$+67°15'22\overset{''}{.}5$	M3	6.30	10.7	−485.6	90.7	0.00	V04	100–1000	M01a, H99	?LA
-	628	80824	V2306 Oph	$16^h30^m18\overset{s}{.}06$	$-12°39'45\overset{''}{.}3$	M3.5	5.37	4.3	−93.6	−1184.9	-0.25	C01	100–5000	M01a	LA
-	-	81084	-	$16^h33^m41\overset{s}{.}61$	$-09°33'12\overset{''}{.}0$	M0.5	7.78	31.9	−67.4	−179.7	-	-	80–120	L06	LA (B4)
160934	4020A	86346	-	$17^h38^m39\overset{s}{.}63$	$+61°14'16\overset{''}{.}1$	K7	7.00	24.5	−31.2	59.4	-	-	30–50	Z04c,L06	AB Dor,m
162283	696	87322	-	$17^h50^m34\overset{s}{.}03$	$-06°03'01\overset{''}{.}0$	M0	6.70	21.9	−26.1	−131.4	-	-	100–5000	M01a, B98	-
166181	-	88848	V815 Her	$18^h08^m16\overset{s}{.}03$	$+29°41'28\overset{''}{.}1$	G6 V	5.76	32.3[e]	107.0[e]	−31.0[e]	-0.70	N04	50–150	W03	m
167605	-	89005	LP Dra	$18^h09^m55\overset{s}{.}50$	$+69°40'49\overset{''}{.}8$	K2 V	6.46	31.0	−25.3	193.9	0.13	K02	50–5000	M01a	?IC 2391,m
187748	-	97438	-	$19^h48^m15\overset{s}{.}45$	$+59°25'22\overset{''}{.}4$	G0	5.32	28.4	15.8	116.5	-0.06	N04	50–150	W03	-
-	791.3	101262	-	$20^h31^m32\overset{s}{.}07$	$+33°46'33\overset{''}{.}1$	K5 V	6.64	26.2	142.1	16.6	-	-	50–1000	M01a,H99	?IC 2391
197481	803	102409	AU Mic	$20^h45^m09\overset{s}{.}53$	$-31°20'27\overset{''}{.}2$	M0	4.83	9.9	280.4	−360.1	-	-	8–20	Z01	β Pic
201651	-	104225	-	$21^h06^m56\overset{s}{.}39$	$+69°40'28\overset{''}{.}5$	K0	6.41	32.8	109.0	66.0	-0.18	K02	50–5900	M01a,W04	?IC 2391
202575	824	105038	-	$21^h16^m32\overset{s}{.}47$	$+09°23'37\overset{''}{.}8$	K3 V	5.53	16.2	146.5	−119.1	0.04	V05	100–1000	M01a,H99	?LA
-	4199	106231	LO Peg	$21^h31^m01\overset{s}{.}71$	$+23°20'07\overset{''}{.}4$	K8	6.52	25.1	134.1	−144.8	-	-	30–50	Z04c,L06	AB Dor
206860	836.7	107350	HN Peg	$21^h44^m31\overset{s}{.}33$	$+14°46'19\overset{''}{.}0$	G0 V	4.60	18.4	231.1	−113.5	-0.02	V05	150–300	L06,G98,G00	Her-Lyr
208313	840	108156	-	$21^h54^m45\overset{s}{.}04$	$+32°19'42\overset{''}{.}9$	K0 V	5.68	20.3	210.6	−233.4	-0.04	V05	100–1000	M01a,H99	?LA

Table 4.1 — continued

Names				α	δ	Spectral	H	Dist.[a]	$\mu_\alpha \cos\delta$[a]	μ_δ[a]	[Fe/H]	[Fe/H]	Age	Age	Notes
HD	GJ	HIP	Other	(J2000)	(J2000)	Type	(mag)	(pc)	(mas/yr)	(mas/yr)		Ref.	(Myr)	Ref.	
-	-	-	V383 Lac	$22^h20^m07\overset{s}{.}03$	$+49°30'11\overset{''}{.}8$	K1 V	6.58	27.5[b]	93.4[b]	5.0[b]	-	-	50–150	W03,M01a,C05	LA
213845	863.2	111449	ups Aqr	$22^h34^m41\overset{s}{.}64$	$-20°42'29\overset{''}{.}6$	F7 V	4.27	22.7	221.6	−146.6	0.11	T05b	150–300	L06	Her-Lyr,m
-	875.1	112909	GT Peg	$22^h51^m53\overset{s}{.}54$	$+31°45'15\overset{''}{.}2$	M3	7.13	14.2	527.0	−50.6	-	-	200–300	L05,M01a	?IC 2391
-	876	113020	IL Aqr	$22^h53^m16\overset{s}{.}73$	$-14°15'49\overset{''}{.}3$	M4	5.35	4.7	960.3	−675.6	-	-	100–5000	M01a	?LA
-	9809	114066	-	$23^h06^m04\overset{s}{.}84$	$+63°55'34\overset{''}{.}4$	M0	7.17	24.9	171.0	−58.5	-	-	30–50	Z04c,L06	AB Dor
220140	-	115147	V368 Cep	$23^h19^m26\overset{s}{.}63$	$+79°00'12\overset{''}{.}7$	K1 V	5.51	19.7	201.3	71.6	-0.64	N04	50–150	M01b,W03	LA,m
221503	898A	116215	-	$23^h32^m49\overset{s}{.}40$	$-16°50'44\overset{''}{.}3$	K5	5.61	13.9	343.6	−217.7	0.00	C04	100–800	M01a,H99	?LA
-	900	116384	-	$23^h35^m00\overset{s}{.}28$	$+01°36'19\overset{''}{.}5$	K7	6.28	19.3	343.0	26.8	-0.10	C01	150–250	Z06	Ca-Near,m
-	907.1	117410	-	$23^h48^m25\overset{s}{.}69$	$-12°59'14\overset{''}{.}8$	K8	6.49	27.1	233.6	22.1	-	-	150–250	Z06	Ca-Near,m

[a]From the Hipparcos catalog (Perryman & ESA, 1997), unless stated otherwise.

[b]From Montes et al. (2001b).

[c]From the Tycho catalog (Høg et al., 1997).

[d]From the Tycho-2 catalog (Høg et al., 2000).

[e]From Fekel et al. (2005).

Note. — Star is a member of (α Per) α Persei; (AB Dor) AB Doradus; (β Pic) β Pictoris; (Ca-Near) Carina-Near; (Her-Lyr) Hercules-Lyra; (LA) Local association; (LA (B4)) Local association, subgroup B4; (U Ma) Ursa Major. If a question mark precedes the association, the membership is doubtful or based on kinematics only. An "m" indicates that the star is a multiple, see § 4.4.3 for more detail.

References. — (Z) B. Zuckerman, private communication.; (B99) Barrado y Navascués et al., 1999; (C05) Carpenter et al., 2005; (C01) Cayrel de Strobel et al., 2001; (C97) Cayrel de Strobel et al., 1997; (C04) Clem et al., 2004; (F95) Favata et al., 1995; (F98) Favata et al., 1998; (F04) Fuhrmann, 2004; (G00) Gaidos et al., 2000; (G98) Gaidos, 1998; (G01) Gerbaldi et al., 2001; (G03) Gray et al., 2003; (H98) Huensch et al., 1998; (H99) Hünsch et al., 1999; (K01) Kirkpatrick et al., 2001; (K02) Kotoneva et al., 2002; (L99) Lachaume et al., 1999; (L06) López-Santiago et al., 2006; (L05) Lowrance et al., 2005; (M06) Makarov, 2006; (M03) Mohanty & Basri, 2003; (M01a) Montes et al., 2001b; (M01b) Montes et al., 2001a; (N04) Nordström et al., 2004; (R05) Rieke et al., 2005; (S05) Saffe et al., 2005; (S04a) Santos et al., 2004; (S93) Soderblom & Mayor, 1993; (S00) Song et al., 2000; (S04b) Song et al., 2004; (S06) Sousa et al., 2006; (T05a) Takeda & Kawanomoto, 2005; (T05b) Taylor, 2005; (V04) Valdes et al., 2004; (V05) Valenti & Fischer, 2005; (W03) Wichmann et al., 2003; (W04) Wright et al., 2004; (W05) Wyatt et al., 2005; (Z01) Zuckerman et al., 2001; (Z04b) Zuckerman & Song, 2004b; (Z04a) Zuckerman & Song, 2004a; (Z04c) Zuckerman et al., 2004; (Z06) Zuckerman et al., 2006

4.3 Observations and image processing

4.3.1 Data acquisition and observing strategy

All observations were obtained at the Gemini North telescope with the Altair adaptive optics system (Herriot et al., 2000) and the NIRI camera (Hodapp et al., 2003) (programs GN-2004B-Q-14, GN-2005A-Q-16, GN-2005B-Q-4, GN-2006A-Q-5, and GN-2006B-Q-5). The $f/32$ camera was used, yielding $0.022''$ pixel^{-1} and a field of view of $22'' \times 22''$. The field lens of Altair, which improves the off-axis adaptive optics correction, was not used for any observation as it was not available for the first epoch observations. Because it introduces an undetermined field distortion, having used the field lens for the second epoch observations only would have complicated or prevented verification of the physical association of companion candidates identified in the first epoch observations. The observations were obtained in the narrow band filter CH4-short (1.54–1.65 μm), for the following reason. According to evolution models (e.g. Baraffe et al., 2003), planetary mass objects older than 10-20 Myr should have an effective temperature below 1000 K. Because of the large amounts of methane and the increased collision induced absorption by H_2 in their atmosphere, the near-infrared K-band flux of such objects is largely suppressed. It is thus more efficient to search for giant planets in either the J or the H band; the latter was preferred in this study because higher Strehl ratios are achieved at longer wavelengths. As the bulk of the H-band flux of cool giant planets is emitted in a narrow band centered at $\sim$1.58 μm because of important absorption by methane beyond 1.6 μm, it is even more efficient to search for these planets using the CH4-short filter, which is well matched to the peak of the emission. Based on evolution models and synthetic spectra of giant planets (Baraffe et al., 2003), it is expected that the mean flux density of a planet in the NIRI CH4-short filter be between 1.5 and 2.5 times higher (0.44–1.0 mag brighter) than in the broad band H filter, depending on the specific age and mass of the planet. These factors are consistent with the factors 1.6-2.0 (0.5–0.75 mag) calculated from the observed spectra of T7–T8 brown dwarfs, which

have $T_{\rm eff} \sim 800$ K.

The angular differential imaging (ADI, Marois et al., 2006) technique was used to suppress the PSF speckle noise and improve our sensitivity to faint companions. This technique consists of acquiring a sequence of many exposures of the target using an altitude/azimuth telescope with the instrument rotator turned off (at the Cassegrain focus) to keep the instrument and telescope optics aligned. This is a very stable configuration and ensures a high correlation of the sequence of PSF images. This setup also causes a rotation of the field of view (FOV) during the sequence. For each target image in such a sequence, it is possible to build a reference image from other target images in which any companion would be sufficiently displaced due to FOV rotation. After subtraction of the reference image, the residual images are rotated to align their FOV and co-added. Because of the rotation, the residual PSF speckle noise is averaged incoherently, ensuring an ever improving detection limit with increasing exposure time. It has been shown that, for ADI with Altair/NIRI, the subtraction of an optimized reference PSF image from a target image can suppress the PSF speckle noise by a factor of $\sim$12, and that a noise suppression factor of $\sim$100 is achieved for the combination of 90 such difference images (Lafrenière et al., 2007; Marois et al., 2006).

An individual exposure time of 30 seconds was chosen for all targets. This exposure time is long enough so that, at large separation, faint companion detection is limited by sky background noise rather than read noise, and short enough so that the radius of the region affected by saturation and non-linearity of the detector typically does not exceed $0.5''$. The nominal observing sequence consisted of 90 images, but oftentimes a few images had to be discarded due to brief periods of very bad seeing, loss of tracking, or the advent of clouds. No dithering was made during the main observing sequence to ensure a high correlation of the PSF images; flat-field errors, bad pixels, and cosmic ray hits are naturally averaged/removed with ADI because of the FOV rotation. The PSF centroid was found to wander over the detector by typically 2-5 pixels throughout an observing sequence because of mechanical flexure and differential refraction between

the wavefront sensing and science wavelengths; for a handful of targets the variation slightly exceeded 10 pixels. Short unsaturated exposures were acquired before and after the main sequence of (saturated) images for photometric calibration and Strehl ratio estimation; these observations were acquired in sub-array mode (256×256 or 512×512 pixels), for which the minimum exposure time is shorter. Typically, an unsaturated sequence consisted of five exposures each obtained at a different dither position. The unsaturated observations are missing for a few targets as they were either skipped in the execution of the program, or they turned out to be saturated despite using the shortest possible exposure time. Table 4.2 summarizes all observations. The last column of the table ("saturation radius") indicates the separation at which the radial profile of the PSF reaches 75% of the detector full well capacity; linearity should be better than 1% at this level (Hodapp et al., 2003). We have not analyzed the data inside this separation; point sources located at least one PSF full-width-at-half-maximum (FWHM) past this separation can be detected in our analysis, provided that their brigthness is above the detection limit.

Table 4.2. GDPS observation log

Name	Date	Number of exposures	Strehl (%)	FOV rotation (deg)	Saturation radius (″)[a]
HD 166	2005/08/25	83	5-8	55	0.98
	2006/07/18	83	7-10	81	0.78
HD 691	2005/08/10	90	13-17	70	0.43
	2006/09/18	117	16-30	88	0.44
HD 1405	2004/08/22	90	4-10	17	0.53
	2005/08/04	90	6-18	69	0.40
HD 5996	2005/08/12	90	18-20	24	0.50
	2006/09/25	90	15-17	21	0.50
HD 9540	2005/08/14	90	16-19	25	0.55
	2006/09/28	45	14-17	11	0.61
HD 10008	2005/08/10	90	18-20	36	0.51
GJ 82	2005/08/31	90	10-12	27	0.28
HD 14802	2005/08/20	90	-	23	1.09
HD 16765	2005/09/10	90	14-17	45	0.72
HD 17190	2005/08/24	90	13-30	108	0.52
HD 17382	2004/12/22	66	15	68	0.55
	2005/09/11	90	19-23	104	0.52
HD 17925	2004/11/04	83	$\gtrsim$18[b]	29	0.66
HD 18803	2004/12/24	90	7-14	99	0.70
	2005/09/12	78	17-18	108	0.64
HD 19994	2005/08/31	90	-	44	0.83
	2006/10/01	57	-	27	0.72
HD 20367	2005/10/02	90	12-14	67	0.70
2E 759	2005/10/17	59	7-10	31	0.22
HD 22049	2005/09/08	90	-	32	2.06
HIP 17695	2005/09/13	89	20-20	45	0.24
HD 25457	2005/10/02	90	-	43	0.96
HD 283750	2004/10/24	90	15	99	0.54
	2005/10/04	87	19-23	101	0.59
HD 30652	2005/09/12	52	-	35	1.86
GJ 182	2004/11/05	90	16-20	31	0.37
	2005/10/17	33	11-11	29	0.39
GJ 234A	2005/11/05	72	16	34	0.42
GJ 281	2005/03/25	67	9-10	49	0.52
	2006/02/12	25	8-9	11	0.47
GJ 285	2005/03/18	20	-	10	0.45

Table 4.2 — continued

Name	Date	Number of exposures	Strehl (%)	FOV rotation (deg)	Saturation radius (″)[a]
	2006/02/12	90	4-5	73	0.55
HD 72905	2005/04/23	84	7	25	0.87
HD 75332	2005/04/24	89	$\gtrsim$17[b]	27	0.59
	2006/12/20	16	$\gtrsim$16[b]	11	0.59
HD 77407	2005/04/26	84	16-19	33	0.61
HD 78141	2004/12/21	85	14-16	19	0.55
HD 82558	2005/04/18	90	-	30	0.61
HD 82443	2004/12/25	75	18	28	0.61
GJ 393	2005/04/20	90	13-15	44	0.55
HD 90905	2005/03/18	90	13-18	47	0.61
	2006/04/11	35	13-15	14	0.55
HD 91901	2005/04/29	71	9	22	0.44
HD 92945	2005/05/26	85	15-16	19	0.61
	2006/05/16	10	10-11	2	0.53
HD 93528	2005/04/30	86	-	26	0.39
GJ 402	2005/04/26	79	12-16	37	0.39
	2006/02/16	60	6-10	33	0.35
HD 96064	2005/04/19	89	21-23	37	0.50
	2006/03/05	90	13-19	36	0.50
HD 97334	2005/04/18	90	16-17	54	0.70
HD 102195	2005/04/24	91	20-21	54	0.41
	2006/03/18	82	12-18	30	0.39
HD 102392	2005/04/23	89	19-24	32	0.39
	2006/03/12	90	9-13	31	0.40
HD 105631	2005/05/29	90	14-19	45	0.55
HD 107146	2005/05/30	90	21-26	71	0.57
HD 108767B	2005/04/22	90	14	27	0.43
	2006/02/16	43	10-11	14	0.41
HD 109085	2005/05/26	90	-	22	1.09
	2006/03/12	15	-	3	1.09
BD+60 1417	2005/04/18	90	18-23	24	0.26
	2006/04/11	63	12	19	0.24
HD 111395	2005/04/19	89	$\gtrsim$12[b]	120	0.77
HD 113449	2005/06/01	47	10-20	37	0.52
GJ 507.1	2005/06/07	87	5-7	61	0.44
HD 116956	2005/05/29	90	5-14	27	0.55

Table 4.2 — continued

Name	Date	Number of exposures	Strehl (%)	FOV rotation (deg)	Saturation radius (″)[a]
	2006/05/16	60	5-8	18	0.61
HD 118100	2005/04/27	53	-	18	0.39
GJ 524.1	2005/04/18	90	18-25	37	0.26
	2006/05/18	90	13-14	37	0.22
HD 124106	2005/04/19	86	18-19	32	0.50
	2006/02/16	80	10-12	24	0.50
HD 125161B	2005/05/30	90	17-23	31	0.39
HD 129333	2005/04/20	90	19-20	22	0.48
HD 130004	2005/05/25	90	17-18	105	0.55
HD 130322	2005/05/27	88	15-19	40	0.48
	2006/05/15	10	10-10	5	0.40
HD 130948	2005/04/17	90	$\gtrsim 9$[b]	122	0.83
HD 135363	2005/04/18	87	14-15	19	0.48
	2006/02/16	60	8-9	14	0.44
HD 139813	2005/05/30	90	$\gtrsim 12$[b]	20	0.57
HD 141272	2005/04/19	90	18-19	47	0.55
	2006/03/12	42	13	20	0.56
HD 147379B	2005/04/18	90	17-17	22	0.50
GJ 628	2005/04/17	90	11	29	0.70
	2006/04/11	40	9-14	13	0.66
HIP 81084	2005/04/19	73	17-18	30	0.33
	2006/05/15	90	8-13	31	0.22
HD 160934	2005/04/18	84	17-24	24	0.35
	2006/09/17	14	12-14	4	0.34
HD 162283	2005/04/20	120	15-19	45	0.38
	2006/09/16	100	27-29	31	0.33
HD 166181	2005/04/17	90	16	76	0.59
	2006/09/18	45	18-21	37	0.48
HD 167605	2005/05/27	90	20	22	0.39
HD 187748	2005/05/25	97	15-19	30	0.66
	2006/09/15	75	$\gtrsim 22$[b]	21	0.50
GJ 791.3	2005/05/26	87	9-19	54	0.42
HD 197481	2005/07/29	68	6-10	21	0.87
HD 201651	2005/06/27	90	18-23	21	0.38
	2006/09/14	30	19-21	7	0.38
HD 202575	2005/07/16	90	17-23	75	0.57

Table 4.2 — continued

Name	Date	Number of exposures	Strehl (%)	FOV rotation (deg)	Saturation radius (″)[a]
	2006/09/14	30	16-18	9	0.56
GJ 4199	2004/08/23	65	10-13	118	0.44
	2005/08/04	90	15-23	136	0.39
HD 206860	2005/08/10	34	$\gtrsim$13[b]	56	0.77
	2006/06/26	60	$\gtrsim$15[b]	80	0.61
HD 208313	2005/06/27	90	23-23	67	0.46
	2006/06/25	89	14-22	66	0.55
V383 Lac	2005/07/26	66	13-17	28	0.42
	2006/06/30	77	15-18	27	0.32
HD 213845	2005/08/24	90	-	26	0.81
	2006/07/06	90	-	24	0.83
GJ 875.1	2005/08/10	90	16-18	69	0.33
	2006/07/07	79	7-17	61	0.31
GJ 876	2005/08/21	82	9-16	28	0.68
GJ 9809	2005/08/04	90	18-20	25	0.31
	2006/09/14	120	25-27	31	0.22
HD 220140	2005/08/05	90	16-18	21	0.59
	2006/07/16	82	7-9	19	0.63
HD 221503	2005/08/31	90	21-22	28	0.52
GJ 900	2004/08/24	90	15-21	17	0.46
	2005/09/08	90	16-22	46	0.42
GJ 907.1	2005/09/07	65	5-15	22	0.37
	2006/07/17	44	8	16	0.31

[a]Radius at which the PSF radial intensity profile reaches 75% of the detector well capacity.

[b]Only a lower estimate of the Strehl ratio can be obtained as the PSF peak is in the non-linear regime or sligthly saturated.

4.3.2 Data reduction

For each sequence of short unsaturated exposures, a sky frame was constructed by taking the median of the images obtained at different dither positions; this sky frame was subtracted from each image. The images were then divided by a flat field image. The PSFs of a given unsaturated sequence were registered to a common center and the median of the image sequence was obtained. The center of the PSFs were determined by fitting a 2-dimensional Gaussian function. As an indication of the quality of an observing sequence, the Strehl ratio was calculated by comparing the peak pixel value of the observed PSF image with that of an appropriate theoretical PSF. The calculated Strehl ratio values are reported in Table 4.2; two values are indicated for a target when unsaturated data were obtained before *and* after the main saturated sequence. Strehl ratios were typically in the range 10–20%.

Images of the main saturated sequence were first divided by a flat field image. Bad and hot pixels, as determined from analysis of the flat field image and dark frame respectively, were replaced by the median value of neighboring pixels. Field distortion was corrected using an IDL procedure provided by the Gemini staff (C. Trujillo, private communication) and modified to use the IDL *interpolate* function with cubic interpolation. The plate scale and field of view orientation for each image were obtained from the FITS header keywords.

For each sequence of saturated images, the stellar PSF of the first image was registered to the image center by maximizing the cross-correlation of the PSF diffraction spikes with themselves in a 180-degree rotation of the image about its center. The stellar PSF of the subsequent images was registered to the image center by maximizing the cross-correlation of the PSF diffraction spikes with those in the first image. Prior to shifting, the 1024×1024 pixel images were padded with zeros to 1450×1450 pixel to ensure that no FOV would be lost. An azimuthally symmetric intensity profile was finally subtracted from each image to remove the smooth seeing halo.

Next, the stellar PSF speckles were removed from each image by subtracting an optimized reference PSF image obtained using the "locally optimized combination of images" (LOCI) algorithm detailed in Lafrenière et al. (2007). The heart of this algorithm consists in dividing the target image into subsections and obtaining, for each subsection independently, an optimized reference PSF image consisting of a linear combination of the other images of the sequence for which the rotation of the FOV would have displaced sufficiently an eventual companion. For each subsection, the coefficients of the linear combination are optimized such that its subtraction from the target image minimizes the noise. The subsections geometry and the algorithm parameters determined in Lafrenière et al. (2007) were used for all targets. The residual images were then rotated to align their FOV and their median was obtained. Figure 4.2 illustrates the PSF subtraction process.

4.3.3 Photometric calibration and uncertainty

As the stellar PSF peak is saturated for the main sequence of images, and since much image processing is done to subtract the stellar PSF from each image, special care must be taken to calibrate the photometry of the residual images and ensure that the contrast limits calculated are accurate.

When the PSF peak is saturated, relative photometry can be calibrated by scaling the stellar flux measured in the unsaturated images obtained before and/or after the saturated sequence according to the ratio of the exposure times of the saturated and unsaturated images. However, the accuracy of this calibration method is affected by the (unknown) variations in Strehl ratio, hence of the peak PSF flux, that may have occurred between the saturated and unsaturated observations. To mitigate this problem, the calibration approach we adopted relies on a sharp ghost artifact located $(+0.09'', -2.45'')$ from the PSF center in the ALTAIR/NIRI images. Since the intensity of this ghost artifact is proportional to the PSF intensity, it can be used to infer the peak flux of a saturated PSF. This was verified for all sequences for which both unsaturated and saturated data

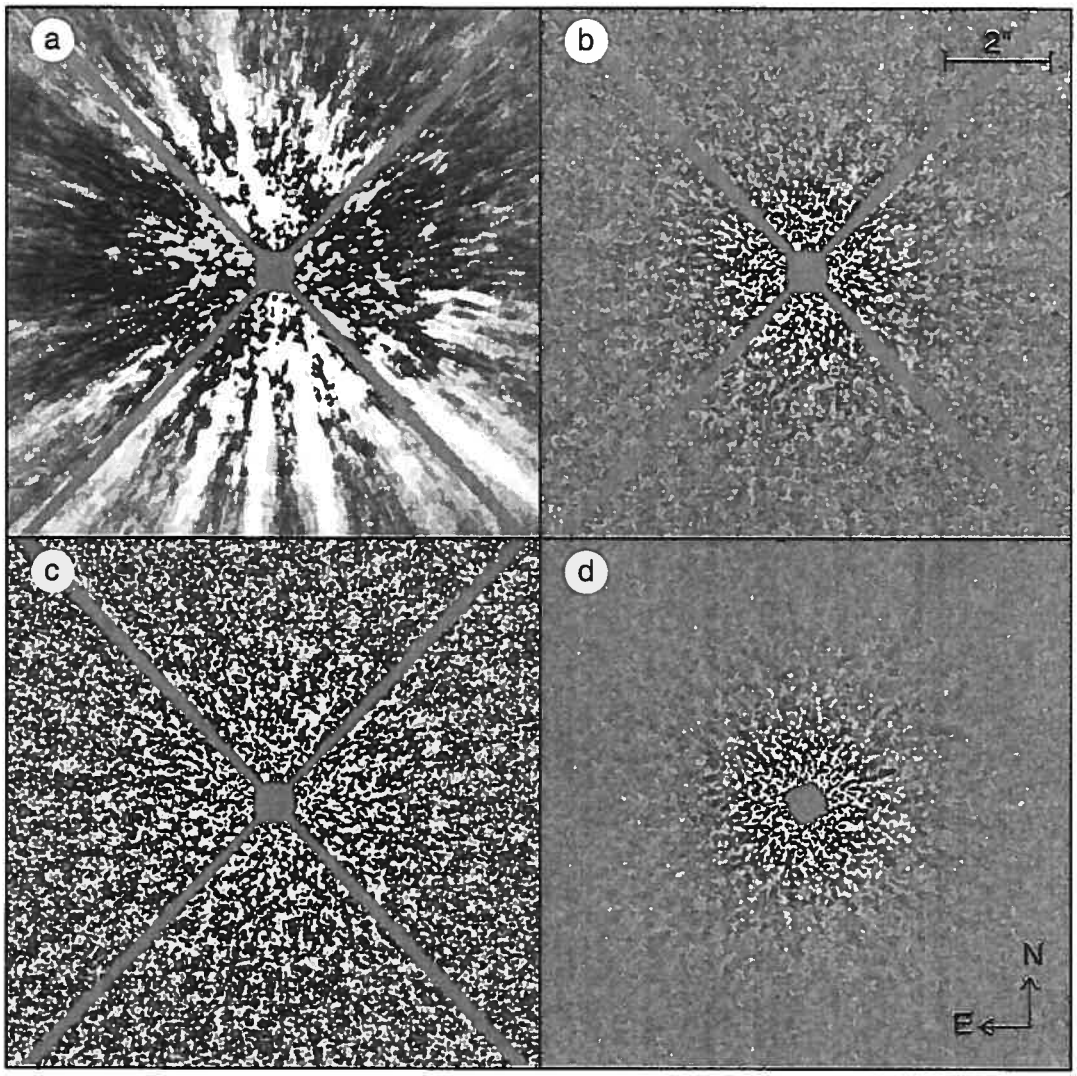

Figure 4.2 Illustration of the ADI noise attenuation process. Panel (a) shows an original 30-s image of the young star HD 691 after subtraction of an azimuthally symmetric median intensity profile, panels (b) and (c) both show, with a different intensity scale, the corresponding residual image after ADI subtraction using the LOCI algorithm, and panel (d) shows the median combination of 117 such residual images. Display intensity ranges are $\pm 5 \times 10^{-6}$ and $\pm 10^{-6}$ of stellar PSF peak for the top and bottom rows respectively. Each panel is $10''$ on a side. The diffraction spikes from the secondary mirror support vanes and the central saturated region are masked. The faint point source ($\Delta m = 14.9$) visible in panel (d) at a separation of $2.43''$ and P.A. of $7.3°$ could not have been detected without ADI processing.

were available. First, the stellar flux was measured in the unsaturated images using a circular aperture of diameter equal to the FWHM of the PSF. When unsaturated data were acquired both before and after the saturated sequence, the mean of the two values was used. Then the flux of the ghost artifact in the same aperture was measured for each image of the saturated sequence. The median of these values, scaled according to the ratio of the exposure times of the saturated and unsaturated images, was then compared to the stellar flux, and the process was repeated for all sequences that include both saturated and unsaturated data. Similar values were found for all sequences; the mean ratio of the flux of the ghost over that of the PSF peak was found to be 6.1×10^{-5}, with a standard deviation of 0.6×10^{-5}. Comparisons of the flux of background stars bright enough to be visible in each individual image of a sequence with the flux of the ghost in the corresponding images also confirmed that the intensity of the ghost is indeed directly proportional to the intensity of off-axis sources.

The procedure used for calibrating the photometry was the following. The flux of the ghost was measured for each image of a sequence and the median of these values, divided by the ratio quoted above, was taken to represent the peak stellar PSF flux, $F_\star$. This calibration method should be more accurate than the one based solely on unsaturated data obtained before and/or after the saturated sequence because the median ghost flux is affected in the same way as the median of all residual images by the variations of Strehl ratio that may have occurred during the sequence of saturated images or between the saturated and unsaturated measurements. For this reason, this calibration was used even for the sequences for which unsaturated data were available.

Observations obtained with ALTAIR without the field lens suffer from important off-axis Strehl degradation because of anisoplanatism; this degradation must be taken into account when calculating contrast. Unfortunately, it is virtually impossible to quantify the specific degradation pertaining to our data as there are no bright reference off-axis point sources available for every sequence of images. Instead, we have used the average

anisoplanetism Strehl ratio degradation formula indicated on the ALTAIR webpage[4], which is $f_{\text{aniso}}(\theta) \equiv S(\theta)/S_0 = \mathrm{e}^{-(\theta/12.5)^2}$, where $S(\theta)$ is the Strehl ratio at angular separation θ, expressed in arcseconds, and S_0 is the on-axis Strehl ratio. This factor was used to correct the noise and the flux of faint point sources measured in the residual images.

As explained in Lafrenière et al. (2007), while the subtraction of an optimized reference PSF obtained using the LOCI algorithm leads to better signal-to-noise (S/N) ratios, it removes partially the flux of the point sources sought after. This flux loss must be accounted for when calculating contrast. This is done by calculating the normalized residual intensity, f_{sub}, of artificially implanted point sources after execution of the subtraction algorithm; the method used is described in §4.3 of Lafrenière et al. (2007). Then using flux measurements made in the residual image, the factor f_{sub} is used to infer the true flux of a point source, i.e. that before execution of the subtraction algorithm.

Another effect that must be taken into account for ADI data is the azimuthal smearing of an off-axis point source that occurs as the field of view rotates during an integration; this causes a fraction of the source's flux to fall outside of the circular aperture used for photometric measurements. The amount of flux loss in the aperture was calculated for each sequence of images as follows. For a given angular separation and for each image of a sequence, a copy of the unsaturated PSF was smeared according to its displacement during an integration. When unsaturated data were unavailable, a 2D Gaussian of the appropriate FWHM was used in place of the unsaturated PSF. The median of these smeared PSFs was obtained and the flux in a circular aperture was measured. This flux was divided by the flux of the original PSF in the same aperture to obtain the smearing factor f_{sm}, which is used to correct the flux or noise measured in the images.

Given all of these considerations, the contrast at angular separation θ was calculated as

$$C(\theta) = \frac{F(\theta)}{f_{\text{aniso}}(\theta) f_{\text{sm}}(\theta) f_{\text{sub}}(\theta)} \times \frac{1}{F_\star}, \tag{4.1}$$

[4]http://www.gemini.edu/sciops/instruments/altair/altairCommissioningPerformance.html

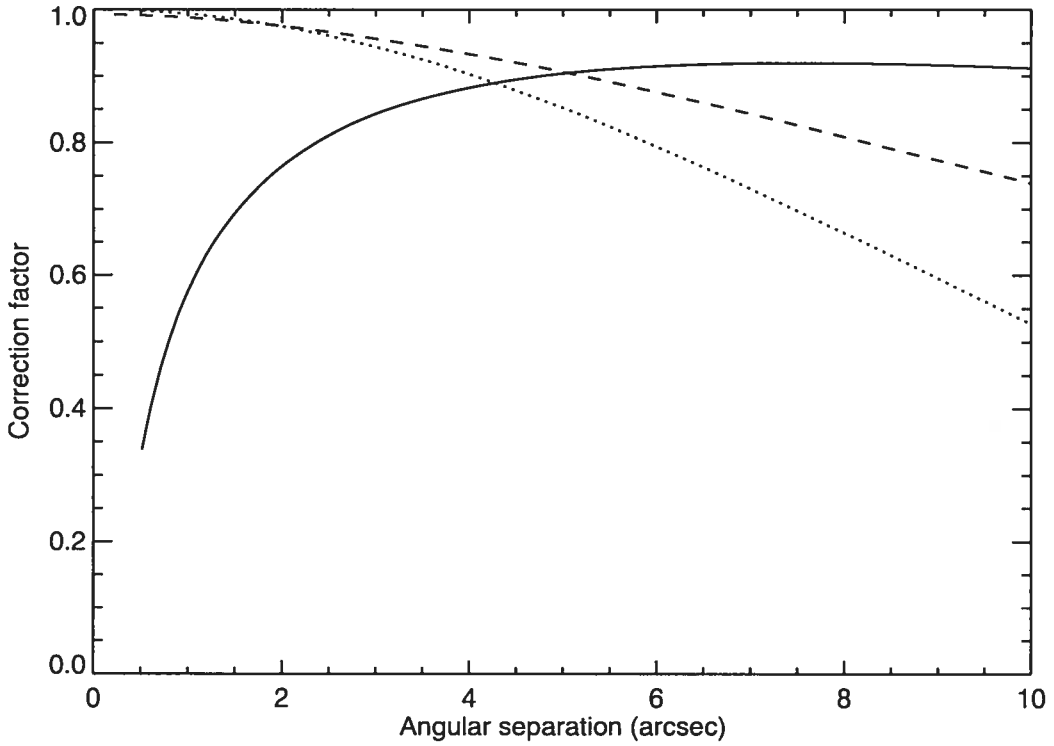

Figure 4.3 Typical values of $f_{\rm sub}$ (*solid line*), $f_{\rm aniso}$ (*dotted line*), and $f_{\rm sm}$ (*dashed line*) as a function of angular separation. The curves shown are for the target HD 166181.

where $F(\theta)$ is either the noise or the flux of a point source in a circular aperture of diameter equal to one PSF FWHM, at angular separation θ, in the residual image. Note that the contrast in the equation above is defined such that a fainter companion, or a smaller residual noise, has a smaller contrast value. Eq. (4.1) was used for all contrast calculations in the present work. Typical correction factors as a function of angular separation are shown in Figure 4.3.

An estimate of the photometric accuracy resulting from the entire process was obtained by calculating the mean absolute difference between the magnitudes calculated at two epochs for every faint background star that was observed twice (see §4.4.2); this mean absolute difference was taken to represent $\sqrt{2}$ times the photometric uncertainty. This photometric uncertainty was found to vary significantly with angular separation,

Table 4.3. Photometric uncertainties

Sep. ($''$)	<4	$4-7$	$7-10$	$10-13$	>13
σ (mag)	0.07	0.12	0.15	0.26	0.39

indicating that it is dominated by the uncertainty on the anisoplanatism factor. The photometric uncertainty as a function of angular separation is reported in Table 4.3; it is typically 0.07–0.15 mag for separations below $10''$. For completeness, it is noted that a higher photometric uncertainty, by about 0.08 mag, results when the unsaturated data obtained before and/or after the main sequence of saturated images are used to determine $F_\star$, rather than the median flux of the ghost artifact, justifying our choice to use the calibration based on the flux of the ghost for all sequences.

4.4 Results

4.4.1 Detection limits

Detection limits are based on a measure of the noise in the residual images. To calculate this noise, the residual images were first convolved by a circular aperture of diameter equal to one PSF FWHM, which is typically $\sim 0.07''$, and the noise as a function of angular separation from the image center, $F(\theta)$, was determined as the standard deviation of the pixel values in an annulus of width equal to one PSF FWHM. As shown in Lafrenière et al. (2007) and Marois et al. (2007b), the noise in an ADI residual image has a distribution similar to a Gaussian; using a 5σ detection threshold is thus appropriate for our data to limit the number of false positives. Given that a residual image typically contains $\sim 2\times 10^5$ resolution elements, roughly 0.1 false positive per target is expected on average. Because of the underlying noise in a residual image, some sources near the detection threshold might not be detected. From Gaussian statistics, the probability that the residual signal underlying a source is below 0σ, -1σ, or -2σ is 50%, 16%,

or 2.3%, respectively. Our detection completeness for sources whose true intensities are 5σ, 6σ, or $>7\sigma$ is thus 50%, 84%, or >97.7%, respectively. Note that for a similar reason, some sources whose true intensities are below the 5σ threshold could be detected as well. These effects will be taken into account appropriately in the statistical analysis of the results presented in §4.5.

The detection limits achieved for all target stars, expressed in magnitude difference, are presented in Table 4.4. The last two lines of this table present the median and best contrast, over the 85 observations, achieved at each angular separation. The median detection limits in magnitude difference are 9.5 at 0.5″, 12.9 at 1″, 15.0 at 2″, and 16.5 at 5″. The detection limits are presented graphically in Figure 4.4 for the stars HD 208313, HD 166181, and GJ 507.1, which are representative of poor, median, and good contrast performance, respectively.

Table 4.4. GDPS detection limits[a]

Name	0.50″	0.60″	0.75″	1.00″	1.25″	1.50″	2.00″	2.50″	3.00″	4.00″	5.00″	7.50″	10.00″
HD 166	-	-	-	12.5	13.1	13.9	14.9	15.4	15.9	16.5	16.9	17.3	17.3
HD 691	-	11.1	12.1	13.2	14.1	14.7	15.6	15.9	16.2	16.6	16.7	16.6	16.3
HD 1405	9.2	10.5	11.4	12.7	13.5	14.0	14.8	15.3	15.7	16.0	16.1	16.1	15.8
HD 5996	-	10.8	12.0	13.2	14.1	14.6	15.4	15.8	16.1	16.5	16.6	16.6	16.4
HD 9540	-	-	11.8	13.1	14.0	14.5	15.4	16.0	16.4	17.0	17.3	17.6	17.5
HD 10008	-	10.0	11.2	12.4	13.2	13.8	14.7	15.2	15.6	16.2	16.5	16.5	16.3
GJ 82	8.9	9.5	10.5	11.8	12.5	13.2	13.7	14.3	14.6	14.9	15.0	14.8	14.6
HD 14802	-	-	-	-	11.8	12.4	13.3	14.0	14.7	15.8	16.8	17.4	17.9
HD 16765	-	-	-	13.0	13.9	14.5	15.3	15.8	16.2	16.9	17.4	17.5	17.6
HD 17190	-	10.5	12.2	13.7	14.2	14.8	15.5	15.9	16.3	16.6	16.8	16.6	16.2
HD 17382	-	10.8	12.0	13.3	14.1	14.6	15.4	15.9	16.3	16.8	17.0	17.0	16.7
HD 17925	-	-	11.9	13.6	14.6	15.4	16.2	16.8	17.1	17.6	17.7	17.7	17.4
HD 18803	-	-	11.3	12.9	13.8	14.5	15.5	16.0	16.5	16.8	17.1	17.2	16.9
HD 19994	-	-	-	13.5	14.3	15.0	15.8	16.4	16.7	17.4	17.8	18.3	18.4
HD 20367	-	-	-	11.6	12.2	12.8	13.9	14.4	14.8	15.6	16.0	16.3	16.1
2E 759	8.6	9.4	9.9	11.0	11.8	12.2	13.0	13.4	13.6	13.9	14.0	13.9	13.6
HD 22049	-	-	-	-	-	-	-	15.9	16.5	17.3	17.7	18.5	18.9
HIP 17695	10.0	10.8	11.8	12.8	13.6	14.2	14.8	15.1	15.3	15.7	15.7	15.6	15.3
HD 25457	-	-	-	-	12.5	13.1	13.9	14.8	15.2	16.0	16.6	17.0	17.0
HD 283750	-	-	12.2	13.4	14.2	15.1	15.9	16.4	16.8	17.2	17.2	17.1	16.7
HD 30652	-	-	-	-	-	-	14.9	15.5	15.9	16.7	17.3	18.2	18.6
GJ 182	10.0	10.5	11.9	13.1	14.0	14.7	15.4	15.8	16.1	16.4	16.5	16.4	16.2
GJ 234A	9.5	10.1	11.2	12.3	13.3	13.9	14.6	15.1	15.4	15.9	16.2	16.3	16.1
GJ 281	-	9.0	10.4	12.0	12.9	13.5	14.3	14.6	15.0	15.3	15.3	15.4	15.2
GJ 285	-	8.0	10.1	11.6	12.6	13.3	13.8	14.5	14.9	15.5	15.8	15.9	15.8
HD 72905	-	-	-	11.2	12.5	13.1	14.2	14.9	15.4	16.3	16.7	17.4	17.7
HD 75332	-	-	10.8	12.3	13.0	13.9	14.9	15.5	15.7	16.6	17.1	17.4	17.3
HD 77407	-	-	10.3	11.4	12.3	13.0	14.0	14.8	15.0	15.7	16.0	16.3	16.2
HD 78141	-	-	11.5	13.0	13.7	14.5	15.4	15.8	16.1	16.5	16.6	16.5	16.3
HD 82558	-	-	11.5	12.9	13.8	14.4	15.4	15.9	16.1	16.6	16.8	17.0	16.7
HD 82443	-	-	11.5	13.0	14.1	14.8	15.9	16.4	16.8	17.2	17.5	17.7	17.5
GJ 393	-	-	11.8	13.3	14.1	14.6	15.6	16.0	16.2	16.7	16.8	16.9	16.8
HD 90905	-	-	11.4	12.7	13.7	14.1	15.1	15.7	16.1	16.5	16.6	16.6	16.4
HD 91901	-	9.2	10.0	11.4	12.1	12.8	13.6	14.1	14.4	14.9	14.8	14.8	14.6
HD 92945	-	-	10.8	12.1	13.0	13.8	14.6	15.1	15.5	15.9	16.1	16.3	16.1
HD 93528	8.5	9.3	10.2	11.6	12.6	13.3	14.2	14.8	15.0	15.5	15.7	15.9	15.7
GJ 402	8.4	9.2	10.5	11.6	12.5	13.1	14.0	14.5	14.9	15.4	15.4	15.6	15.3
HD 96064	-	10.9	12.3	13.5	14.3	14.9	15.6	16.1	16.3	16.6	16.8	16.8	16.6
HD 97334	-	-	-	13.6	14.7	15.1	16.0	16.4	16.7	17.2	17.4	17.5	17.3
HD 102195	9.8	11.2	12.2	13.3	14.1	14.7	15.4	15.9	16.1	16.5	16.6	16.6	16.3
HD 102392	9.5	10.3	11.4	12.6	13.5	13.9	14.7	15.3	15.6	16.1	16.3	16.3	16.2
HD 105631	-	-	11.7	12.8	13.5	14.2	15.1	15.5	16.0	16.4	16.7	16.8	16.5
HD 107146	-	-	11.7	12.5	13.5	14.0	15.0	15.4	15.8	16.2	16.5	16.5	16.3
HD 108767B	8.4	9.7	10.6	11.9	12.8	13.5	14.3	14.9	15.1	15.7	15.8	16.0	15.7
HD 109085	-	-	-	-	13.4	14.0	14.9	15.8	16.3	17.2	17.7	18.3	18.5
BD+60 1417	10.0	11.1	12.0	13.0	13.8	14.2	14.7	15.0	15.3	15.5	15.5	15.4	15.1
HD 111395	-	-	-	13.4	14.3	15.0	15.9	16.4	16.7	17.2	17.4	17.6	17.3
HD 113449	-	-	11.5	12.6	13.7	13.9	14.9	15.4	15.7	16.3	16.5	16.6	16.4
GJ 507.1	-	9.6	10.4	11.5	12.2	12.9	13.7	14.3	14.6	15.0	15.2	15.2	14.9
HD 116956	-	-	11.3	12.7	13.5	14.2	15.1	15.7	16.0	16.5	16.7	16.8	16.6
HD 118100	8.4	9.4	10.5	11.6	12.3	12.8	13.5	14.0	14.1	14.4	14.5	14.4	14.2
GJ 524.1	10.1	11.0	12.0	13.0	13.6	14.2	14.9	15.2	15.4	15.4	15.5	15.4	15.0
HD 124106	-	10.3	11.6	13.0	13.8	14.4	15.4	15.7	15.9	16.4	16.7	16.8	16.6
HD 125161B	10.5	11.3	12.4	13.6	14.3	14.6	15.4	15.8	16.0	16.2	16.4	16.3	16.1
HD 129333	-	10.7	11.7	13.2	13.9	14.4	15.3	15.7	16.2	16.4	16.7	16.7	16.5
HD 130004	-	-	12.0	13.1	14.1	14.5	15.3	15.8	16.1	16.5	16.7	16.7	16.4
HD 130322	-	11.1	12.1	13.2	13.9	14.3	15.2	15.6	15.9	16.3	16.4	16.4	16.2
HD 130948	-	-	-	12.4	13.2	13.8	14.7	15.4	15.7	16.5	16.9	17.3	17.3
HD 135363	-	9.2	10.9	12.3	13.1	13.7	14.6	15.1	15.3	15.5	15.7	15.6	15.4
HD 139813	-	-	10.3	11.2	11.9	12.6	13.6	14.3	14.9	15.7	16.1	16.3	16.1
HD 141272	-	-	12.2	13.7	14.4	15.0	15.8	16.2	16.5	16.9	16.9	17.1	16.9
HD 147379B	-	10.0	11.3	12.8	13.5	14.1	15.0	15.3	15.6	15.8	16.0	16.0	15.7
GJ 628	-	-	10.4	12.2	13.0	13.7	14.6	15.2	15.7	16.2	16.6	16.9	16.7
HIP 81084	9.5	10.3	11.4	12.3	13.0	13.5	14.0	14.4	14.6	14.7	14.7	14.6	14.3
HD 160934	9.5	10.1	11.2	12.5	13.3	13.9	14.6	14.9	15.0	15.3	15.3	15.2	14.9
HD 162283	10.3	11.2	12.2	13.4	14.0	14.6	15.2	15.7	16.1	16.4	16.5	16.5	16.1
HD 166181	-	10.8	11.7	13.0	13.7	14.3	15.0	15.4	15.8	16.2	16.5	16.5	16.3
HD 167605	9.4	10.5	11.4	12.5	13.3	14.0	14.8	15.1	15.6	15.9	16.1	16.1	15.9
HD 187748	-	10.8	11.7	12.9	13.7	14.5	15.3	15.9	16.3	17.0	17.3	17.6	17.4
GJ 791.3	9.6	11.0	12.0	13.3	13.8	14.4	15.1	15.6	15.7	16.0	16.1	16.1	15.7
HD 197481	-	-	-	11.0	11.7	12.4	13.5	14.3	14.7	15.5	16.1	16.4	16.3
HD 201651	10.1	11.4	12.3	13.3	14.1	14.6	15.3	15.8	16.1	16.4	16.5	16.5	16.3
HD 202575	-	-	11.4	12.5	13.3	14.0	14.9	15.5	16.1	16.6	16.8	17.0	16.7
GJ 4199	10.5	11.2	12.0	13.2	13.8	14.5	15.1	15.6	15.7	16.0	16.1	15.8	15.4

Table 4.4 — continued

Name	0.50″	0.60″	0.75″	1.00″	1.25″	1.50″	2.00″	2.50″	3.00″	4.00″	5.00″	7.50″	10.00″
HD 206860	-	-	12.2	13.3	13.8	14.5	15.2	15.7	16.0	16.5	16.9	17.0	16.7
HD 208313	-	11.9	13.0	14.0	14.7	15.2	16.0	16.5	16.7	17.2	17.3	17.3	17.0
V383 Lac	10.2	11.0	11.9	13.0	13.6	14.3	14.8	15.2	15.5	15.9	16.1	16.0	15.8
HD 213845	-	-	-	13.3	14.0	14.7	15.7	16.3	16.8	17.2	17.6	18.1	18.0
GJ 875.1	9.6	10.5	11.2	12.3	13.1	13.5	14.4	14.9	15.1	15.5	15.6	15.5	15.1
GJ 876	-	-	-	11.0	12.2	12.6	13.7	14.3	15.1	15.8	16.2	16.6	16.6
GJ 9809	11.3	12.1	12.8	14.0	14.6	15.0	15.5	15.9	15.9	16.2	16.3	16.1	15.8
HD 220140	-	-	12.0	13.1	13.9	14.5	15.3	15.8	16.1	16.4	16.6	16.5	16.3
HD 221503	-	10.4	11.8	13.2	14.1	14.6	15.3	15.8	16.2	16.7	17.0	17.1	17.0
GJ 900	8.9	10.1	10.8	12.4	13.2	13.9	14.9	15.4	15.8	16.1	16.2	16.1	16.0
GJ 907.1	8.4	9.0	10.0	11.2	12.1	12.5	13.4	14.0	14.3	14.8	15.0	15.1	14.9
Median	9.5	10.5	11.5	12.9	13.6	14.2	15.0	15.5	15.8	16.3	16.5	16.5	16.3
Best	11.3	12.1	13.0	14.0	14.7	15.4	16.2	16.8	17.1	17.6	17.8	18.5	18.9

[a]Magnitude difference in the NIRI CH4-short filter, at a 5σ level.

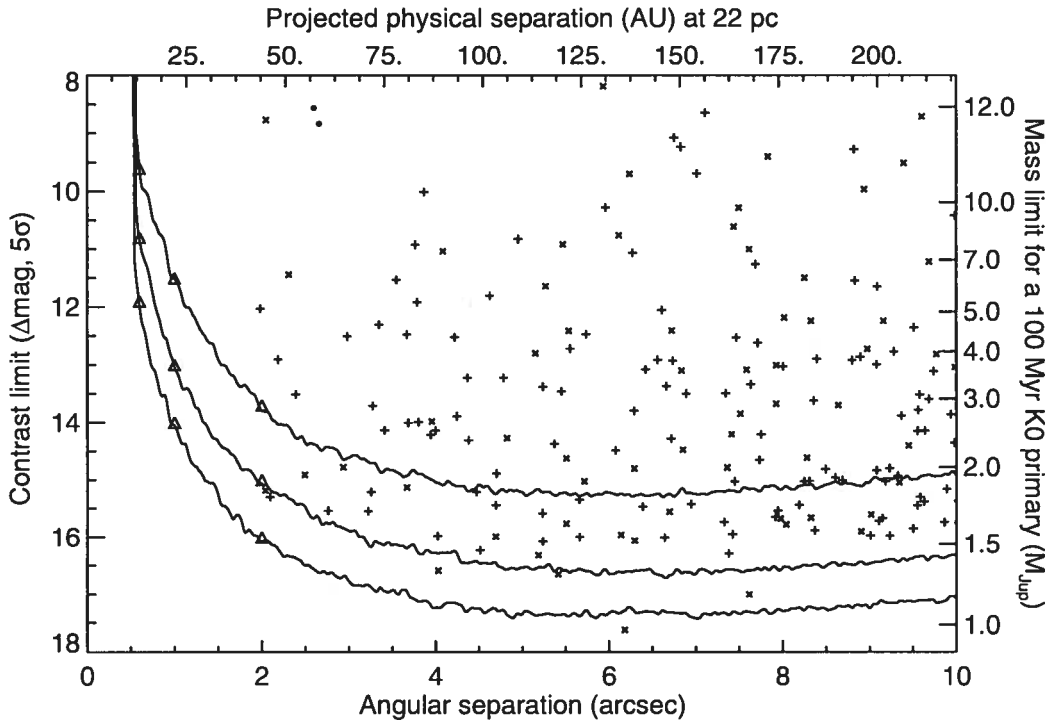

Figure 4.4 Survey detection limits in difference of magnitude (in the NIRI CH4-short filter) between an off-axis point source and the target star, at the 6σ level. The top, middle, and bottom curves are respectively for the targets GJ 507.1, HD 166181, and HD 208313, which are representative of poor, median, and good performance reached by the survey. Companion candidates identified around targets of galactic latitude $|b| < 15$ are shown by $+$ symbols, while those identified around targets with $|b| \geq 15$ are shown by $\times$ symbols. The two filled circles near (2.6,8.6) indicate the components of the binary brown dwarf companion to HD 130948. The fiducial point sources shown in Fig. 4.5 are marked with triangles. The top and right axes show, for reference only, the projected separation in AU and the detection limits in $M_{\rm Jup}$ that would apply for a 100 Myr old K0 star located 22 pc away.

For consistency we have verified the validity of these detection limits by implanting fiducial sources in the sequence of original images and then processing the data as described in §4.3.2. An example, incorporating artificial sources at the 5σ and 10σ levels at various separations, is shown in Figure 4.5 for the stars HD 208313, HD 166181, and GJ 507.1. As visible in this figure, sources exactly at our detection limits can indeed be detected with the expected completeness level.

One must resort to evolution models of giant planets to convert the detection limits mentioned above into mass limits. Traditionally, such evolution models have assumed arbitrary initial conditions for the planets (e.g. Baraffe et al., 2003; Burrows et al., 1997), with the caution that their results depend on the specific initial conditions adopted for ages below a few million years (Baraffe et al., 2002). Recent evolution models (Marley et al., 2007) that incorporate initial conditions calculated explicitly for planets formed through core accretion indicate that it may in fact take as much as 10–100 Myr before the planets "forget" their initial conditions; the effect being more important for more massive planets. Nevertheless, given the typical ages of our target stars (50–300 Myr) and the good contrast limits we have reached, the different evolution models should yield similar mass detection limit estimates. As a simple example, consider a contrast of 12.9 mag in the NIRI CH4-short filter around a K0 star (typical at a separation of $1''$). The "hot start" models of Baraffe et al. (2003) would give masses of 2.6 $M_{\rm Jup}$ and 3.9 $M_{\rm Jup}$ at 50 Myr and 100 Myr, respectively, while the "core accretion" models of Marley et al. (2007) would give masses of $\sim$3.0 $M_{\rm Jup}$ and $\sim$4.5 $M_{\rm Jup}$, respectively[5]. The difference between the models would be smaller for smaller masses (better contrast limits (i.e. beyond $\sim1''$) and/or greater ages), while it would be larger for larger masses (worse contrast limits and/or smaller ages). In this work, keeping the latter caveat in mind, we have used the COND evolution models of Baraffe et al. (2003), for which absolute H-band magnitudes as a function of mass and age are readily available. The following procedure

[5]For this simple calculation, it was assumed that the luminosity ratios between the "hot start" and "core accretion" models were representative of the H-band magnitude differences.

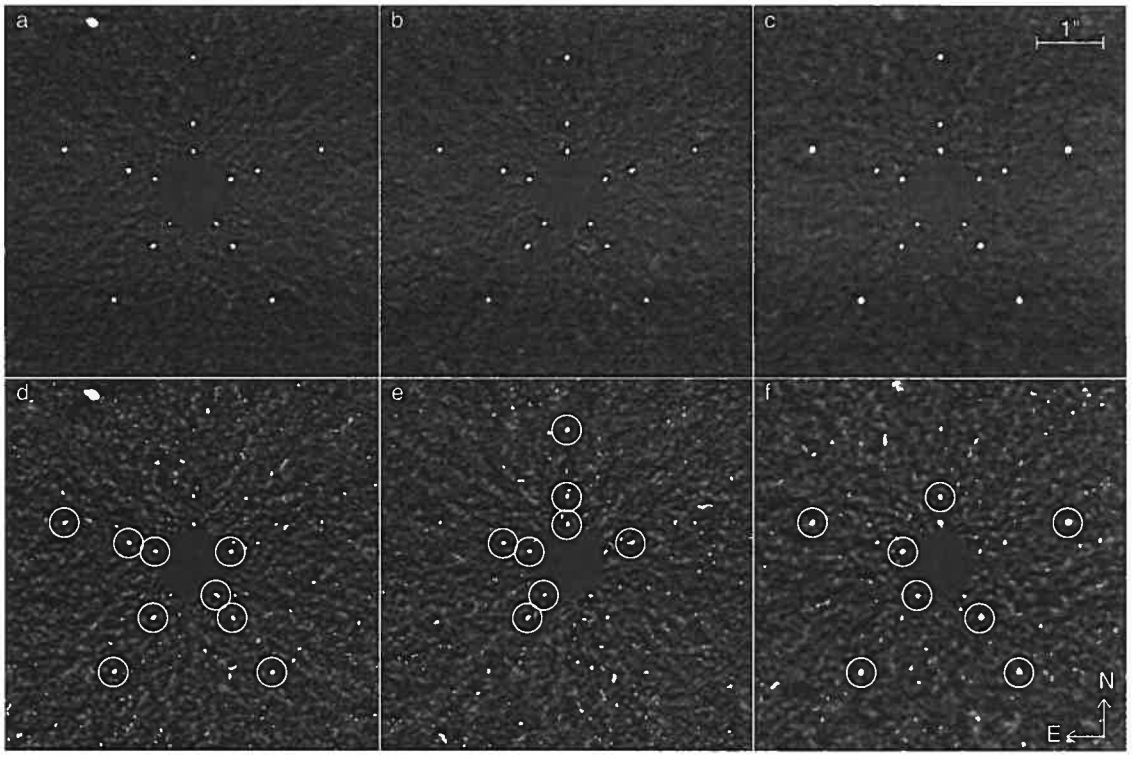

Figure 4.5 Final S/N residual images for three sequences of images to which fiducial point sources have been implanted. The fiducial point sources have been added at 5 P.A.'s (0°, 72°, 144°, 216°, and 288°) and 3 angular separations (0.6″, 1.0″, and 2.0″). For bottom panels (d–f) the intensity of each source was set to the corresponding detection limit (5σ) indicated in Table 4.4, while it was set 0.75 mag brighter (i.e. 10σ) for top panels (a–c). Panels (a,d), (b,e), and (c,f) are for the stars HD 208313, HD 166181, and GJ 507.1, respectively. The bright spot at the upper left corner of panels (a,d) is a real background star. The display intensity scale is linear from -2 to $+10$ for top panels (a–c), and from -1 to $+5$ for bottom panels (d–f). In bottom panels (d–f), the sources that would have been detected (S/N$\geq$5) have been circled in white. According to expectations, the detection completeness is roughly 50% for sources whose true intensity is equal to the 5σ detection limit.

was used to estimate the contrast, in the NIRI CH4-short filter, of a planet of given mass orbiting a given target. The absolute H-band magnitude of the planet was first obtained directly from the evolution models of Baraffe et al. (2003) and converted into an apparent magnitude, $H_{\rm pl}$, using the distance of the star. The corresponding magnitude in the NIRI CH4-short filter was then calculated as

$$m_{\rm pl} = H_{\rm pl} - 2.5 \log \left(\frac{f_{\rm CH4}}{f_H} \right), \tag{4.2}$$

where $f_{\rm CH4}$ and f_H are the mean flux density of the planet in the NIRI CH4-short and broad band H filters, respectively; their values were calculated using a synthetic spectrum of appropriate effective temperature and surface gravity (Baraffe et al., 2003; Allard et al., 2001)[6]. We recall here (c.f. §4.3) that the ratio $\frac{f_{\rm CH4}}{f_H}$ is typically 1.5–2.5 for giant planets depending on their mass and age. The stellar magnitudes in the NIRI CH4-short and broad band H filters were assumed to be equal, such that the contrast of the planet was obtained as $m_{\rm pl} - H_\star$, where $H_\star$ is the H-band apparent magnitude of the target star. The 5σ contrast levels of planets of various masses orbiting a K0 primary of 100 Myr,[7] the typical target of the survey, are presented in Figure 4.4. For a typical target located at 22 pc from the Sun, the median detection limits correspond to 10.8 $M_{\rm Jup}$ at 11 AU, 3.9 $M_{\rm Jup}$ at 22 AU, 1.9 $M_{\rm Jup}$ at 44 AU, and 1.4 $M_{\rm Jup}$ at 110 AU.

The typical contrast reached by our survey improves on earlier surveys (e.g. Lowrance et al., 2005; Masciadri et al., 2005; Chauvin et al., 2006; Biller et al., 2007) by at least 1 mag at $1''$, 1.5 mag at $2''$, and ~ 3 mag at larger separations. For the 27 targets for which our data were in the linear regime of the detector at a separation of $0.5''$, our detection limits at this separation are similar to those achieved with the SDI device at the Very Large Telescope (Biller et al., 2007). The contrast reached by GDPS observations is the highest that has been achieved to date at separations larger than $\sim 0.7''$.

[6] Spectra available at ftp://ftp.ens-lyon.fr/pub/users/CRAL/fallard/

[7] An H-band absolute magnitude of 4.0 was used, this is the mean value of the K0 stars in the sample.

4.4.2 Candidate companion detections

To identify candidate companions, the residual images were first convolved by a circular aperture of diameter equal to one PSF FWHM, and then converted to signal-to-noise (S/N) images that were visually inspected for point sources at a $\gtrsim 5\sigma$ level. After identification of a point source, its position was measured by fitting a 2D Gaussian function, and its flux was measured in an aperture of diameter equal to one PSF FWHM; both operations were done in the non-convolved residual image. The contrast of the point source was then calculated using Eq.(4.1). More than 300 faint point sources were found around 54 targets, 188 of which are found around only 7 stars located at low galactic latitudes ($b < 11°$). Up to now, all but six of the 54 stars with candidates were re-observed at a subsequent epoch to verify whether or not the faint point sources detected are co-moving with the target star.

All candidate exoplanets observed at two epochs have been confirmed to be background sources by comparing their displacement between the two epochs with the expected displacement of a distant background source, based on the proper motion and parallax of the target; an example of this verification is presented in Figure 4.6. As a reference for future planet searches, a compilation of all faint point sources identified around our target stars is presented in Table 4.5.

An estimate of the uncertainties on the measured separations and P.A. was obtained by calculating the mean absolute difference between the separation and P.A. measured at the second epoch and those predicted for this epoch based on the parallax and proper motion of the target stars. Given the high precision on the parallax and proper motion of the target stars, the differences observed are dominated by our measurement uncertainties. The mean absolute differences calculated are taken to represent $\sqrt{2}$ times the uncertainties; values of $\sigma_{\rm sep} = 0.015''$ and $\sigma_{\rm P.A.} = 0.2°$ are found.

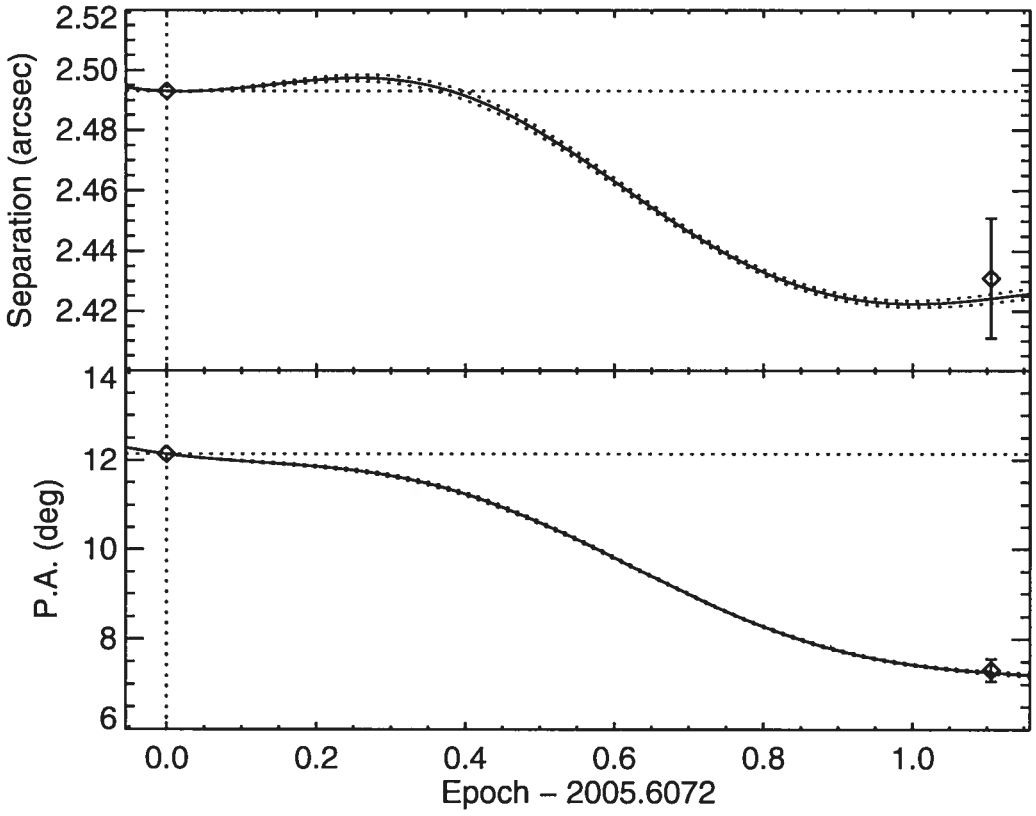

Figure 4.6 Verification of the background nature of the point source detected around the young star HD 691. Open diamonds mark the observed separation (*top*) and P.A. (*bottom*) of the point source at the two epochs. The solid line indicates the expected separation and P.A. of a distant background source as a function of time. The observations agree very well with the expected motion of a background source, indicating that the source is not associated with HD 691.

Table 4.5. Point sources detected

Star	Epoch	Separation[a] (arcsec)	P.A.[b] (deg)	Δm[c] mag
HD 166	2005.6482	10.23	82.9	12.60
HD 691	2005.6072	2.49	12.1	14.91
HD 1405	2004.6409	3.95	254.0	13.98
HD 5996	2005.6128	2.98	118.6	12.51
	2005.6128	4.78	71.6	13.23
	2005.6128	5.66	268.9	15.99
	2005.6128	6.95	73.9	15.43
	2005.6128	9.11	280.8	15.72[e]
	2005.6128	9.15	228.1	15.67
	2005.6128	9.50	120.6	15.85[e]
	2005.6128	9.58	205.2	13.51
	2005.6128	9.94	355.6	13.86
	2005.6128	10.33	221.6	10.86
	2005.6128	10.49	320.2	10.93
	2005.6128	10.55	296.5	14.41
	2005.6128	11.18	218.9	13.51
	2005.6128	13.09	215.7	14.63
	2005.6128	14.05	141.1	13.35
	2005.6128	14.57	314.9	11.48
	2005.6128	15.06	137.5	11.48
HD 9540	2005.6182	5.51	308.8	14.63
	2005.6182	6.70	120.9	15.56
GJ 82	2005.6647	4.24	78.2	13.89[d]
	2005.6647	5.45	35.3	13.46[d]
	2005.6647	6.27	157.0	11.06[d]
	2005.6647	6.29	228.1	13.80[d]
	2005.6647	6.42	307.0	13.08[d]
	2005.6647	6.75	105.7	9.07[d]
	2005.6647	6.83	106.4	9.23[d]
	2005.6647	6.95	25.7	6.57[d]
	2005.6647	7.63	117.2	13.34[d]
	2005.6647	8.82	315.9	9.27[d]
	2005.6647	9.68	318.7	13.59[d]

Table 4.5 — continued

Star	Epoch	Separation[a] (arcsec)	P.A.[b] (deg)	Δm[c] mag
	2005.6647	9.74	334.0	13.11[d]
	2005.6647	11.37	228.3	12.52[d]
HD 17382	2004.9740	11.78	130.8	13.16
HD 18803	2004.9795	7.61	166.1	17.00
	2004.9795	7.98	208.3	15.68
	2004.9795	10.36	52.8	15.10
HD 19994	2005.6648	6.18	187.4	17.62
	2005.6648	6.30	185.3	16.06
	2005.6648	11.64	72.7	17.51
HD 283750	2004.8132	7.73	175.8	14.65
	2004.8132	12.72	104.2	13.85
HD 30652	2005.6978	2.04	106.3	15.18[d]
	2005.6978	9.53	241.4	18.33[d]
GJ 182	2004.8459	5.15	220.3	12.80
	2004.8459	7.44	233.7	10.61
GJ 234A	2005.8455	3.27	48.8	13.71[d]
	2005.8455	6.64	304.9	16.01[d]
	2005.8455	7.45	215.1	15.03[d]
	2005.8455	10.08	179.3	13.36[d]
	2005.8455	10.24	84.3	10.46[d]
	2005.8455	11.75	103.0	12.58[d]
GJ 281	2005.2286	5.74	237.0	12.48
	2005.2286	8.80	288.4	12.92
	2006.1158	10.64	224.6	13.43[f]
GJ 285	2005.2095	8.83	114.3	11.55
HD 75332	2005.3107	8.25	141.7	11.49
HD 82443	2004.9829	5.27	190.3	11.64[d]
	2004.9829	5.42	191.5	16.65[d]
	2004.9829	8.33	97.8	12.24[d]
	2004.9829	10.17	164.8	16.14[d]
	2004.9829	13.74	215.0	14.67[d]
HD 90905	2005.2098	5.47	188.2	10.91
	2005.2098	12.41	176.8	13.32

Table 4.5 — continued

Star	Epoch	Separation[a] (arcsec)	P.A.[b] (deg)	Δm[c] mag
HD 92945	2005.3983	9.77	236.2	12.82
HD 93528	2005.3271	4.82	332.3	14.27[d]
GJ 402	2006.1273	12.46	324.0	10.80[f]
	2005.3164	13.88	337.7	10.10
HD 96064	2005.2972	4.69	29.7	15.99[e]
	2005.2972	5.94	213.8	8.18
	2005.2972	6.11	213.6	10.76
	2005.2972	8.90	329.7	15.90
HD 102195	2005.3109	11.94	185.5	13.82
HD 102392	2005.3082	5.72	42.0	15.02
	2005.3082	10.57	308.9	14.99[e]
HD 108767B	2005.3055	6.72	87.7	12.41
	2005.3055	8.28	100.1	14.62
	2005.3055	10.20	123.9	15.10
HD 109085	2005.3986	12.92	256.2	15.80
BD+60 1417	2005.2946	2.05	298.4	8.76
	2005.2946	14.08	133.5	12.80[e]
HD 116956	2005.4067	9.34	17.4	15.05
GJ 524.1	2005.2948	7.59	19.7	13.09
HD 124106	2005.2975	7.51	124.8	13.85
	2005.2975	9.39	342.2	9.51
	2005.2975	9.60	341.1	8.71
	2005.2975	10.39	287.5	14.65
	2005.2975	11.17	291.7	14.18
	2005.2975	12.06	120.6	15.45
HD 130322	2005.4014	7.61	329.8	11.00
HD 130948	2005.2922	2.60	103.1	8.56[g]
	2005.2922	2.66	104.0	8.83[g]
HD 135363	2005.2949	7.50	122.1	10.28
HD 139813	2005.4097	6.85	271.3	14.48[d]
	2005.4097	7.36	272.2	14.79[d]
HD 141272	2005.2977	2.31	12.3	11.44
	2005.2977	4.03	286.9	16.59[e]

Table 4.5 — continued

Star	Epoch	Separation[a] (arcsec)	P.A.[b] (deg)	Δm[c] mag
	2005.2977	8.04	305.4	15.78[e]
	2005.2977	8.32	258.1	15.66
	2005.2977	10.95	299.2	9.90
	2005.2977	11.43	190.4	15.14
	2005.2977	12.26	209.5	12.31
GJ 628	2005.2924	5.19	259.0	16.32[e]
	2005.2924	6.29	161.6	14.81
	2005.2924	10.25	232.1	14.90
	2005.2924	10.52	2.8	13.42[e]
	2005.2924	11.49	308.6	14.88
	2005.2924	12.72	228.6	15.10
	2005.2924	13.64	215.4	15.03
HIP 81084	2005.2979	6.84	234.6	13.10
	2005.2979	8.64	4.5	13.70
	2005.2979	9.69	49.6	11.22
	2005.2979	9.98	68.4	13.04
	2005.2979	14.04	226.4	11.60
HD 160934	2005.2952	4.08	319.2	11.03
	2005.2952	8.94	232.9	9.96
HD 162283	2005.3007	2.76	118.7	15.54
	2005.3007	3.41	154.4	14.13
	2005.3007	3.26	4.9	15.21
	2005.3007	3.68	244.8	14.01
	2005.3007	3.94	152.8	14.22
	2005.3007	4.22	158.8	12.52
	2005.3007	4.47	111.9	15.21
	2005.3007	4.37	23.1	13.23
	2005.3007	4.70	299.8	15.44
	2005.3007	4.95	80.0	10.82
	2005.3007	5.24	124.0	16.08
	2005.3007	5.24	191.8	13.38
	2005.3007	5.23	348.9	15.59
	2005.3007	6.07	72.2	14.49

Table 4.5 — continued

Star	Epoch	Separation[a] (arcsec)	P.A.[b] (deg)	Δm[c] mag
	2005.3007	6.61	159.4	12.06
	2005.3007	6.72	84.6	14.28
	2005.3007	6.89	352.8	13.50
	2005.3007	7.11	91.2	8.65
	2005.3007	7.38	176.6	16.29
	2006.7069	7.42	18.0	15.95[f]
	2005.3007	7.33	78.7	15.73
	2005.3007	7.47	75.0	12.53
	2005.3007	7.71	134.8	12.62
	2005.3007	7.94	110.5	15.55
	2005.3007	8.19	198.2	15.44
	2005.3007	8.37	173.6	15.88
	2005.3007	8.60	243.7	14.96
	2005.3007	8.69	132.5	15.01
	2006.7069	9.01	318.9	15.97[f]
	2005.3007	9.08	141.2	12.99
	2005.3007	9.23	152.7	15.98
	2005.3007	9.32	142.4	14.95
	2005.3007	9.37	205.7	13.88
	2005.3007	9.28	337.0	12.77
	2005.3007	9.63	235.2	15.38
	2005.3007	9.56	78.8	13.78
	2006.7069	9.86	286.6	15.74[f]
	2006.7069	10.03	289.1	15.75[f]
	2005.3007	10.20	97.7	13.31
	2005.3007	10.18	37.3	8.81
	2005.3007	10.31	319.4	14.47
	2005.3007	10.48	308.7	15.38
	2005.3007	10.71	337.2	14.52
	2005.3007	10.92	36.3	11.98[e]
	2005.3007	11.36	249.0	13.24
	2005.3007	11.38	112.7	9.04
	2005.3007	11.80	40.1	14.79[e]

Table 4.5 — continued

Star	Epoch	Separation[a] (arcsec)	P.A.[b] (deg)	Δm[c] mag
	2006.7069	12.00	261.7	15.23[f]
	2005.3007	12.01	329.6	9.78
	2005.3007	12.28	153.9	14.26
	2006.7069	12.28	265.3	13.99[f]
	2005.3007	12.43	114.8	9.89[e]
	2006.7069	12.47	71.5	14.76[f]
	2005.3007	12.40	100.7	13.16
	2005.3007	12.61	111.8	13.37[e]
	2005.3007	13.04	16.9	14.10[e]
	2006.7069	13.21	161.5	13.02[f]
	2006.7069	13.46	65.5	14.51[f]
	2005.3007	13.53	303.6	12.68[e]
	2006.7069	13.59	257.1	11.76[f]
	2005.3007	14.12	314.4	12.55[e]
	2005.3007	14.59	112.9	10.20[e]
	2005.3007	14.66	17.4	12.43[e]
	2005.3007	14.74	34.6	11.81[e]
HD 166181	2005.2925	10.38	53.4	14.40
	2005.2925	11.21	195.8	15.04
	2005.2925	13.40	167.6	14.19[e]
	2005.2925	14.46	262.8	11.93[e]
HD 187748	2005.3965	5.51	325.9	15.76
	2005.3965	7.93	277.1	13.01
	2005.3965	8.02	276.7	12.18
	2005.3965	12.81	114.3	9.74
	2005.3965	13.15	321.5	12.52
	2006.7043	15.02	311.3	14.90[f]
GJ 791.3	2005.3992	1.98	341.2	12.03[d]
	2005.3992	2.39	51.3	13.51[d]
	2005.3992	3.77	289.0	10.92[d]
	2005.3992	3.80	137.6	13.99[d]
	2005.3992	3.87	19.4	10.01[d]
	2005.3992	4.38	201.6	14.31[d]

Table 4.5 — continued

Star	Epoch	Separation[a] (arcsec)	P.A.[b] (deg)	Δm[c] mag
	2005.3992	5.55	300.0	12.72[d]
	2005.3992	5.96	49.6	10.28[d]
	2005.3992	6.56	232.8	12.91[d]
	2005.3992	6.66	155.9	13.37[d]
	2005.3992	6.73	254.7	12.93[d]
	2005.3992	8.01	10.3	13.03[d]
	2005.3992	8.25	143.8	15.03[d]
	2005.3992	8.31	71.5	15.02[d]
	2005.3992	8.36	155.7	13.62[d]
	2005.3992	8.89	177.3	12.86[d]
	2005.3992	9.33	10.5	14.93[d]
	2005.3992	9.55	276.2	15.45[d]
	2005.3992	9.64	195.5	14.14[d]
	2005.3992	9.89	347.0	15.16[d]
	2005.3992	10.05	255.1	14.63[d]
	2005.3992	10.12	201.2	13.28[d]
	2005.3992	10.21	310.6	14.36[d]
	2005.3992	10.22	328.8	10.56[d]
	2005.3992	10.55	166.9	15.14[d]
	2005.3992	10.63	80.3	13.51[d]
	2005.3992	10.75	326.6	11.48[d]
	2005.3992	10.80	57.8	10.86[d]
	2005.3992	10.84	51.7	14.67[d]
	2005.3992	11.26	243.5	9.22[d]
	2005.3992	11.58	315.9	9.96[d]
	2005.3992	11.71	14.8	13.26[d]
	2005.3992	12.17	18.6	11.27[d]
	2005.3992	12.45	46.6	12.52[d]
	2005.3992	12.80	274.4	11.86[d]
	2005.3992	13.07	127.8	11.44[d]
	2005.3992	13.08	75.4	13.58[d]
	2005.3992	13.23	81.0	11.26[d]
	2005.3992	13.73	70.5	8.91[d]

Table 4.5 — continued

Star	Epoch	Separation[a] (arcsec)	P.A.[b] (deg)	Δm[c] mag
	2005.3992	14.41	65.8	11.04[d]
	2005.3992	15.14	356.5	11.98[d]
	2005.3992	15.23	179.8	12.02[d]
HD 201651	2005.4867	3.67	201.4	12.48
	2005.4867	8.39	259.1	12.90
	2005.4867	14.53	331.5	13.75[e]
HD 202575	2005.5386	5.54	28.5	12.41
	2005.5386	12.37	168.0	13.98
GJ 4199	2004.6431	9.16	319.9	12.24
	2004.6431	11.76	177.6	10.58
HD 206860	2005.6069	3.67	60.0	15.13
HD 208313	2005.4868	2.93	30.6	14.78
	2005.4868	6.24	31.1	9.69
	2005.4868	9.45	301.0	14.41
	2005.4868	10.45	137.8	16.50[e]
	2005.4868	11.43	151.6	15.85
	2005.4868	13.23	121.0	13.73
	2005.4868	13.51	33.2	14.61
	2005.4868	15.13	63.8	12.00
V383 Lac	2005.5660	4.00	100.0	14.14
	2005.5660	4.02	79.3	15.98
	2005.5660	4.63	204.6	11.81
	2005.5660	4.70	207.7	14.89
	2005.5660	8.49	181.6	14.82
	2005.5660	9.09	110.0	11.65
	2005.5660	9.55	358.6	14.15
	2005.5660	10.59	93.0	8.48
	2005.5660	11.68	142.3	11.24
HD 213845	2005.6453	12.85	214.2	14.91
GJ 875.1	2005.6071	7.83	343.9	9.40
	2005.6071	8.97	260.7	12.73
	2005.6071	11.42	151.3	12.30
	2005.6071	14.54	15.2	11.85[e]

Table 4.5 — continued

Star	Epoch	Separation[a] (arcsec)	P.A.[b] (deg)	Δm[c] mag
GJ 9809	2006.7019	2.10	240.4	15.30[f]
	2005.5907	2.18	30.6	12.91
	2006.7019	3.22	141.6	15.55[f]
	2005.5907	3.35	207.8	12.31
	2005.5907	3.55	337.2	11.53
	2005.5907	3.79	173.8	11.92
	2006.7019	4.51	0.9	16.23[f]
	2005.5907	5.37	258.1	14.38
	2006.7019	5.66	118.3	15.35[f]
	2005.5907	6.39	68.9	15.47
	2005.5907	7.01	101.1	9.69
	2005.5907	7.34	236.9	13.49
	2005.5907	7.69	127.3	11.26
	2005.5907	7.75	131.1	14.21
	2006.7019	7.92	78.4	15.65[f]
	2006.7019	9.08	247.3	14.84[f]
	2005.5907	9.18	36.5	15.03
	2005.5907	9.23	27.2	14.80
	2005.5907	9.51	95.2	12.35
	2006.7019	9.58	84.1	15.30[f]
	2005.5907	9.98	68.5	14.35
	2005.5907	9.98	121.4	10.42
	2006.7019	10.02	163.4	15.37[f]
	2005.5907	10.18	93.9	13.69
	2006.7019	10.73	12.2	15.33[f]
	2005.5907	10.64	248.1	13.59
	2005.5907	10.94	254.4	9.90
	2005.5907	11.23	82.9	13.75
	2006.7019	11.40	336.1	15.18[f]
	2005.5907	11.69	155.9	12.14
	2005.5907	11.87	32.2	12.28
	2005.5907	11.74	291.2	7.01
	2005.5907	12.23	310.2	8.73

Table 4.5 — continued

Star	Epoch	Separation[a] (arcsec)	P.A.[b] (deg)	Δm[c] mag
	2005.5907	12.75	66.9	12.76
	2005.5907	13.03	58.0	11.09
	2005.5907	12.93	332.5	13.42
	2005.5907	14.04	309.7	12.50
HD 220140	2005.5934	6.14	358.5	15.96
	2005.5934	15.19	50.4	10.62[e]
HD 221503	2005.6646	9.02	234.4	15.61[d]
GJ 900	2004.6458	7.41	76.0	14.20
	2004.6458	12.15	150.6	12.53
	2004.6458	12.41	96.4	9.36
GJ 907.1	2005.6837	7.93	296.7	13.68

Note. — Target stars around which no point source was detected are omitted from this table. Unless stated otherwise, all point sources listed were confirmed to be background objects using data from two epochs.

[a]Uncertainty is 0.015″, see text for detail.

[b]Uncertainty is 0.2°, see text for detail.

[c]Uncertainties are given in Table 4.3, see text for detail.

[d]No second epoch data available.

[e]Source undetected in second epoch data.

[f]Source detected in second epoch data only.

[g]Previously known brown dwarf companion (Potter et al., 2002; Goto et al., 2002).

4.4.3 Multiple systems

As mentioned in §4.2, 16 of the target stars are part of multiple systems. As an orbital solution can potentially be determined in a reasonable amount of time for close-separation multiple systems, the measured properties of the systems observed that have a separation below 2″ are presented in Table 4.6 as a reference for future studies. Two of the close-separation systems observed were resolved for the first time by our observations (HD 14802 and HD 166181), and a third system (HD 213845) was found to be a relatively large separation (∼6″) binary for which we have found no prior indication in the literature; since HD 213845 is reported to be part of a binary system for the first time in this paper, its properties are presented in Table 4.6 as well. The three multiple systems observed for the first time in this work are discussed in more detail below.

HD 14802 A source 12 ± 2 times fainter than HD 14802 was detected at a separation of $0.469'' \pm 0.005''$ and P.A. $267.1° \pm 0.7°$ (epoch 2005.6348); the large uncertainty on the flux ratio is due to the peak of the primary star PSF being saturated. Common proper motion of the pair was not verified but the system is likely bound given the brightness and close separation of the companion. The Hipparcos catalog (Perryman & ESA, 1997) indicates that the proper motion of this star is accelerating and the star is likely part of a binary system; an astrometric solution for the system was obtained by Gontcharov et al. (2000). The estimated period and semi-major axis are 25 yr and 0.5″, respectively, consistent with the projected separation we have measured.

HD 166181 This star has been known for a long time to be a spectroscopic binary with a period of only 1.8 days (Nadal et al., 1974). More recently, analysis of additional radial velocity data has lead Dempsey et al. (1996) to propose that the system is in fact triple; a proposition which was confirmed by Fekel et al. (2005), who found radial velocity variations ascribable to a third component with an orbit of period 5.7 year and eccentricity 0.765. Further, by reanalyzing Hipparcos data in light of this new component, these authors have found a new astrometric solution for the system, leading to revised

Table 4.6. Properties of close separation multiple systems

Name	Epoch	Separation (″)	P.A. (°)	Brightness ratio[a]	1st spatially resolved observation
HD 14802AB	2005.6348	0.469 ± 0.005	267.1 ± 0.7	12 ± 2	This work
GJ 234AB	2005.8455	1.392 ± 0.002	44.5 ± 0.1	4.7 ± 0.1	W. Baade (1955), c.f. Gatewood et al. (2003)
HD 77407AB	2005.3163	1.702 ± 0.004	355.6 ± 0.1	7.4 ± 0.3	Mugrauer et al. (2004)
HD 102392AB	2005.3083	1.134 ± 0.002	172.5 ± 0.1	7.8 ± 0.3	Rossiter (1955)
	2006.1929	1.137 ± 0.002	171.1 ± 0.1		
HD 129333AB	2005.3004	0.766 ± 0.002	173.0 ± 0.2	14.0 ± 0.5	Metchev & Hillenbrand (2004)
HD 135363AB	2005.2950	0.302 ± 0.002	129.9 ± 0.5	4.0 ± 0.1	This work[b]
	2006.1277	0.316 ± 0.002	131.8 ± 0.5		
HD 160934AB	2005.2953	0.213 ± 0.002	268.5 ± 0.7	2.2 ± 0.1	Hormuth et al. (2007)
	2006.7097	0.218 ± 0.002	271.3 ± 0.7		
HD 166181AabB	2005.2926	0.065 ± 0.005	16.2 ± 5.0	5.5 ± 0.4	This work
	2006.7124	0.102 ± 0.003	51.5 ± 2.0		
HD 167605AB	2005.4017	1.182 ± 0.002	46.9 ± 0.1	8.2 ± 0.2	Arribas et al. (1998)
HD 213845AB	2005.6453	6.09 ± 0.03	129.8 ± 0.4	∼125[c]	This work
	2006.5108	6.09 ± 0.03	129.6 ± 0.4		
GJ 900AB	2004.6459	0.611 ± 0.002	334.3 ± 0.2	5.7 ± 0.2	Martín (2003)
	2005.6864	0.673 ± 0.002	338.8 ± 0.2		
GJ 900AC	2004.6459	0.733 ± 0.002	344.7 ± 0.2	12.0 ± 0.2	Martín (2003)
	2005.6864	0.722 ± 0.002	345.6 ± 0.2		
GJ 907.1AB	2005.6837	0.789 ± 0.002	213.5 ± 0.2	1.62 ± 0.05	Rossiter (1955)
	2006.5411	0.775 ± 0.002	212.1 ± 0.2		

[a]Brightness of the primary over that of the companion, in the NIRI CH4-short filter..

[b]The peak of both the primary and companion is saturated in the data; the ratio quoted is an estimate based on the comparison of radial profiles.

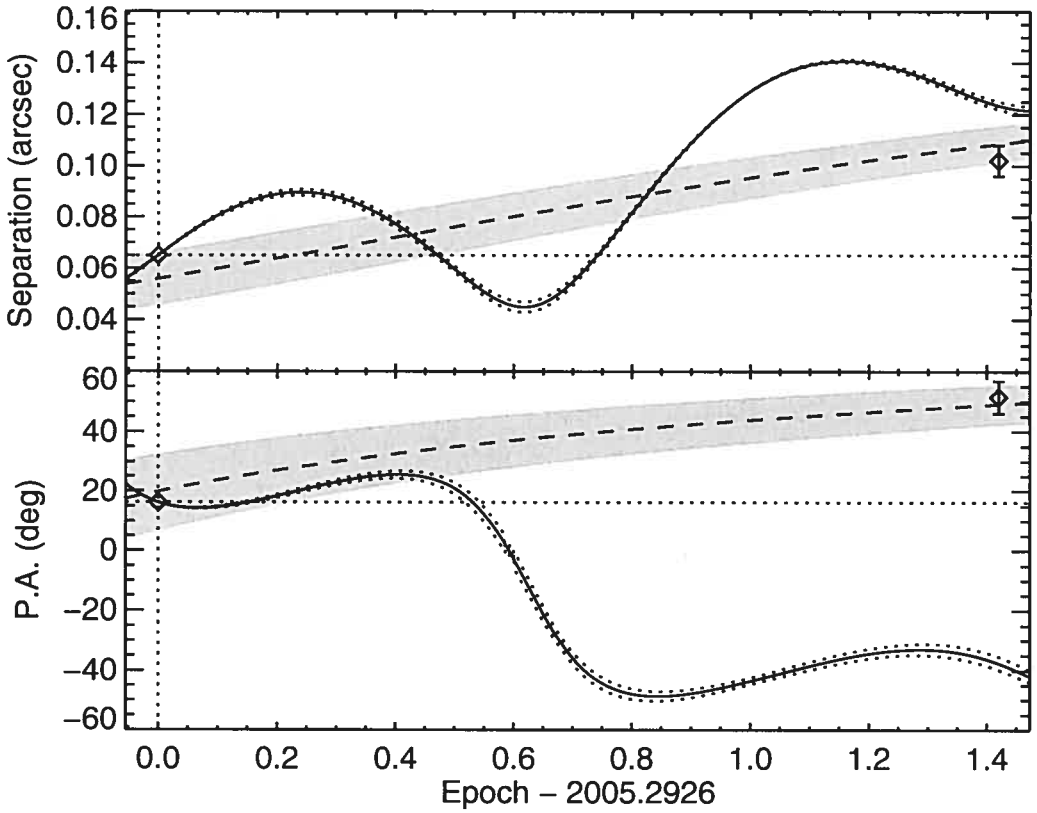

Figure 4.7 Verification of the physical association of the point source detected around HD 166181. Open diamonds mark the observed separation (*top*) and P.A. (*bottom*) of the point source at the two epochs. The solid line indicates the expected separation and P.A. of a distant background source as a function of time. The predicted separation and P.A. of HD 166181B based on the astrometric solution of Fekel et al. (2005) are shown as *dashed lines*, with uncertainties indicated by the shaded areas.

values of parallax and proper motion (see Table 4.1) and to a determination of the orbital inclination of the long-period companion. Based on their complete solution, they estimate the semi-major axis of the outer companion at 0.077″ (2.5 AU) and its mass at 0.79 $M_{\odot}$. Our observations have resolved the long-period companion of this triple system. In 2005.2926, the companion was located at a separation of $0.065'' \pm 0.005''$ and P.A. of $16.2° \pm 5.0°$, and in 2006.7124, it was located at a separation of $0.102'' \pm 0.003''$ and P.A. of $51.5° \pm 2.0°$. The evolution of the separation and P.A. of this source between the two epochs is far from that expected for an unrelated background source and is in very good agreement with the orbital motion expected based on the astrometric solution of Fekel et al. (2005) (see Fig. 4.7), confirming that the source observed is HD 166181B. The flux ratio of the component Aab to component B is ~5.5, a contrast of ~1.85 mag.

HD 213845 A bright source is visible in our data at a separation of $6.09'' \pm 0.03''$ and P.A. of $129.8° \pm 0.4°$ from HD 213845 (epoch 2005.6453). This source did not change separation nor P.A. between our 2005 and 2006 observations (see Figure 4.8), indicating that it is bound to HD 213845. The companion is only visible in our saturated data as its separation exceeds the field of view of the sub-array used for the unsaturated observations. Further, being relatively bright, the peak of the companion's PSF is saturated in all our data, making it very difficult to estimate its flux ratio to the primary and explaining the larger uncertainty on the separation and P.A. quoted above. We have nevertheless estimated that the companion is ~125 times fainter than its primary based on a comparison of their radial intensity profiles at radii where the data are in the linear regime of the detector. The companion was possibly detected by 2MASS, but its measured position and photometry in the 2MASS point source catalog (PSC) are affected by confusion due to the nearby primary. Nevertheless, the relative position of this source in the 2MASS PSC, separation of 5.55″ and P.A. of 128°, is consistent with the star being gravitationally bound to HD 213845 as, were it not a bound companion, its separation should have changed by ~2″ between the 2MASS observations and our first epoch observations. Although the separation of this binary system is well above the resolution

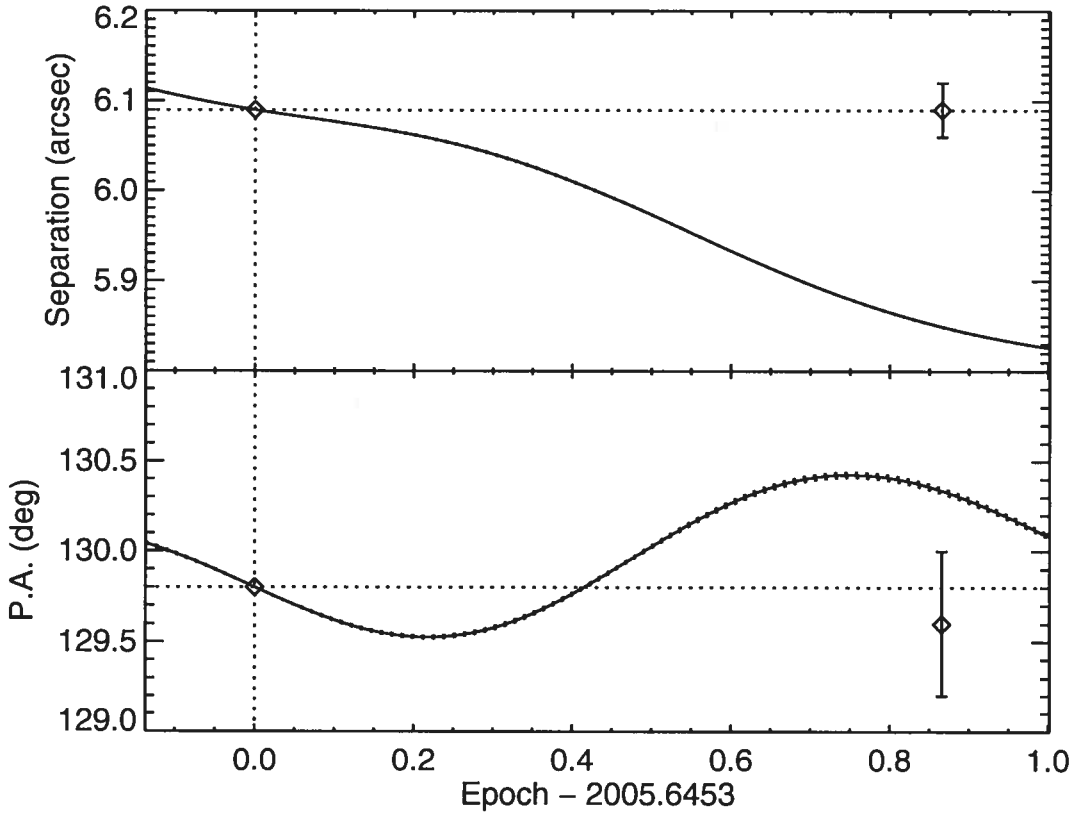

Figure 4.8 Same as Figure 4.7 for HD 213845

limit of seeing-limited observations, we have found no prior indication of binarity in the literature.

4.5 Analysis and discussion

The detection limits determined in §4.4.1 can be used to calculate an upper limit to the fraction of stars that have companions of mass and semi-major axis inside some given intervals. The analysis presented in this section is largely guided by the work of Brandeker et al. (2006); Carson et al. (2006); Allen et al. (2005); and Sivia (1996). The statistical formalism for the analysis is presented first and various applications to our data are presented afterward.

4.5.1 Statistical formalism

Consider the observation of N stars enumerated by $j = 1 \ldots N$. Let f be the fraction of stars that have at least one companion of mass and semi-major axis in the intervals $[m_{\min}, m_{\max}]$ and $[a_{\min}, a_{\max}]$, respectively, and p_j the probability that such a companion around star j, if indeed it was there, would be detected given the detection limits of the observations. The probability of detecting such a companion around star j is fp_j, and the probability of not detecting a companion around this star is simply $1 - fp_j$. If the set $\{d_j\}$ denotes the detections made by the observations, such that d_j equals 1 if a companion is detected around star j or else equals 0, then the probability that the observed outcome would occur, also called the likelihood of the data given f, is given by

$$\mathscr{L}(\{d_j\}|f) = \prod_{j=1}^{N} (1 - fp_j)^{(1-d_j)} (fp_j)^{d_j}. \tag{4.3}$$

According to Bayes' theorem, from the *a priori* probability density $p(f)$, or prior distribution, and the likelihood function $\mathscr{L}$, one may calculate $p(f|\{d_j\})$, the probability density updated in light of the data, or posterior distribution:

$$p(f|\{d_j\}) = \frac{\mathscr{L}(\{d_j\}|f)p(f)}{\int_0^1 \mathscr{L}(\{d_j\}|f)p(f)\mathrm{d}f}. \tag{4.4}$$

In this study, since we have no prior knowledge about f, we use the most ignorant prior distribution $p(f) = 1$.

The posterior distribution $p(f|\{d_j\})$ can be used to determine a credible interval (CI) for f, bounded by $f_{\min}$ and $f_{\max}$, for a given level of credibility α. For a case where there is no detection, as is the case with our survey, then clearly $f_{\min} = 0$, and the upper bound of the CI is found by solving

$$\alpha = \int_0^{f_{\max}} p(f|\{d_j\})\mathrm{d}f. \tag{4.5}$$

For a case where there are some detections, an equal-tail CI is found by solving

$$\frac{1-\alpha}{2} = \int_0^{f_{\min}} p(f|\{d_j\})\mathrm{d}f \quad \text{and} \quad \frac{1-\alpha}{2} = \int_{f_{\max}}^1 p(f|\{d_j\})\mathrm{d}f. \tag{4.6}$$

In this work a value of $\alpha = 0.95$ was chosen.

The determination of the p_j's is a critical step of this analysis; their value depends on the detection limits of the observations, on the ages and distances of the systems, and on the mass, semi-major axis, and orbital eccentricity distributions of the companions. In calculating the p_j's it is also important to account properly for orbital inclination and phase as these affect significantly the distribution of projected separations for an orbit of given semi-major axis. In this work, the p_j's were calculated using a Monte Carlo approach. The mass and semi-major axis intervals, $[m_{\min}, m_{\max}]$ and $[a_{\min}, a_{\max}]$, were first selected. Then for each target star, 10000 planets were generated by sampling randomly, for each planet, the mass, semi-major axis, orbital eccentricity, orbital separation projection factor, age of the system, and underlying residual noise in the image. The mass and semi-major axis distributions are left arbitrary for the moment; different possibilities will be explored later. For all of our calculations, the orbital eccentricity distribution was assumed to be that of the radial velocity exoplanets sample, which was approximated by a Gaussian function of mean 0.25, standard deviation 0.19, and with $0 \leq e \leq 0.8$ (Marcy et al., 2005). The orbital separation projection factor was sampled using the method described in Appendix A of Brandeker et al. (2006); this method properly takes into consideration orbital eccentricities, phases, and orientations. The age was sampled linearly within the range indicated in Table 4.1. Given the age assigned to each planet, the procedure described in 4.4.1 was used to convert its mass into a magnitude difference in the NIRI CH4-short filter. The projected physical separation of each planet was converted into an angular separation based on the distance of its primary star. The random noise added to each planet was drawn from a Gaussian distribution of standard deviation equal to the measured residual noise at the separation of the planet. The ef-

fect of adding this noise is to either increase or decrease the signal that a planet would have in the residual image. The signal of some "a priori detectable" planets near the detection limit will thus decrease below the 5σ detection limit, while the signal of some "a priori undetectable" planets will be boosted above the detection limit such that the appropriate detection completeness will result for planets of various true intensities (see §4.4.1). Finally, given the sample of planets assigned to target j, the probability p_j was calculated as the fraction of planets lying above the corresponding 5σ detection limits (c.f. Table 4.4).

The above determination of the p_j's yields a CI for f that is a function of the assumptions made on the mass and semi-major axis distributions. For a case where there is no detection, it is also possible to obtain a more conservative estimate of $f_{\max}$ that is valid for any distributions of mass and semi-major axis. The procedure used to do this is identical to that described above except for the following. Rather than populating the whole intervals of mass and semi-major axis considered, all planets are assigned a mass and semi-major axis precisely equal to $m_{\min}$ and $a_{\min}$, respectively. Because more massive or more distant planets are easier to detect, the values of p_j's calculated in this manner constitute lower limits to the values that would be obtained by populating the whole intervals assuming any specific distributions; accordingly, the resulting value of $f_{\max}$ constitutes an upper limit. This approach is perfectly legitimate as long as $a_{\max}$ is chosen such that the values of p_j's for any a in $[a_{\min}, a_{\max}]$ are at least as large as those for $a_{\min}$.

It is possible to derive a simple analytic expression for $f_{\max}$ for a case where there is no detection; this expression may be useful to estimate what the results of an ongoing survey will be or scale actual results for different values of N or detection probabilities. This expression may be obtained by first replacing each p_j by the average detection probability $\langle p_j \rangle$ in Eq. (4.3), and then recognizing that the likelihood function can be

approximated by $e^{-Nf\langle p_j \rangle}$. This leads to

$$f_{\max} \approx \frac{-\ln(1-\alpha)}{N\langle p_j \rangle}. \tag{4.7}$$

This approximation, valid for $N\langle p_j \rangle \gg 1$, is equivalent to using Poisson statistics rather than Binomial statistics for the presence of companions (c.f. Eq. 3–7 of Carson et al. 2006).

4.5.2 $f_{\max}$ for arbitrary mass and semi-major axis distributions

As a first analysis of the survey results, we present estimates of $f_{\max}$ that are independent of the mass and semi-major axis distributions for $m_{\min}$ =0.5, 1, 2, 3, 4, 5, 7.5, 10, and 13 $M_{\rm Jup}$, and for all $a_{\min}$ between 10 and 500 AU; these estimates were calculated according to the last procedure described above. For this analysis, and those in the next section, we have not considered the 6 stars with candidates for which second epoch observations are missing. The results obtained in this section are valid for any $m_{\max}$ up to $\sim$40 $M_{\rm Jup}$ as no companion with a mass below this value was detected.[8] Planet detection probabilities for each star are indicated in Table 4.7 for a small selection of masses and semi-major axes, while the mean planet detection probabilities, i.e. the average of the p_j's over all j's, are shown in Figure 4.9 as a continuous function of semi-major axis and for a larger selection of masses. The peak sensitivity of the survey occurs for semi-major axes between 50 and 200 AU; the peak values are $\sim$45% and $\sim$68% for 2 and 5 $M_{\rm Jup}$, respectively. The survey is particularly sensitive to brown dwarfs ($m \gtrsim 13\ M_{\rm Jup}$), with a detection probability above 75% between 35 and 200 AU. A decline in sensitivity occurs at a separation of $\sim$200 AU; this is consistent with the field of view of the observations ($\sim 11''$ radius) and mean distance of the targets (22 pc).

The results for $f_{\max}$ are shown in Figure 4.10. For a semi-major axis interval lower

[8]The previously known 40–65 $M_{\rm Jup}$ binary brown dwarf companion located 2.6″from HD 130948 (Potter et al., 2002; Goto et al., 2002) is detected in our data.

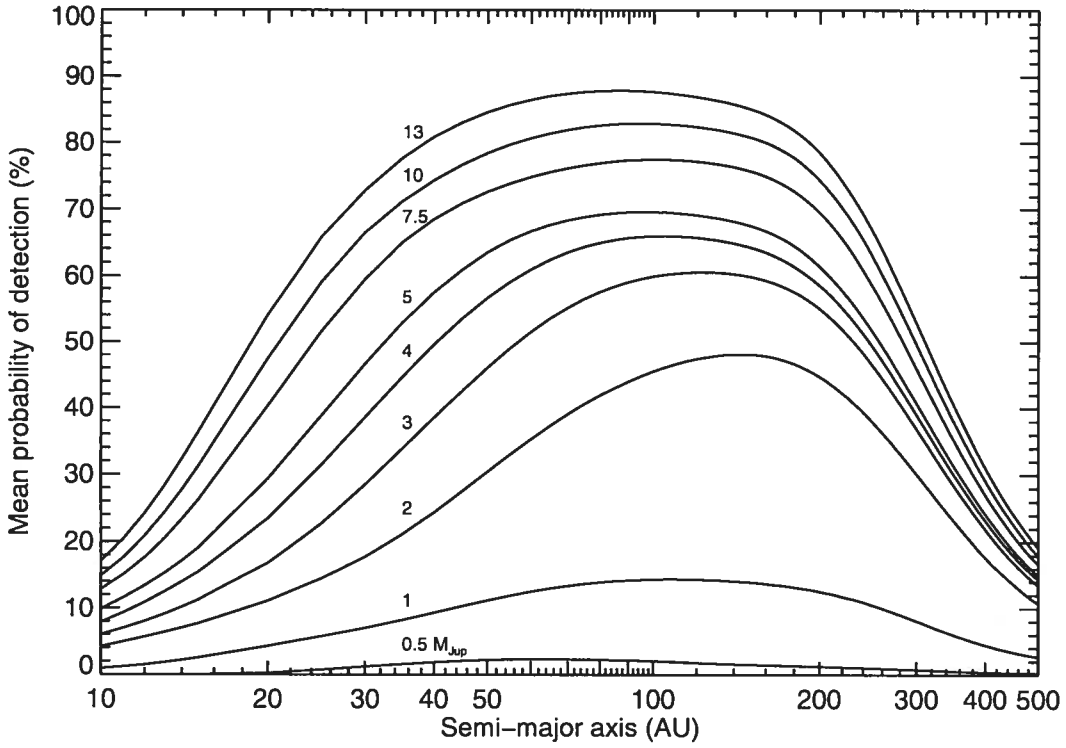

Figure 4.9 Mean probability of detection of a planet of given mass as a function of the semi-major axis of its orbit; the curves are labeled by the mass of the planet, in $M_{\rm Jup}$. The mean is obtained over all targets of the survey.

bound of 50 AU, the 95% credible planet frequency upper limits are 0.28 for 1–13 $M_{\rm Jup}$ and 50–225 AU, 0.12 for 2–13 $M_{\rm Jup}$ and 50–295 AU, and 0.057 for 5–13 $M_{\rm Jup}$ and 50–185 AU. For a semi-major axis lower bound of 25 AU, the upper limits are 0.23 for 2–13 $M_{\rm Jup}$ and 25–420 AU and 0.09 for 5–13 $M_{\rm Jup}$ and 25–305 AU. For completeness, the exercise was repeated for circular orbits and for a uniform distribution of eccentricity (between 0 and 1), and the results obtained were very similar to those shown in Figure 4.10.

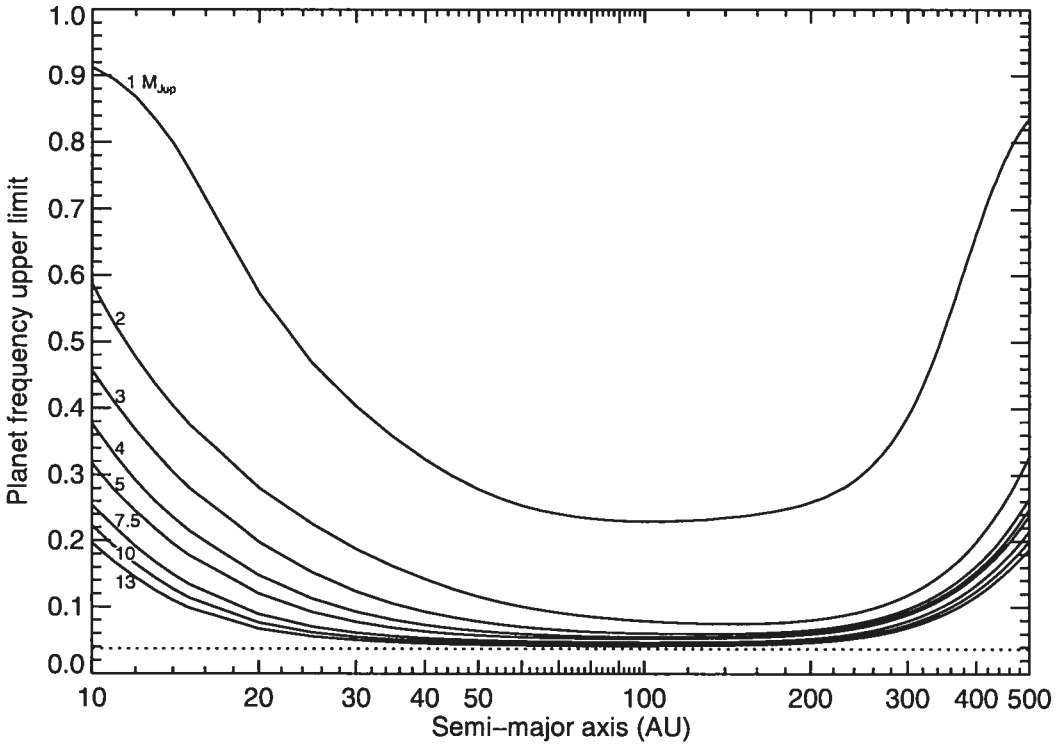

Figure 4.10 Upper limits, with a credibility of 95%, on the fraction of stars harboring at least one companion of mass in the range $[m_{\min}, 40]\ M_{\text{Jup}}$ and orbit of semi-major axis in various ranges. The minimum mass, $m_{\min}$, is indicated on each curve. For any interval, $[a_{\min}, a_{\max}]$ AU, of semi-major axis selected, the correct value of $f_{\max}$ to read from the graph is the maximum of the curve within that interval. The curves shown in this graph are conservative upper limits that are valid for any distributions of mass and semi-major axis. The dotted line indicates the minimum upper limit that one could derive from observation of 79 stars if the probability of detection of a planet was 100% irrespective of its age, mass, and orbital separation.

Table 4.7. Planet detection probability

Name	2 M_{Jup}			5 M_{Jup}			0.5–13 M_{Jup}, $\beta = -1.2$, $\gamma = -1$		
	25 AU	50 AU	100 AU	25 AU	50 AU	100 AU	10–25 AU	25–50 AU	50–250 AU
HD 166	0.002	0.261	0.748	0.693	0.936	0.985	0.120	0.339	0.448
HD 691	0.000	0.078	0.403	0.113	0.730	0.944	0.022	0.191	0.452
HD 1405	0.009	0.602	0.919	0.540	0.906	0.979	0.076	0.348	0.654
HD 5996	0.000	0.035	0.164	0.134	0.575	0.900	0.030	0.176	0.344
HD 9540	0.001	0.041	0.117	0.112	0.370	0.641	0.028	0.148	0.269
HD 10008	0.000	0.010	0.282	0.161	0.792	0.957	0.044	0.212	0.419
GJ 82	0.921	0.983	0.963	0.978	0.993	0.967	0.575	0.788	0.648
HD 14802	0.000	0.000	0.000	0.000	0.000	0.000	0.000	0.000	0.000
HD 16765	0.000	0.019	0.231	0.149	0.730	0.944	0.029	0.192	0.389
HD 17190	0.001	0.016	0.041	0.037	0.115	0.199	0.008	0.059	0.151
HD 17382	0.014	0.138	0.322	0.296	0.752	0.949	0.064	0.236	0.413
HD 17925	0.867	0.972	0.843	0.947	0.987	0.848	0.454	0.697	0.508
HD 18803	0.000	0.000	0.000	0.000	0.000	0.008	0.001	0.019	0.087
HD 19994	0.000	0.000	0.000	0.000	0.000	0.000	0.000	0.005	0.062
HD 20367	0.000	0.003	0.222	0.012	0.486	0.894	0.009	0.123	0.393
2E 759	0.001	0.197	0.648	0.396	0.872	0.973	0.089	0.282	0.490
HD 22049	0.000	0.000	0.000	0.935	0.338	0.068	0.273	0.257	0.035
HIP 17695	0.772	0.951	0.988	0.944	0.987	0.996	0.386	0.614	0.633
HD 25457	0.000	0.030	0.635	0.148	0.797	0.956	0.022	0.203	0.449
HD 283750	0.369	0.864	0.971	0.840	0.966	0.991	0.202	0.506	0.656
GJ 182	0.530	0.906	0.979	0.828	0.964	0.991	0.222	0.610	0.873
GJ 281	0.021	0.310	0.548	0.789	0.956	0.989	0.169	0.375	0.416
GJ 285	0.982	0.992	0.405	0.987	0.993	0.407	0.811	0.961	0.425
HD 72905	0.000	0.000	0.052	0.157	0.804	0.955	0.046	0.209	0.322
HD 75332	0.000	0.026	0.472	0.029	0.624	0.924	0.011	0.148	0.456
HD 77407	0.007	0.381	0.854	0.282	0.828	0.965	0.027	0.266	0.649
HD 78141	0.116	0.719	0.942	0.708	0.938	0.986	0.121	0.413	0.601
HD 82558	0.373	0.867	0.971	0.825	0.962	0.990	0.184	0.505	0.661
GJ 393	0.971	0.992	0.511	0.981	0.994	0.513	0.664	0.789	0.402
HD 90905	0.000	0.060	0.553	0.073	0.716	0.940	0.014	0.173	0.470
HD 91901	0.000	0.000	0.005	0.001	0.020	0.058	0.001	0.009	0.045
HD 92945	0.003	0.444	0.886	0.517	0.902	0.978	0.079	0.322	0.530
HD 93528	0.000	0.020	0.371	0.014	0.570	0.915	0.009	0.132	0.431
GJ 402	0.958	0.942	0.271	0.991	0.951	0.274	0.581	0.672	0.225
HD 96064	0.064	0.642	0.927	0.664	0.929	0.984	0.100	0.383	0.598
HD 97334	0.007	0.252	0.610	0.513	0.902	0.978	0.063	0.300	0.489
HD 102195	0.000	0.002	0.015	0.010	0.057	0.116	0.003	0.027	0.097
HD 102392	0.000	0.004	0.018	0.014	0.064	0.124	0.005	0.030	0.100
HD 105631	0.000	0.000	0.000	0.000	0.000	0.000	0.000	0.017	0.107
HD 107146	0.000	0.197	0.798	0.286	0.845	0.966	0.035	0.250	0.533
HD 108767B	0.001	0.122	0.456	0.169	0.774	0.953	0.038	0.214	0.468
HD 109085	0.000	0.000	0.000	0.000	0.000	0.093	0.001	0.022	0.128
BD+60 1417	0.749	0.946	0.987	0.938	0.985	0.996	0.384	0.612	0.645
HD 111395	0.000	0.000	0.000	0.002	0.175	0.532	0.018	0.118	0.207
HD 113449	0.005	0.488	0.894	0.604	0.920	0.982	0.096	0.340	0.548
GJ 507.1	0.000	0.010	0.023	0.033	0.093	0.141	0.011	0.053	0.100
HD 116956	0.000	0.051	0.237	0.174	0.715	0.942	0.043	0.200	0.375
HD 118100	0.155	0.802	0.956	0.810	0.959	0.989	0.191	0.452	0.584
GJ 524.1	0.001	0.012	0.025	0.034	0.100	0.147	0.011	0.058	0.116
HD 124106	0.000	0.000	0.000	0.000	0.002	0.105	0.003	0.056	0.163
HD 125161B	0.000	0.008	0.022	0.016	0.064	0.116	0.004	0.031	0.092
HD 129333	0.014	0.296	0.799	0.246	0.817	0.962	0.028	0.254	0.582
HD 130004	0.001	0.011	0.026	0.037	0.099	0.154	0.012	0.056	0.114

Table 4.7 — continued

Name	$2\ M_{\rm Jup}$			$5\ M_{\rm Jup}$			0.5–13 $M_{\rm Jup}$, $\beta=-1.2$, $\gamma=-1$		
	25 AU	50 AU	100 AU	25 AU	50 AU	100 AU	10–25 AU	25–50 AU	50–250 AU
HD 130322	0.000	0.000	0.000	0.000	0.000	0.005	0.001	0.016	0.104
HD 130948	0.023	0.451	0.876	0.584	0.916	0.981	0.071	0.336	0.567
HD 135363	0.005	0.370	0.858	0.333	0.856	0.969	0.045	0.284	0.568
HD 141272	0.001	0.167	0.512	0.573	0.915	0.980	0.086	0.304	0.462
HD 147379B	0.168	0.264	0.252	0.815	0.961	0.872	0.241	0.372	0.279
GJ 628	0.077	0.056	0.013	0.468	0.333	0.067	0.209	0.240	0.048
HIP 81084	0.002	0.364	0.863	0.494	0.898	0.977	0.085	0.315	0.528
HD 160934	0.500	0.900	0.978	0.855	0.968	0.992	0.231	0.574	0.780
HD 162283	0.002	0.019	0.035	0.049	0.125	0.200	0.016	0.072	0.140
HD 166181	0.000	0.058	0.508	0.119	0.756	0.949	0.021	0.193	0.468
HD 167605	0.000	0.003	0.015	0.004	0.043	0.093	0.002	0.018	0.078
HD 187748	0.000	0.126	0.689	0.181	0.799	0.958	0.036	0.223	0.516
HD 197481	0.910	0.980	0.808	0.913	0.980	0.810	0.538	0.897	0.622
HD 201651	0.000	0.004	0.015	0.008	0.043	0.089	0.002	0.019	0.073
HD 202575	0.009	0.102	0.204	0.262	0.651	0.921	0.070	0.218	0.333
GJ 4199	0.518	0.904	0.978	0.841	0.965	0.991	0.213	0.567	0.799
HD 206860	0.000	0.018	0.255	0.427	0.882	0.974	0.082	0.262	0.413
HD 208313	0.012	0.106	0.200	0.296	0.676	0.923	0.082	0.228	0.351
V383 LAC	0.024	0.443	0.869	0.584	0.915	0.980	0.105	0.347	0.567
HD 213845	0.000	0.001	0.172	0.056	0.710	0.938	0.016	0.168	0.394
GJ 875.1	0.214	0.793	0.954	0.917	0.982	0.994	0.284	0.463	0.479
GJ 876	0.059	0.054	0.013	0.372	0.333	0.068	0.160	0.219	0.053
GJ 9809	0.811	0.960	0.990	0.920	0.982	0.994	0.396	0.717	0.893
HD 220140	0.150	0.736	0.945	0.771	0.952	0.988	0.136	0.426	0.573
GJ 900	0.008	0.443	0.874	0.644	0.928	0.984	0.116	0.353	0.491
GJ 907.1	0.000	0.000	0.007	0.009	0.528	0.906	0.015	0.134	0.344
Mean	0.144	0.304	0.456	0.388	0.635	0.696	0.122	0.284	0.392

The results also indicate that no more than 0.056 of stars have low-mass brown dwarf companions ($13 < m/M_{\rm Jup} < 40$) between 25 and 250 AU. For determining the frequency of stars with at least one companion in the whole brown dwarf mass range ($13 < m/M_{\rm Jup} < 75$) over the same range of semi-major axis, the brown dwarf companion to HD 130948 (Potter et al., 2002; Goto et al., 2002) must be taken into account explicitly. This analysis must be carried out with care as the semi-major axis of this companion could be significantly different from its measured projected physical separation of 47 AU. It is possible to account for this uncertainty by calculating the probability distribution of the real semi-major axis of the brown dwarf companion using a Monte Carlo approach similar to the one presented above for the calculation of the p_j's. Basically, the projected separation of the companion is fixed at $s = 47$ AU and its orbital eccentricity and orbital projection factor are sampled randomly 10^5 times, as described

above. The de-projected semi-major axis is then calculated for each random trial and its normalized distribution over all trials is obtained. As the projection factor can never be larger than $(1+e_{\rm max})$, where $e_{\rm max}$ is the maximum eccentricity allowed, the semi-major axis probability distribution is equal to zero below $s/(1+e_{\rm max})$; the distribution extends to infinity for higher values. Applied to the current case, this calculation indicates that at a 95% credible interval for the semi-major axis of the binary brown dwarf companion to HD 130948 is 26–157 AU. We thus posit that our observations have resulted in one detection in the semi-major axis interval 25–200 AU and mass interval 13–75 $M_{\rm Jup}$; then using the procedure described in the previous section and Eq. (4.6), the 95% credible interval for the frequency of stars with at least one brown dwarf companion in the semi-major axis interval 25–250 AU is $0.019^{+0.083}_{-0.015}$. This result is consistent with the upper limit of 0.12 (95% credibility) reported by Carson et al. (2006) for the 25–100 AU semi-major axis interval and also with the fraction of $0.068^{+0.083}_{-0.049}$ (95% credibility) reported by Metchev & Hillenbrand (2004) for the range 30–1600 AU. For smaller semi-major axes, our results indicate that, with a credibility of 95%, the fraction of stars with at least one brown dwarf companion in the range 10–25 AU is less than 0.20, and less than 0.10 for the range 15–25 AU.

4.5.3 $f_{\rm max}$ for specific mass and semi-major axis distributions

In this section we derive first an upper limit to the fraction of stars harboring at least one planet in the single mass interval $[0.5, 13]$ $M_{\rm Jup}$, assuming that the mass distribution follows $dn/dm \propto m^{-1.2}$. The mass distribution adopted is based on a statistical analysis of the RV results that properly accounts for the detection sensitivity reached for each star (A. Cumming et al. 2007, in preparation) and is formally valid only for planets with semi-major axis below ~3 AU; here it is blindly extrapolated to larger semi-major axes. For comparison, a simple fit of the mass distribution of the RV exoplanets sample yields $dn/dm \propto m^{-1.1}$ (Butler et al., 2006). For this calculation the whole mass interval is populated according to the distribution stated, but all planets are assigned a value $a_{\rm min}$ for the

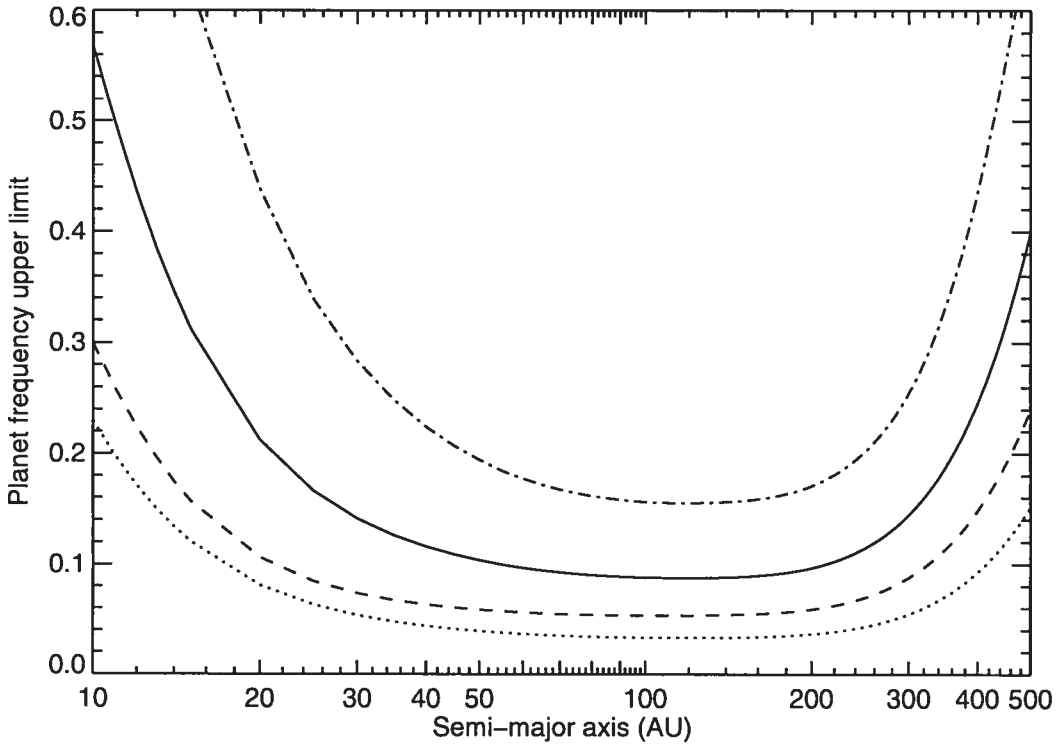

Figure 4.11 Upper limits, with a credibility of 95%, on the fraction of stars harboring at least one planet of mass in the range $[0.5, 13]\ M_{\rm Jup}$, assuming $\mathrm{d}n/\mathrm{d}m \propto m^{\beta}$, and semi-major axis in various ranges. The values of β are -2 (*dot-dashed line*), -1.2 (*solid line*), and 0 (*dashed line*). For any interval, $[a_{\rm min}, a_{\rm max}]$ AU, of semi-major axis selected, the correct value of $f_{\rm max}$ to read from the graph is the maximum of the curve within that interval. The 67% credibility curve for $\beta = -1.2$ is also shown (*dotted line*).

semi-major axis, so as to make the results independent of its distribution. The calculation was made for all $a_{\rm min}$ between 10 and 500 AU. The results are shown in Figure 4.11. With a credibility of 95%, the fraction of stars having at least one planet of mass in the range $[0.5, 13]\ M_{\rm Jup}$ and semi-major axis in $[10, 500]$, $[25, 340]$, and $[50, 230]$ AU is less than 0.57, 0.17, and 0.10, respectively. For reference, results of the same analysis assuming $\mathrm{d}n/\mathrm{d}m \propto m^{\beta}$, with $\beta = 0$ and -2, are presented also in Figure 4.11. As expected, a smaller β leads to larger values of $f_{\rm max}$ because a larger fraction of planets have a smaller mass, while a larger value of β has the opposite effect.

Next we calculate upper limits for the same mass interval by assuming further that the distribution of semi-major axes follows $dn/da \propto a^{\gamma}$, for $\gamma = -1$, 0, and 1. This range of power-law index includes the value of $\gamma = -0.67$ found by A. Cumming et al. (2007, in preparation) for the RV exoplanets sample within the range 0.03–3 AU. We have done the calculations for $a_{\rm min}$=10, 25, and 50 AU, and for all $a_{\rm max}$ in the range $[a_{\rm min} + 5, 500]$ AU; the results are presented in Figure 4.12 and the corresponding planet detection probabilities for each star are shown in Table 4.7 for a selection of semi-major axis intervals. Figure 4.13 illustrates how a synthetic population of planets based on the above distributions compares with our detection limits. For $\gamma = -1$, the 95% credible upper limits to the fraction of stars with at least one planet of mass in the range $[0.5, 13]$ $M_{\rm Jup}$ are 0.28 for the semi-major axis range 10–25 AU, 0.18 for 10–50 AU, 0.13 for 25–50 AU, 0.11 for 25–100 AU, and 0.093 for 50–250 AU. Slightly smaller values of $f_{\rm max}$ are found for larger values of γ, as such indices would place more planets at larger separations where they would have been easier to detect with our observations. For the larger values of $a_{\rm min}$, the value of γ has very little effect on the upper limit found as, irrespective of the value of γ, the majority of planets are located at separations for which the sensitivity of the observations is high. Overall, the weak dependence of $f_{\rm max}$ on γ implies that the semi-major axis distribution (i.e. γ) cannot be constrained from our results.

As one may worry that the population of planets around M dwarfs is different from that around earlier-type stars, because of smaller disk masses for example, we derive an estimate of $f_{\rm max}$ by excluding the M dwarfs from the statistical analysis. This estimate is obtained using Eq. (4.7) and the values of the last three columns of Table 4.7; it is thus valid for $\beta = -1.2$ and $\gamma = -1$. Excluding M dwarfs from the sample leaves 64 stars and results in average detection probabilities $\langle p_j \rangle$ of 0.070, 0.229, and 0.385 for 10–25 AU, 25–50 AU, and 50–250 AU, respectively. The corresponding 95% credible upper limits to the fraction of stars with planets are then 0.67, 0.20, and 0.12. The effect is quite significant at the smallest orbital separations, where M dwarfs provide

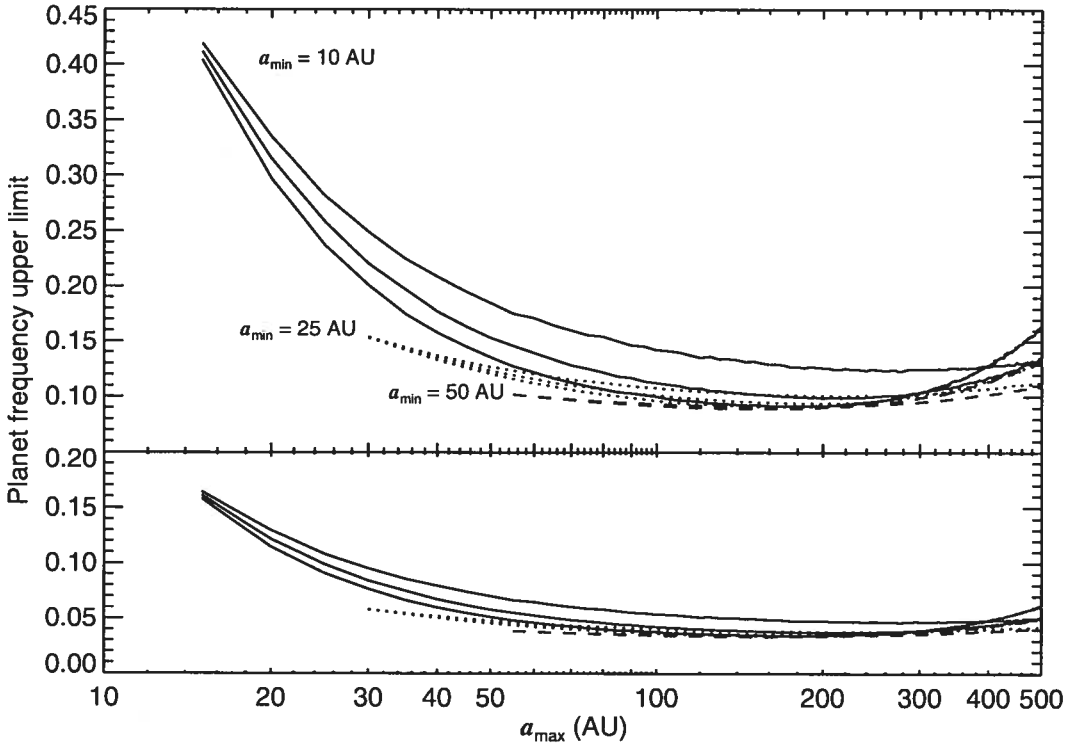

Figure 4.12 Upper limits, with a credibility of 95% (*top panel*) or 67% (*bottom panel*), on the fraction of stars harboring at least one giant planet of mass in the range $[0.5, 13]\, M_{\rm Jup}$, assuming $\mathrm{d}n/\mathrm{d}m \propto m^{-1.2}$, and orbit of semi-major axis in the range $[a_{\rm min}, a_{\rm max}]$ AU, assuming $\mathrm{d}n/\mathrm{d}a \propto a^{\gamma}$. The abscissa indicates the upper bounds ($a_{\rm max}$) of the semi-major axis intervals, while the lower bounds ($a_{\rm min}$) are 10 AU (*solid lines*), 25 AU (*dotted lines*), and 50 AU (*dashed lines*). The top, middle, and bottom curves in each set of three curves are for $\gamma = -1$, 0, and 1, respectively.

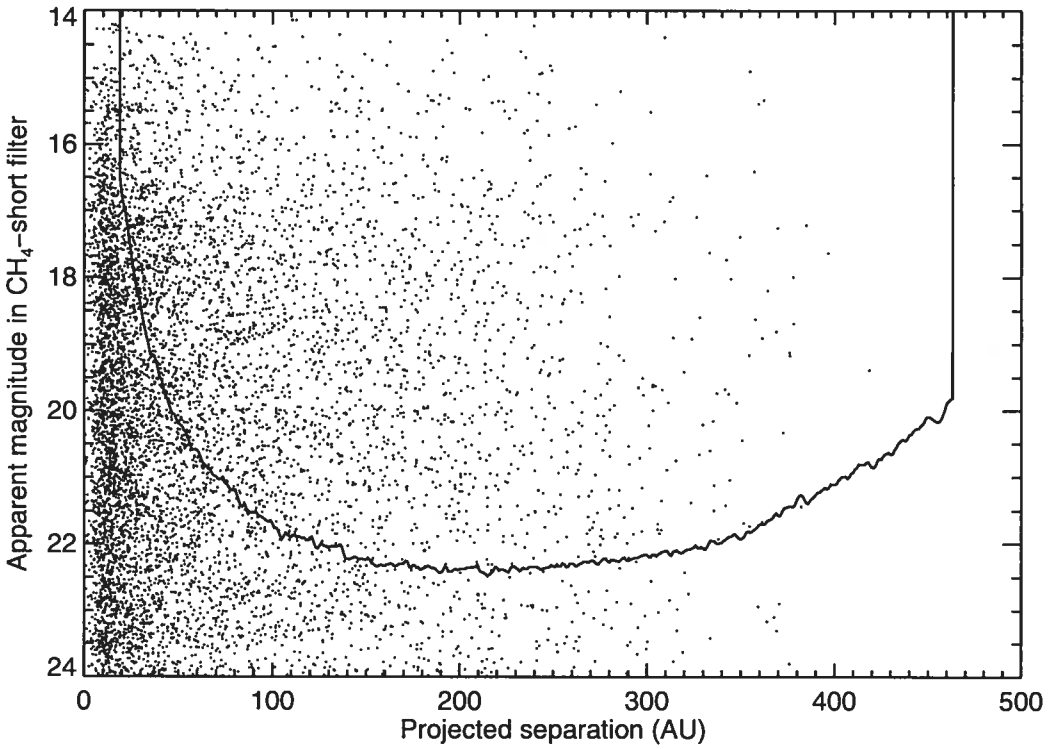

Figure 4.13 Detection limits (5σ, *solid line*) and synthetic population of planets (*dots*) for the star HD 166181. A planet mass distribution following $dn/dm \propto m^{-1.2}$ inside 0.5–13 $M_{\rm Jup}$ and a semi-major axis distribution following $dn/da \propto a^{-1}$ inside 10–300 AU were used. For this particular example, the planet detection probability p_j is 30%.

good sensitivities due to their smaller luminosity, smaller average distance, and younger average age. Similarly, the population of planets in stellar multiple systems may be different from that in single systems. Excluding multiples from the sample also leaves 64 stars and yields values of $\langle p_j \rangle$ of 0.139, 0.299, and 0.389 for 10–25 AU, 25–50 AU, and 50–250 AU. The corresponding upper limits to the fraction of stars with planets are 0.34, 0.16, and 0.12; the effect is thus rather small in this case.

4.6 Summary and conclusion

In this paper, we have presented the results of the Gemini Deep Planet Survey, a near-infrared adaptive optics search for giant planets on orbits of 10–300 AU around nearby young stars. The use of angular differential imaging at the Gemini North telescope has enabled us to reach the best sensitivities to date for detecting giant exoplanets with projected separations above $\sim 0.7''$. The typical detection limits (5σ) reached by the survey, in magnitude difference between an off-axis point source and the central star, are 9.5 at $0.5''$, 12.9 at $1''$, 15 at $2''$, and 16.5 at $5''$, sufficient to detect planets more massive than 2 $M_{\rm Jup}$ with a projected separation of 40–200 AU around a typical target star. More than 300 faint point sources have been detected around 54 of the 85 stars observed, but observations at a second epoch have revealed changes in separation and P.A. of these point sources relative to the target stars that are all consistent with those expected from unrelated background objects. The observations made as part of this survey have resolved the stars HD 14802, HD 166181, and HD 213845 into binaries for the first time.

We have presented a statistical analysis of the survey results to derive upper limits to the fraction of stars having planetary companions. This analysis indicates that the 95% credible upper limit to the fraction of stars harboring at least one planet more massive than 2 $M_{\rm Jup}$ with an orbit of semi-major axis in the range 25–420 AU or 50–295 AU is 0.23 or 0.12, respectively, independently of the mass and semi-major axis distributions

of the planets; for planets more massive than 5 $M_{\rm Jup}$, the upper limits are 0.09 for 25-305 AU and 0.057 for 50–185 AU. It was also found that less than 0.056 of stars have low-mass brown dwarf companions ($13 < m/M_{\rm Jup} < 40$) between 25 and 250 AU (see Figure 4.10); this upper limit is set by the sample size only as the sensitivity of the observations to brown dwarfs is very good. Considering the whole brown dwarf mass range, the 95% credible interval for the frequency of stars with at least one brown dwarf companion in the semi-major axis interval 25–250 AU is $0.019^{+0.083}_{-0.015}$. Assuming a mass distribution following $\mathrm{d}n/\mathrm{d}m \propto m^{-1.2}$, the results indicate that with a credibility of 95% the fraction of stars having at least one planet of mass in the range 0.5–13 $M_{\rm Jup}$ and semi-major axis in the range 25–325 AU is less than 0.17, and less than 0.10 for the range 50–220 AU. Assuming further a semi-major axis distribution following $\mathrm{d}n/\mathrm{d}a \propto a^{-1}$, the upper limits to the fraction of stars with planets are 0.28 for the range 10–25 AU, 0.13 for 25–50 AU, and 0.093 for 50–250 AU.

The work presented in this paper constitutes a first step toward the detection of the population of "outer" giant planets around other stars. Such a study, which is complementary to RV searches in terms of orbital separation, is necessary to improve our understanding of the various mechanisms that could generate planets on orbits of tens to hundreds of AU, such as in situ formation triggered by collisions of stars with proto-planetary disks or orbital migration induced by gravitational scattering in multiple planet systems. While the upper limits we have found rule out an important increase in the population of planets at large separations compared to the known population of planets below 3 AU, our sample size and the sensitivities we haved reached are insufficient to tell if the above mechanisms operate at all, and a fortiori which one is dominant. Future searches reaching better sensitivities and targeted at a larger sample of stars will be necessary to answer these questions.

Considerable efforts are currently deployed by major observatories to develop instruments dedicated to the search of giant exoplanets around nearby stars. The Gemini Planet Imager (GPI, Gemini Telescope, Macintosh et al., 2006) and the Spectro-Polarimetric

High-contrast Exoplanet Research instrument (SPHERE, Very Large Telescope, Dohlen et al., 2006) are good examples; they should see their first light in around 2010. These complex instruments will ally an extreme AO system to correct atmospheric wavefront errors to unprecedented levels of accuracy, a calibration system to correct instrumental quasi-static aberrations, a coronagraph to suppress the coherent on-axis stellar light, and differential imaging capabilities enabled by either multi-channel cameras or integral field spectrographs. The expected performance of these instruments, e.g. a contrast better than 17.5 mag at a separation of $0.5''$ for GPI (Macintosh et al., 2006), should allow detection of planets of 1 $M_{\rm Jup}$ aged less than 100–200 Myr at separations of 5–50 AU, significantly improving on the work presented here. These efforts should uncover the population of outer giant planets, if they exist, or place sufficient constraints on their existence to rule out the mechanisms that could generate them. In less than a decade the James Webb Space Telescope will allow similar studies to be done for relatively nearby M-type primaries, which are too faint for operating the wavefront sensor of extreme adaptive optics systems. Given all of the projects that should unfold in the next few years, the coming decade promises to be extremely exciting for exoplanet science.

Acknowledgments

We are grateful to the referee whose thorough review and excellent suggestions have improved the quality of this paper significantly. The authors would like to thank the Gemini staff for carrying out all the observations. This project was made possible through the support and generous allocation of observing time from the Canadian, US, UK, and Gemini staff time allocation committees. This work was supported in part through grants from the Natural Sciences and Engineering Research Council, Canada, from the Fonds Québécois de la Recherche sur la Nature et les Technologies, and from the Faculté des Études Supérieures de l'Université de Montréal. This research was performed in part under the auspices of the US Department of Energy by the University of

California, Lawrence Livermore National Laboratory under contract W-7405-ENG-48, and also supported in part by the National Science Foundation Science and Technology Center for Adaptive Optics, managed by the University of California at Santa Cruz under cooperative agreement AST 98-76783. This research has made use of the SIMBAD database, operated at Centre de Données astronomiques de Strasbourg (CDS), Strasbourg, France. This research has made use of the VizieR catalog service (Ochsenbein et al., 2000), hosted by the CDS.

References

Alibert, Y., Mordasini, C., Benz, W., & Winisdoerffer, C. 2005, A&A, 434, 343

Allard, F., Hauschildt, P. H., Alexander, D. R., Tamanai, A., & Schweitzer, A. 2001, ApJ, 556, 357

Allen, P. R., Koerner, D. W., Reid, I. N., & Trilling, D. E. 2005, ApJ, 625, 385

Alonso, R. et al. 2004, ApJ, 613, L153

Arribas, S., Mediavilla, E., & Fuensalida, J. J. 1998, ApJ, 505, L43+

Augereau, J. C., Lagrange, A. M., Mouillet, D., & Ménard, F. 1999, A&A, 350, L51

Baraffe, I., Chabrier, G., Allard, F., & Hauschildt, P. H. 2002, A&A, 382, 563

Baraffe, I., Chabrier, G., Barman, T. S., Allard, F., & Hauschildt, P. H. 2003, A&A, 402, 701

Barrado y Navascués, D., Stauffer, J. R., Song, I., & Caillault, J.-P. 1999, ApJ, 520, L123

Bate, M. R., & Bonnell, I. A. 2005, MNRAS, 356, 1201

Beaulieu, J.-P. et al. 2006, Nature, 439, 437

Biller, B. A., Close, L., Lenzen, R., Brandner, W., McCarthy, D. W., Nielsen, E., & Hartung, M. 2004, in Proc. SPIE, Vol. 5490, Advancements in Adaptive Optics, ed. D. Bonaccini Calia, B. L. Ellerbroek, & R. Ragazzoni, 389–397

Biller, B. A. et al. 2007, ApJS, in press. (astro-ph/0705.0066)

Bond, I. A. et al. 2004, ApJ, 606, L155

Boss, A. P. 1997, Science, 276, 1836

—. 2000, ApJ, 536, L101

—. 2001, ApJ, 563, 367

—. 2003, ApJ, 599, 577

—. 2006, ApJ, 637, L137

Brandeker, A., Jayawardhana, R., Khavari, P., Haisch, Jr., K. E., & Mardones, D. 2006, ApJ, 652, 1572

Burrows, A., Marley, M., Hubbard, W. B., Lunine, J. I., Guillot, T., Saumon, D., Freedman, R., Sudarsky, D., & Sharp, C. 1997, ApJ, 491, 856

Butler, R. P. et al. 2006, ApJ, 646, 505

Cameron, A. C. et al. 2007, MNRAS, 375, 951

Carpenter, J. M., Wolf, S., Schreyer, K., Launhardt, R., & Henning, T. 2005, AJ, 129, 1049

Carson, J. C., Eikenberry, S. S., Smith, J. J., & Cordes, J. M. 2006, AJ, 132, 1146

Cayrel de Strobel, G., Soubiran, C., Friel, E. D., Ralite, N., & Francois, P. 1997, A&AS, 124, 299

Cayrel de Strobel, G., Soubiran, C., & Ralite, N. 2001, A&A, 373, 159

Charbonneau, D., Brown, T. M., Latham, D. W., & Mayor, M. 2000, ApJ, 529, L45

Chatterjee, S., Ford, E. B., & Rasio, F. A. 2007, ArXiv Astrophysics e-prints, astro-ph/0703166

Chauvin, G., Lagrange, A.-M., Dumas, C., Zuckerman, B., Mouillet, D., Song, I., Beuzit, J.-L., & Lowrance, P. 2004, A&A, 425, L29

—. 2005a, A&A, 438, L25

Chauvin, G., Lagrange, A.-M., Udry, S., Fusco, T., Galland, F., Naef, D., Beuzit, J.-L., & Mayor, M. 2006, A&A, 456, 1165

Chauvin, G. et al. 2005b, A&A, 438, L29

Clem, J. L., VandenBerg, D. A., Grundahl, F., & Bell, R. A. 2004, AJ, 127, 1227

Close, L. M. et al. 2007, ApJ, 660, 1492

Deller, A. T., & Maddison, S. T. 2005, ApJ, 625, 398

Dempsey, R. C., Neff, J. E., O'Neal, D., & Olah, K. 1996, AJ, 111, 1356

Dohlen, K. et al. 2006, in Proc. SPIE, Vol. 6269, Ground-based and Airborne Instrumentation for Astronomy, ed. I. S. McLean & M. Iye, 62690Q

Donahue, R. A. 1993, PhD thesis, AA(New Mexico State Univ., University Park.)

Favata, F., Barbera, M., Micela, G., & Sciortino, S. 1995, A&A, 295, 147

Favata, F., Micela, G., Sciortino, S., & D'Antona, F. 1998, A&A, 335, 218

Fekel, F. C., Barlow, D. J., Scarfe, C. D., Jancart, S., & Pourbaix, D. 2005, AJ, 129, 1001

Fernandez, J. A., & Ip, W.-H. 1984, Icarus, 58, 109

Fuhrmann, K. 2004, Astronomische Nachrichten, 325, 3

Gaidos, E. J. 1998, PASP, 110, 1259

Gaidos, E. J., Henry, G. W., & Henry, S. M. 2000, AJ, 120, 1006

Gatewood, G., Coban, L., & Han, I. 2003, AJ, 125, 1530

Gerbaldi, M., Faraggiana, R., & Balin, N. 2001, A&A, 379, 162

Gontcharov, G. A., Andronova, A. A., & Titov, O. A. 2000, A&A, 355, 1164

Goto, M. et al. 2002, ApJ, 567, L59

Gould, A. et al. 2006, ApJ, 644, L37

Gray, R. O., Corbally, C. J., Garrison, R. F., McFadden, M. T., & Robinson, P. E. 2003, AJ, 126, 2048

Greaves, J. S. et al. 1998, ApJ, 506, L133

Hahn, J. M., & Malhotra, R. 2005, AJ, 130, 2392

Haisch, Jr., K. E., Lada, E. A., & Lada, C. J. 2001, ApJ, 553, L153

Heinze, A., Hinz, P., Sivanandam, S., & Meyer, M. 2006, in Bulletin of the American Astronomical Society, Vol. 38, Bulletin of the American Astronomical Society, 1212

Henry, T. J., Soderblom, D. R., Donahue, R. A., & Baliunas, S. L. 1996, AJ, 111, 439

Herriot, G. et al. 2000, in Proc. SPIE, Vol. 4007, Adaptive Optical Systems Technology, ed. P. L. Wizinowich, 115–125

Hinkley, S. et al. 2007, ApJ, 654, 633

Hodapp, K. W. et al. 2003, PASP, 115, 1388

Høg, E. et al. 1997, A&A, 323, L57

Høg, E. et al. 2000, A&A, 355, L27

Holland, W. S. et al. 1998, Nature, 392, 788

Hormuth, F., Brandner, W., Hippler, S., Janson, M., & Henning, T. 2007, A&A, 463, 707

Huensch, M., Schmitt, J. H. M. M., & Voges, W. 1998, A&AS, 132, 155

Hünsch, M., Schmitt, J. H. M. M., Sterzik, M. F., & Voges, W. 1999, A&AS, 135, 319

Ida, S., & Lin, D. N. C. 2004, ApJ, 604, 388

Itoh, Y. et al. 2005, ApJ, 620, 984

Jayawardhana, R., Coffey, J., Scholz, A., Brandeker, A., & van Kerkwijk, M. H. 2006, ApJ, 648, 1206

Kalas, P., Graham, J. R., & Clampin, M. 2005, Nature, 435, 1067

Kasper, M., Apai, D., Janson, M., & Brandner, W. 2007, ArXiv e-prints, astro-ph/0706.0095

Kirkpatrick, J. D., Dahn, C. C., Monet, D. G., Reid, I. N., Gizis, J. E., Liebert, J., & Burgasser, A. J. 2001, AJ, 121, 3235

Konacki, M., Torres, G., Jha, S., & Sasselov, D. D. 2003, Nature, 421, 507

Kotoneva, E., Flynn, C., Chiappini, C., & Matteucci, F. 2002, MNRAS, 336, 879

Lachaume, R., Dominik, C., Lanz, T., & Habing, H. J. 1999, A&A, 348, 897

Lafrenière, D., Marois, C., Doyon, R., Nadeau, D., & Artigau, E. 2007, ApJ, 660, 770

Levison, H. F., Morbidelli, A., Gomes, R., & Backman, D. 2007, in Protostars and Planets V, ed. B. Reipurth, D. Jewitt, & K. Keil, 669–684

López-Santiago, J., Montes, D., Crespo-Chacón, I., & Fernández-Figueroa, M. J. 2006, ApJ, 643, 1160

Lowrance, P. J. et al. 2005, AJ, 130, 1845

Luhman, K. L. 2004, ApJ, 614, 398

Luhman, K. L., Allers, K. N., Jaffe, D. T., Cushing, M. C., Williams, K. A., Slesnick, C. L., & Vacca, W. D. 2007a, ApJ, 659, 1629

Luhman, K. L., & Jayawardhana, R. 2002, ApJ, 566, 1132

Luhman, K. L. et al. 2007b, ApJ, 654, 570

Luhman, K. L. et al. 2006, ApJ, 649, 894

Macintosh, B. et al. 2006, in Proc. SPIE, Vol. 6272, Advances in Adaptive Optics II, ed. B. L. Ellerbroek & D. Bonaccini Calia, 62720L

Makarov, V. V. 2006, AJ, 131, 2967

Malhotra, R. 1995, AJ, 110, 420

Marcy, G., Butler, R. P., Fischer, D., Vogt, S., Wright, J. T., Tinney, C. G., & Jones, H. R. A. 2005, Progress of Theoretical Physics Supplement, 158, 24

Marley, M. S., Fortney, J. J., Hubickyj, O., Bodenheimer, P., & Lissauer, J. J. 2007, ApJ, 655, 541

Marois, C., Doyon, R., Nadeau, D., Racine, R., Riopel, M., Vallée, P., & Lafrenière, D. 2005, PASP, 117, 745

Marois, C., Doyon, R., Nadeau, D., Racine, R., & Walker, G. A. H. 2003, in EAS Publications Series, Vol. 8, Astronomy with High Contrast Imaging, ed. C. Aime & R. Soummer, 233–243

Marois, C., Doyon, R., Racine, R., & Nadeau, D. 2000, PASP, 112, 91

Marois, C., Lafrenière, D., Doyon, R., Macintosh, B., & Nadeau, D. 2006, ApJ, 641, 556

Marois, C., Macintosh, B., & Barman, T. 2007a, ApJ, 654, L151

Marois, C. et al. 2007b, ApJ, submitted.

Martín, E. L. 2003, AJ, 126, 918

Martin, R. G., Lubow, S. H., Pringle, J. E., & Wyatt, M. C. 2007, ArXiv Astrophysics e-prints, astro-ph/0704.3369

Masciadri, E., Mundt, R., Henning, T., Alvarez, C., & Barrado y Navascués, D. 2005, ApJ, 625, 1004

Matzner, C. D., & Levin, Y. 2005, ApJ, 628, 817

McCarthy, C., & Zuckerman, B. 2004, AJ, 127, 2871

Metchev, S. A. 2006, PhD thesis, California Institute of Technology, United States – California

Metchev, S. A., & Hillenbrand, L. A. 2004, ApJ, 617, 1330

Mohanty, S., & Basri, G. 2003, ApJ, 583, 451

Mohanty, S., Jayawardhana, R., Huélamo, N., & Mamajek, E. 2007, ApJ, 657, 1064

Montes, D., López-Santiago, J., Fernández-Figueroa, M. J., & Gálvez, M. C. 2001a, A&A, 379, 976

Montes, D., López-Santiago, J., Gálvez, M. C., Fernández-Figueroa, M. J., De Castro, E., & Cornide, M. 2001b, MNRAS, 328, 45

Mugrauer, M. et al. 2004, A&A, 417, 1031

Nadal, R., Pedoussaut, A., Ginestet, N., & Carquillat, J.-M. 1974, A&A, 37, 191

Neuhäuser, R., Guenther, E. W., Wuchterl, G., Mugrauer, M., Bedalov, A., & Hauschildt, P. H. 2005, A&A, 435, L13

Nielsen, E. L., Close, L. M., Biller, B. A., & Masciadri, E. 2007, ArXiv e-prints, astro-ph:0706.4331

Nordström, B. et al. 2004, A&A, 418, 989

Ochsenbein, F., Bauer, P., & Marcout, J. 2000, A&AS, 143, 23

Ozernoy, L. M., Gorkavyi, N. N., Mather, J. C., & Taidakova, T. A. 2000, ApJ, 537, L147

Perryman, M. A. C., & ESA. 1997, ESA SP Series, Vol. 1200, The HIPPARCOS and TYCHO catalogues. Astrometric and photometric star catalogues derived from the ESA HIPPARCOS Space Astrometry Mission (Noordwijk, Netherlands: ESA Publications Division)

Pollack, J. B., Hubickyj, O., Bodenheimer, P., Lissauer, J. J., Podolak, M., & Greenzweig, Y. 1996, Icarus, 124, 62

Potter, D., Martín, E. L., Cushing, M. C., Baudoz, P., Brandner, W., Guyon, O., & Neuhäuser, R. 2002, ApJ, 567, L133

Racine, R., Walker, G. A. H., Nadeau, D., Doyon, R., & Marois, C. 1999, PASP, 111, 587

Rasio, F. A., & Ford, E. B. 1996, Science, 274, 954

Reipurth, B., & Clarke, C. 2001, AJ, 122, 432

Rieke, G. H. et al. 2005, ApJ, 620, 1010

Rossiter, R. A. 1955, Publications of Michigan Observatory, 11, 1

Saffe, C., Gómez, M., & Chavero, C. 2005, A&A, 443, 609

Santos, N. C., Israelian, G., & Mayor, M. 2004, A&A, 415, 1153

Schneider, G., & Silverstone, M. D. 2003, in Proc. SPIE, Vol. 4860, High-Contrast Imaging for Exo-Planet Detection, ed. A. B. Schultz, 1–9

Schneider, G. et al. 1999, ApJ, 513, L127

Seifahrt, A., Neuhäuser, R., & Hauschildt, P. H. 2007, A&A, 463, 309

Shen, S., & Wadsley, J. 2006, ApJ, 651, L145

Sivia, D. S. 1996, Data Analysis: A Bayesian Tutorial (Oxford Science Publications) (Oxford University Press)

Soderblom, D. R., & Mayor, M. 1993, AJ, 105, 226

Song, I., Caillault, J.-P., Barrado y Navascués, D., Stauffer, J. R., & Randich, S. 2000, ApJ, 533, L41

Song, I., Zuckerman, B., & Bessell, M. S. 2004, ApJ, 614, L125

Sousa, S. G., Santos, N. C., Israelian, G., Mayor, M., & Monteiro, M. J. P. F. G. 2006, A&A, 458, 873

Sparks, W. B., & Ford, H. C. 2002, ApJ, 578, 543

Takeda, Y., & Kawanomoto, S. 2005, PASJ, 57, 45

Taylor, B. J. 2005, ApJS, 161, 444

Tsiganis, K., Gomes, R., Morbidelli, A., & Levison, H. F. 2005, Nature, 435, 459

Udalski, A. et al. 2005, ApJ, 628, L109

Udry, S., Fischer, D., & Queloz, D. 2007, in Protostars and Planets V, ed. B. Reipurth, D. Jewitt, & K. Keil, 685–699

Valdes, F., Gupta, R., Rose, J. A., Singh, H. P., & Bell, D. J. 2004, ApJS, 152, 251

Valenti, J. A., & Fischer, D. A. 2005, ApJS, 159, 141

Veras, D., & Armitage, P. J. 2004, MNRAS, 347, 613

Weidenschilling, S. J., & Marzari, F. 1996, Nature, 384, 619

Weinberger, A. J., Becklin, E. E., Schneider, G., Smith, B. A., Lowrance, P. J., Silverstone, M. D., Zuckerman, B., & Terrile, R. J. 1999, ApJ, 525, L53

Whitworth, A. P., & Stamatellos, D. 2006, A&A, 458, 817

Wichmann, R., Schmitt, J. H. M. M., & Hubrig, S. 2003, A&A, 399, 983

Wilner, D. J., Holman, M. J., Kuchner, M. J., & Ho, P. T. P. 2002, ApJ, 569, L115

Wright, J. T., Marcy, G. W., Butler, R. P., & Vogt, S. S. 2004, ApJS, 152, 261

Wyatt, M. C., Greaves, J. S., Dent, W. R. F., & Coulson, I. M. 2005, ApJ, 620, 492

Zuckerman, B., Bessell, M. S., Song, I., & Kim, S. 2006, ApJ, 649, L115

Zuckerman, B., & Song, I. 2004a, ApJ, 603, 738

—. 2004b, ARA&A, 42, 685

Zuckerman, B., Song, I., & Bessell, M. S. 2004, ApJ, 613, L65

Zuckerman, B., Song, I., Bessell, M. S., & Webb, R. A. 2001, ApJ, 562, L87

CHAPITRE 5

CONCLUSION

Le but principal du travail présenté dans cette thèse est la recherche d'exoplanètes géantes par imagerie directe. Pour aider aux efforts observationnels qui s'inscrivent dans cette lignée, deux outils ont été développés pour améliorer les performances de l'imagerie différentielle. Parallèlement à ce travail, une recherche d'exoplanètes a été réalisée avec le télescope Gemini Nord.

Les performances de l'imagerie différentielle spectrale simultanée avec une caméra multi-canal sont limitées par les aberrations optiques présentes dans la caméra, car celles-ci décorrèlent les images de la FÉP de l'étoile des différents canaux. Pour remédier à ce problème, il a été proposé dans cette thèse d'introduire un diffuseur holographique au plan focal d'entrée d'une caméra multi-canal. Le diffuseur a pour rôle de transformer l'image de la FÉP de l'étoile en une source étendue d'illumination incohérente, qui est par la suite imagée par la caméra multi-canal. Ainsi, les aberrations de la caméra ne modifient pas la structure globale de la FÉP de l'étoile et il en résulte des images mieux corrélées entre les canaux. Un modèle semi-analytique et des simulations numériques ont indiqué que l'atténuation possible avec cette technique devrait être proportionnelle au ratio du rapport focal de sortie du système avant le diffuseur sur le rapport focal d'entrée de la caméra multi-canal. Le concept a été validé par une expérience en laboratoire utilisant une caméra à deux canaux. L'utilisation d'un diffuseur holographique au plan focal de cette caméra a amélioré d'un facteur $\sim$5 l'atténuation de la FÉP obtenue par la soustraction de deux images simultanées à des longueurs d'onde différentes. Des simulations Monte Carlo de populations d'exoplanètes ont indiqué que ce gain permettrait de doubler le nombre d'exoplanètes qui pourraient être détectées actuellement avec un télescope de 8 mètres.

La solution au problème des aberrations différentielles présentée dans cette thèse

est simple, peu coûteuse, et facile à implémenter ; elle devrait être considérée pour des instruments futurs consacrés à la recherche de planètes par imagerie directe. De plus, une caméra multi-canal équipée d'un diffuseur au plan focal peut être utilisée de pair avec d'autres techniques d'imagerie à haute gamme dynamique, telles que la coronographie ou l'imagerie différentielle angulaire.

En imagerie différentielle il est très difficile, voire impossible, d'obtenir des images références d'une FÉP qui soient parfaitement corrélées. La façon particulière dont les images références disponibles sont utilisées pour soustraire la FÉP d'une image cible peut avoir un impact important sur l'atténuation réalisée. Dans cette thèse, un algorithme pour construire une image référence optimisée de la FÉP a été présenté. Pour chaque image cible, l'algorithme développé combine linéairement plusieurs images références de la FÉP de l'étoile de façon à ce qu'une fois cette combinaison d'images soustraite de l'image cible le bruit soit minimisé. L'optimisation des coefficients de la combinaison linéaire est faite de façon indépendante dans plusieurs sous-sections de l'image cible et la procédure d'optimisation assure que le bruit résiduel est minimal pour chaque sous-section. L'application de ce nouvel algorithme à une séquence d'imagerie différentielle angulaire a fourni un gain en sensibilité d'un facteur pouvant aller jusqu'à 3 aux séparations angulaires où le bruit de tavelure est le plus important. Cet algorithme peut être utilisé avec n'importe quelle technique d'imagerie qui vise à soustraire la FÉP d'une étoile à l'aide d'images références ; il pourrait donc s'avérer très utile pour la recherche de planètes par imagerie directe.

Enfin, les résultats d'une recherche de planètes géantes par imagerie directe ont été présentés. Cette recherche a été menée au télescope Gemini Nord et a eu recours à l'imagerie différentielle angulaire ainsi qu'à l'algorithme de combinaison d'images développé précédemment ; ces outils ont grandement contribué au succès du projet. L'échantillon des cibles observées est constitué de 85 étoiles de type spectral FGKM situées à moins de 35 pc du Soleil. La majorité de ces étoiles ont un âge estimé inférieur à 300 millions d'années.

La sensibilité des observations, exprimée en différence de magnitude à 1.6 μm entre une planète et son étoile, est typiquement de 9.5 à 0.5″, 12.9 à 1″, 15 à 2″, et 16.5 à 5″. Par rapport aux recherches de planètes qui avaient été faites auparavant, ces sensibilités constituent une amélioration d'au moins 1 mag à 1″, 1.5 mag à 2″, et ∼3 mag à plus grande séparation. Pour une étoile cible typique, c'est-à-dire une étoile de type K0 âgée de 100 millions d'années et située à 22 pc du Soleil, les sensibilités atteintes par nos observations permettent la détection de planètes plus massives que 2 $M_{\rm Jup}$ avec une séparation projetée entre 40 et 200 UA. Un peu plus de 300 exoplanètes candidates ont été identifiées autour de 54 des étoiles observées ; un suivi de 48 de ces étoiles a cependant permis de vérifier que leurs candidates sont toutes des étoiles d'arrière-plan.

Une analyse statistique des résultats a été faite pour déterminer, à un niveau de crédibilité de 95%, une limite supérieure à la fraction d'étoiles ayant une planète détectable. En ne faisant aucune supposition sur la fonction de masse ou la distribution en demi-grand axe des planètes, cette analyse indique que la fraction d'étoiles avec au moins une planète plus massive que 2 $M_{\rm Jup}$ sur une orbite de demi-grand axe entre 25 et 300 UA ou entre 50 et 200 UA est de 23% ou 12%, respectivement. Pour les planètes plus massives que 5 $M_{\rm Jup}$, ces limites sont respectivement de 9.2% et 5.7%. En supposant une fonction de masse $dn/dm \propto m^{-1.2}$ et une distribution en demi-grand axe $dn/da \propto a^{-1}$, la limite supérieure de la fraction d'étoiles avec au moins une planète de masse 0.5–13 $M_{\rm Jup}$ est de 28% pour l'intervalle de demi-grand axe 10–25 UA, 13% pour 25–50 UA, et 9.3% pour 50–200 UA.

La recherche de planètes présentée dans cette thèse constitue une première étape vers la détection de planètes géantes sur des orbites de dizaines d'UA autour d'autres étoiles. Une telle étude est nécessaire pour nous informer sur les mécanismes capables de produire des planètes sur de telles orbites. Bien que les résultats obtenus dans cette étude indiquent qu'il n'y a pas d'augmentation importante du nombre de planètes à grande séparation, en comparaison à la population connue en deça de 3 UA, la taille de l'échantillon observé et les sensibilités atteintes sont insuffisantes pour déterminer si

certains mécanismes opèrent réellement à ces séparations, et a fortiori lequel prédomine. D'autres recherches atteignant de meilleures sensibilités sont nécessaires pour répondre à ces questions. De telles recherches seront réalisées dans les prochaines années.

Des projets instrumentaux au sol tels que le *Gemini Planet Imager* (Gemini Telescope), le *Spectro-Polarimetric High-contrast Exoplanet Research instrument* (Very Large Telescope), et le *Planet Formation Imager* (Thirty-Meter Telescope) devraient mener aux premières découvertes de planètes géantes sur des orbites de plus de 10 UA autour d'étoiles de type solaire et permettre, pour la première fois, des études détaillées de leur atmosphère. D'autres projets, tels que *Gaia*, *DARWIN*, *CoRoT*, *Kepler*, *SIM-PlanetQuest*, *JWST*, *TPF*, ou *New Worlds Discoverer* permettront d'étudier les populations d'exoplanètes dans d'autres régimes de masse et de séparation orbitale. Avec tous les projets qui devraient voir le jour au cours des prochaines années, la prochaine décennie promet d'être extrêmement passionnante pour la science des exoplanètes.

Annexe I

Permissions de l'éditeur

Annexe II

Déclarations des coauteurs des articles